# Quantum Chemistry in Radical Studies

by

Qianyi Cheng

(Under the direction of Henry F. Schaefer III)

## Abstract

Free radicals are often highly chemically reactive due to the unpaired electrons in an open shell configuration, and they usually play an important role in combustion, atmospheric chemistry, biochemistry, polymerization, plasma chemistry, and many other processes. Radicals have also been found to be involved in degenerative diseases and cancers.

Water dimer radical cation has been studied using coupled cluster theory CCSD and CCSD(T) with Dunning's correlation consistent polarized valence basis sets (cc-pV$X$Z and aug-cc-pV$X$Z, where $X$ =D, T, Q). Among the fourteen stationary points which have been characterized on its doublet electronic state potential energy surface, isomers **1** and **7** are found to be local minima, seven are transition states, and the remaining five are higher order saddle points. The fourteen structures lie within 45 kcal mol$^{-1}$ of isomer **1**, and the interconversion barrier from **1** to **7** is 15.1 kcal mol$^{-1}$.

The cyclic, *trans*, and *cis*-BNNO radicals and two isomerization reactions are systematically investigated using SCF, CASSCF, CCSD and CCSD(T) levels of theory with cc-pV$X$Z and aug-cc-pV$X$Z (where $X$ =D, T, and Q) basis sets. All stationary points lie within 19 kcal mol$^{-1}$ of the global minimum cyclic isomer at the aug-cc-pVQZ CCSD(T) level. Contrary to the result of Wang and Zhou, the *trans*-structure is not the global minimum, but is rather the second lowest lying isomer. This apparent disparity is rationalized by a detailed examination of the PES describing this reaction.

Hydroxyl radical reactions with adenine have been studied at the B3LYP/DZP++ level of theory. Hydrogen atoms directly attached to five positions ($C_2$, $C_8$, $N_9$, $N_{61}$, and $N_{62}$) have been examined for dehydrogenation. Four reactant complexes [A$\cdots$OH]$\cdot$ have been found connecting to six transition states, leading to six product complexes [A$-$H$\cdots$H$_2$O]$\cdot$ and five final products A$-$H$\cdot$ + H$_2$O. All six pathways are exothermic. The dehydrogenation at $N_6$ is predicted to be favorable, while that at $C_8$ is unlikely.

INDEX WORDS: computational chemistry, coupled cluster theory, density functional theory, potential energy surface, radicals, DNA damage

# Quantum Chemistry in Radical Studies

by

Qianyi Cheng

B.S., Nanjing Forestry University, 2004

M.S., Mississippi College, 2007

A Dissertation Submitted to the Graduate Faculty

of The University of Georgia in Partial Fulfillment

of the

Requirements for the Degree

Doctor of Philosophy

Athens, Georgia

2011

# Quantum Chemistry in Radical Studies

by

Qianyi Cheng

Approved:

Major Professor: Henry F. Schaefer III

Committee: Geoffrey D. Smith
Nigel G. Adams

Electronic Version Approved:

Maureen Grasso
Dean of the Graduate School
The University of Georgia
May 2011

## Dedication

For my parents, their support means so much to me.

# Acknowledgments

In the memorable, fruitful, and enjoyable four years at CCQC, there are many people without whom this work could not have been completed.

I would like to express my deepest gratitude to my advisor Professor Schaefer for giving me the opportunity to be a member of the CCQC. I really appreciate the freedom, support, and advice that he has given me in exploring various areas of quantum chemistry, as well as the great chance to meet with so many outstanding scientists and enjoy so many inspiring talks and lectures. His mentorship is directly responsible for my current and future accomplishments as a scientist.

Dr. Yamaguchi deserves my great appreciation for his patience and willingness to help me understand key concepts in quantum chemistry and writing scientific papers. I will always remember his passion and carefulness about quantum chemistry. I would also like to thank Professor Allen, Dr. Xie, and Dr. Gu for teaching me and helping me during my four years here. Credit is also due to Francesco Evangelista, Andrew Simmonett, and Jeremiah Wilke for guiding and helping me in my research.

I would like to thank Dr. Magers, who persuaded me to continue my studies, for his incredible commitment to each of his students and his dedication to scientific education. Without his great help and faith in me, I would never have conquered the hard times of both studying and living in a foreign country. Nor would I have had the opportunity to experience learning computational chemistry and understanding the correlation between this special and useful chemistry and my specific field.

Finally, I would like to thank all my research colleagues for their friendship and for their commitment to CCQC. Especially, Katie, Bo, and Beulah and many others: you hold a

special place in my heart and are responsible for so many fond memories of my time here at UGA. I will miss each and every one of you as we continue in our scientific endeavors.

Not least in this group are my parents, who have supported me emotionally and spiritually throughout my time studying abroad. Without them, I would never have gotten this far.

# Table of Contents

# Chapter 1

# Introduction and Literature Review

## 1.1 Computational Chemistry

As a branch of theoretical chemistry, computational chemistry solves chemical problems, such as determination of molecular properties, by using principles of computer science and efficient computer programs. Molecules differ from each other because they have different nuclei and numbers of electrons; in other words, their nuclear centers are at different positions. Even a single molecular formula can have different conformational isomers on its potential energy surface. Computational chemistry attempts to interpret geometrical configurations of stable molecules, their absolute and relative energies, properties (such as dipole moment, polarizability, NMR coupling constants, etc.), reaction rates, and time dependent structures and properties.

*Ab initio* method is widely used to determine electronic structures and properties of molecules by finding approximate solutions of the non-relativistic time-independent Schrödinger equation

$$\hat{H} \mid \Phi\rangle = E \mid \Phi\rangle \tag{1.1}$$

$\hat{H}$ is the many-electron operator (the Hamiltonian), and $\Phi$ is the many-electron wave function (Slater determinants and linear combinations of these determinants). A key part of solving the Schrödinger equation is the Born-Oppenheimer approximation, in which the coupling between the nuclei and electronic motion is neglected. The problem then is reduced to solving the electronic Schrödinger equation for a given set of nuclear coordinates, which greatly simplifies the situation.

The simplest *ab initio* electronic structure computation is the Hartree-Fock (HF) model, where each electron is described by an orbital, and the total wave function is the product of a set of orbitals. The Hartree-Fock method generates solutions to the Schrödinger equation in which the electron-electron interactions are assumed to be an average effect, and the correlation between electrons is neglected. In a sufficiently large basis set, the Hartree-Fock method is able to account for about 99% of the total electronic energy, but the remaining 1% is often very important for describing chemical phenomena.

## 1.2 Coupled Cluster Theory

In order to achieve chemical accuracy of 1 kcal mol$^{-1}$, it is necessary to use sophisticated methods for including electron correlation and large basis sets. This is often only computationally feasible for small systems. There are three main methods for computing electron correlation: configuration interaction (CI), many-body perturbation theory (MBPT), and coupled cluster (CC).[1] Among the three, coupled cluster has emerged as the most reliable and computationally affordable treatment for describing electron correlation and providing approximate solutions to the electronic Schrödinger equation for many body systems, since its introduction into quantum chemistry in the late 1960s by Čížek and Paldus.[2–4] The exponential ansatz is essential in coupled cluster theory, which characterizes a system by expanding the reference wave function exponentially:

$$\mid \Phi_{cc}\rangle = e^{\hat{T}} \mid \Phi_0\rangle \tag{1.2}$$

where $\mid \Phi_0\rangle$ is generally a Hartree-Fock reference wave function. The exponential operator is defined as

$$e^{\hat{T}} = 1 + \hat{T} + \frac{1}{2}\hat{T}^2 + \frac{1}{6}\hat{T}^3 + \cdots = \sum_{k=0}^{\infty} \frac{1}{k!}\hat{T}^k \tag{1.3}$$

and the exponentiated cluster operator $\hat{T}$ is the summation of excitation operators, $\hat{T} = \hat{T}_1 + \hat{T}_2 + \hat{T}_3 + \cdots$. When appling $\mathrm{e}^{\hat{T}}$ to the reference function, a new wave function containing cluster functions which correlate the motions of a specified number of electrons will

be produced. If the exponentiated operator includes contributions from all possible electron groupings, then the exact wave function will be obtained from the reference wave function. Truncation of the cluster operator at specific excitation levels leads to a hierarchy of coupled cluster techniques. Coupled cluster theory with single and double excitations (CCSD, where $\hat{T} = \hat{T}_1 + \hat{T}_2$)[5,6] has sufficient accuracy to be widely applied in many computational studies. CCSD with perturbative triple excitations [CCSD(T)][7–9] is often referred as "the gold standard of quantum chemistry" for its good compromise between high accuracy and computational cost for molecules near their equilibrium geometries.

The main drawback of the coupled cluster approach is the unfavorable scaling with system size. CCSD equations scales as $N^6(o^2v^4$, where $o$ and $v$ are the number of occupied and unoccupied orbitals in the wave function, which increases with the number of electrons in the system and one-particle basis set augmentation, respectively). CCSD(T) scales as $N^7(o^3v^4)$. Thus, a great deal of time is often required to achieve $\sim$1 kcal mol$^{-1}$ accuracy for large systems.

### 1.3 Density Functional Theory

Density functional theory (DFT) scales as $N^3$ (scales three dimensionally), and can be considered as a simple improvement on HF theory, which scales as $N^4$. The energy of the molecule, including the electron correlation, is defined as a functional of electron density.[11,12]

$$\text{Electron density} = \rho(x, y, z)$$

$$\text{Energy} = F[\rho(x, y, z)]$$

As a result, DFT calculations are typically faster and more accurate than HF. DFT can also perform computations on some molecules that are not possible with *ab initio* methods, such as transition metals and very large bio-systems.[13] Density functional theory has enjoyed enormous success in recent years, providing the seemingly impossible combination of accuracy and computational efficiency. As such, DFT is often the first choice for predicting

thermochemical values and mapping out potential energy surfaces for complex reactions. It is ideally suited for this purpose, providing qualitative information about potential energy surfaces with minimal computational effort.

There are roughly three categories of density functional methods: local density approximation (LDA) methods, gradient-corrected (GC) methods, and hybrid methods. In LDA methods, the density of the molecule is assumed to be a uniform electron gas and the functional depends only on the density at the coordinate where the functional is evaluated. The term LDA (or SVWN, or LSDA when considering spin) in literature usually refers to Slater's exchange functional plus the VWN correlation functional. This method predicts good geometries, but greatly over-binds molecules. Improvements over the LDA assumption need to consider the density as non-uniform electron gas throughout the molecule. As one step in this direction, GC methods make the exchange and correlation energies depend not only on the electron density, but also on derivatives of the density. However, higher-order gradient corrections are very difficult to compute, and little is known about them. Hybrid methods incorporate HF exchange into some improved DFT equations. As an example, B3LYP is

$$E_{xc}^{B3LYP} = a \times E_x^{Slater} + (1-a) \times E_x^{HF} + b \times \Delta E_x^{B88} + (1-c) E_c^{VWN} + c \times \Delta E_c^{LYP} \quad (1.4)$$

where the non-local correlation is provided by the LYP expression and the constants a, b, and c are determined by fitting to experimental data. This is the most commonly used DFT method.

However, there are several disadvantages to DFT methods. Determining the most appropriate method for a particular application is a major difficulty. Many popular DFT functionals contain empirically adjusted parameters, so, as with all semi-empirical methods, application of these functionals to systems dissimilar to the training set can result in unexpected behavior. Furthermore, DFT methods lack a means of systematic improvement of results, so that their accuracy is difficult to appraise.

## 1.4 Radicals and DNA Damage

Focusing on free radicals, my dissertation covers a wide range of system sizes. Thus, both *ab initio* and DFT methods were employed.

A plethora of computational studies have targeted on free radicals, because they usually exhibit interesting properties. Free radicals (often referred to as radicals for simplicity) are atoms, molecules, or ions with unpaired electrons in an open shell configuration. However, metals and their ions or complexes with unpaired electrons are not considered as radicals, even though they have unpaired electrons. Free radicals are often highly chemically reactive due to the unpaired electrons, and they usually play an important role in combustion, atmospheric chemistry, biochemistry, polymerization, plasma chemistry, and many other chemical processes, including human physiology. They are believed to be involved in degenerative diseases and cancers.

Radicals, such as the highly reactive hydroxyl radicals which are usually produced by radiolysis of water in cells, will cause indirect DNA damage, in addition to direct damage from radiation impinging on DNA.[10,14–16] Experiments have shown that these indirect effects may involve low-energy electrons or low-energy reaction barriers, but could indeed cause DNA strand breaks. Since DFT provides reliable electronic property results for systems of this size, computational studies such as reaction pathways, mechanisms, and energetic information may shed light on the corresponding biochemical experiments, leading to possible therapies for certain diseases and cancers.

## 1.5 Prospectus

Applying various computational methods, three open shell molecular systems have been studied. We begin with the water dimer radical cation, $(H_2O)_2{}^+$, in Chapter 2. The purpose of this work is to locate as many isomers as possible on its doublet potential energy surface, and compare geometries, vibrational frequencies, and energetics among different isomers and

with experimental results. Although there are few experimental observations of $(H_2O)_2^+$, the results of Ar bonded complexes can still provide a hint of the geometries and frequencies. In Chapter 3, we characterized the isomerization reaction of BNNO molecule, which is important in combustion and the chemical industry. In Appendix A, which is not included as a chapter, we investigated the geometries, molecular orbitals, vibrational and fundamental frequencies of BNNO molecule, as well as its isotopic shifts and energetics. In the last chapter, we investigated the dehydrogenation of adenine when hydroxyl radical attack this important nucleobase. This reaction is believed to be one of the causes of DNA damage. Six reaction pathways corresponding to five unique hydrogen abstractions have been examined at the B3LYP/DZP++ level. Geometries, local barriers, and thermodynamic properties are presented for the four reactant complexes, six transition states, and six product complexes along these reaction pathways, as well as optical transitions for the six final dehydrogenated adenine (A−H)· radicals.

## Bibliography


[1] T. D. Crawford, H. F. Schaefer, *Rev. Comput. Chem.* **2000**, *14*, 33.

[2] J. Čížek, *J. Chem. Phys.* **1966**, *45*, 4256.

[3] J. Čížek, *Adv. Chem. Phys.* **1969**, *14*, 35.

[4] J. Čížek, J. Paldus, *Int. J. Quantum Chem.* **1971**, *5*, 359.

[5] C. Hampel, K. A. Peterson, H. J. Werner, *Chem. Phys. Lett.* **1992**, *190*, 1.

[6] J. D. Watts, J. Gauss, R. J. Bartlett, *Chem. Phys. Lett.* **1992**, *200*, 1.

[7] K. Raghavachari, G. W. Trucks, J. A. Pople, M. Head-Gordon, *Chem. Phys. Lett.* **1989**, *157*, 479.

[8] J. D. Watts, J. Gauss, R. J. Bartlett, *J. Chem. Phys.* **1993**, *98*, 8718.

[9] J. F. Stanton, *Chem. Phys. Lett.* **1997**, *281*, 130.

[10] S. Steenken, *Chem. Rev.* **1989**, *89*, 503.

[11] D. M. Ceperley, B. J. Alder, *Phys. Rev. Lett.* **1980**, *45*, 577.

[12] S. H. Vosko, L. Wilk, M. Nusair, *Can. J. Phys.* **1980**, *58*, 1200.

[13] A. O. Colson, M. D. Sevilla, *J. Phys. Chem.* **1995**, *99*, 13033.

[14] B. D. Michael, P. O'Neill, *Science* **2000**, *287*, 1603.

[15] B. Boudaiffa, P. Cloutier, D. Hunting, M. A. Huels, L. Sanche, *Science* **2000**, *287*, 1658.

[16] I. S. Hong, H. Ding, M. M. Greenberg, *J. Am. Chem. Soc.* **2006**, *128*, 485.

# CHAPTER 2

## THE WATER DIMER RADICAL CATION: STRUCTURES, VIBRATIONAL FREQUENCIES, AND ENERGETICS[†]

[†]Reproduced with permission from [Qianyi Cheng, Francesco A. Evangelista, Andrew C. Simmonett, Yukio Yamaguchi and Henry F. Schaefer, III, *J. Phys. Chem. A*, 2009, **113**, 13779-13789] Copyright [2009] American Chemical Society.

## 2.1 Abstract

Fourteen stationary points for the water dimer radical cation on its doublet electronic state potential energy surface have been characterized using coupled cluster theory with single and double excitations (CCSD) and CCSD with perturbative triple excitations [CCSD(T)]. This is done in conjunction with Dunning's correlation consistent polarized valence basis sets (cc-pV$X$Z and aug-cc-pV$X$Z, $X$ = D, T, Q). Two stationary points are found to be local minima, isomer **1** ($C_1$ symmetry) with $H_3O^+ \cdots OH$ character (hydrogen-bonded system), and isomer **7** ($C_2$ symmetry) with $[H_2O \cdots H_2O]^+$ character (hemi-bonded system). Among the other stationary points, seven are transition states, and the remaining five are higher order saddle points. The fourteen water dimer radical cation structures lie within 45 kcal mol$^{-1}$of isomer **1**. Structure **1**, transition states **2** ($C_s$ symmetry) and **3** ($C_s$ symmetry) are related through torsion of the OH group; these three stationary points fall within one kcal mol$^{-1}$, demonstrating the low energy barrier of the OH torsional mode. Adiabatic ionization energies of $(H_2O)_2$ to **1** and **7** are determined to be 10.81 and 11.19 eV, respectively; the former is in excellent agreement with the experimental value of 10.8–10.9 eV. The critical dissociation energy of **1** to $H_3O^+$+OH· is predicted to be 26.4 kcal mol$^{-1}$, while the dissociation energy of isomer **7** to $H_2O^+$+ $H_2O$ is determined to be 34.7 kcal mol$^{-1}$. At the aug-cc-pVQZ CCSD(T) level of theory, the hydrogen-bonded **1** and hemi-bonded **7** minima are separated by 8.8 kcal mol$^{-1}$, with an interconversion barrier (**1**→**10**→**7**) of 15.1 kcal mol$^{-1}$. A careful comparison is made with the recent experiments of Gardenier, Johnson, and McCoy on $(H_2O)_2^+$·Ar and $(H_2O)_2^+$·$Ar_2$.

## 2.2 Introduction

Dynamical simulations and computations of the bulk properties of liquids[1,2] become computationally tractable when energies and forces are obtained from inexpensive methods, such as molecular mechanics, semi-empirical theory, or density functional theory (DFT).

In molecular mechanics, force fields are often constructed to perform well for a specific problem; in this process, *ab initio* information is often used to impose constraints on the parameterization. Even when employing density functional theory, the choice of a specific functional is usually made based upon comparisons to *ab initio* results. For both of these purposes, reference data on small model systems is typically employed.

Given the ubiquity of water in biological processes, it is no surprise that small water clusters[3–8] have been investigated extensively. These studies include the characterization of electron attachment and localization modes (surface and interior states) in water clusters,[4–6,9] ionized clusters,[1,2,10–21] $(H_2O)_n^-$, $(H_2O)_n^+$, and fragmentation processes occurring upon ionization,[15,22–27] as well as studies of ion and neutral hydration systems,[15,22,28–30] i.e., $X(H_2O)_n$ and $X(H_2O)_n$, where X is a solvated species (atom or molecule), including the protonated clusters $(H_2O)_nH^+$.[7,15,22,28,31–33] The fascinating rearrangement dynamics of hydrogen-bond networks and unique proton transfer mechanisms in water have led to myriad experimental studies.[11,12,20,27,30,34,35]

Experiments on water clusters have primarily focused on neutral molecules, hydrated electron clusters[6,36–42] and protonated cluster ions $(H_2O)_nH^+$. Protonated clusters exhibit very rich and varied chemistry, such as electron transfer, proton transfer, and molecular rearrangement. The smallest of these clusters, $(H_2O)_2H^+$, plays an important role in the ion chemistry of the upper atmosphere, dominating the ion composition in the D region in the ionosphere.[43] Furthermore, oxonium ions such as $H_3O^+$ and $H_5O_2{}^+$ occur as solvated charge carriers in aqueous solutions, condensed phases (ices), and clusters such as $(H_2O)_{21}H^+$ [often referred as $(H_2O)_{20}{\cdot}H_3O^+$, an oxonium hydrated in a cage of 20 water molecules].[44] These charged water species have been investigated experimentally and theoretically.[1,2,15,18,22,26,27]

In contrast, much less work has been done on the electronic and molecular structures of corresponding radical cation clusters $(H_2O)_n{}^+$, which are, for example, generated in *vivo* by water radiolysis. Early photoionization studies[12] of neutral water dimer detected a low signal of $(H_2O)_2{}^+$ near threshold and determined an upper bound of the dimer adiabatic

ionization potential (aIP) [$(H_2O)_2$]≤11.21±0.09 eV; a lower value of 10.81–10.90 eV has also been suggested.[14] Later He I photoelectron measurements[34] determined the vertical ionization potential (vIP) [$(H_2O)_2$] = 12.1±0.1 ($^2$A" state) and 13.2±0.2 eV ($^2$A' state). Shinohara et al.[11] observed unprotonated $(H_2O)_n^+$ clusters (2≤n≤10) for the first time by applying near threshold photoionization with an Ar resonance lamp (11.83 eV) for a molecular beam expansion of $H_2O$ and Ar. Recently, Dong[35] detected a small signal for $(H_2O)_2^+$, the daughter ion for $(H_2O)_3$, using a soft X-ray laser. These experiments suggest that the exiting electron removes almost all of the excess energy in these clusters. The difficulty of observing $(H_2O)_n^+$ clusters is attributed[26,45] to the large configurational differences between the parent neutrals and the ionized clusters, which result in small Franck-Condon factors for the ionization process.[46–48] Consequently, the vertically ionized cluster is formed in a highly vibrationally excited state, leading to dissociation.[46,49,50] Dissociation of the neutral water dimer may occur via two alternative channels[26]: the "oxonium channel" [$(H_2O)_2 + h\nu \rightarrow H_3O^+ + OH + e^-$], and the "water channel" [ $(H_2O)_2 + h\nu \rightarrow H_2O^+ + H_2O + e^-$]. In 2009, Gardenier and coworkers[27] reported a spectroscopic study of the ion-radical hydrogen-bonded $H_4O_2^+$. Based on the pattern of infrared transitions, it was unambiguously established that this species is best described as the $H_3O^+ \cdots OH\cdot$ ion-radical complex.

Early theoretical studies[47,51] of the neutral water dimer reported 10 stationary point structures (all with $H_2O\cdots H_2O$ character), at the second- and fourth-order Møller-Plesset levels of theory.[51] Later, coupled cluster with single and double excitations (CCSD) as well as CCSD with perturbative triple excitations [CCSD(T)] were employed to refine the structures.[47] The 10 structures include one minimum (nonplanar open $C_s$), three transition states (open $C_1$, cyclic $C_i$, and nonplanar bifurcated $C_{2v}$), and six higher order saddle points. The energy barriers connecting these structures range from 0.52 to 1.79 kcal mol$^{-1}$.

The water dimer radical cation $(H_2O)_2^+$ has also been studied theoretically.[52–54] Two different structures can result from ionization of the neutral; one is the oxonium-like complex $H_3O^+ \cdots OH$, and the other is the water-like complex $[H_2O\cdots H_2O]^+$. In 1987, Gill

and Radom characterized the $^2$A" state of the hydrogen-bonded ($C_s$ symmetry) isomer and the $^2B_u$ state of the hemi-bonded ($C_{2h}$ symmetry) isomer as two minima at the MP4/6-311G(MC)**//MP2/6-31G* level of theory.[55] The energy difference between the two isomers was found to be 8.9 kcal mol$^{-1}$. Sodupe, Oliva, and Bertran located five structures[56] of the ionized water dimer $(H_2O)_2^+$, including two $C_1$ minima (one hydrogen-bonded structure and one hemi-bonded structure) and three transition states (two $^2$A' states for the $C_s$ hemi-bonded isomers and one $^2$A" state for the $C_s$ hydrogen-bonded isomer) at the MCPF/TZ2P++//MP2/TZ2P++ level of theory.[56] In Sodupe's paper, the $C_s$ symmetry transition state was found to be similar to the $C_1$ minimum structure, but with the OH rotated out of the plane. The energy difference between these two structures was predicted to be 0.03 kcal mol$^{-1}$. The vertical ionization energies of the water dimer were computed to be 11.5 and 12.9 eV for the $^2$A" and $^2$A' states, respectively.

In the present research, a systematic theoretical study employing the CCSD and CCSD(T) levels of theory is carried out to investigate the molecular and electronic structures of the water dimer radical cations. The purpose of our research is to characterize the structures of the fourteen stationary points on the electronic doublet potential energy surface (PES) and to examine the dissociation pathways of ionized water dimers. Furthermore, newly determined structures and binding energies will be compared with previous studies[47,51] of the neutral water dimer and water dimer radical cations.[55,56] Our results will hopefully serve as benchmarks, against which more approximate models can be calibrated.

## 2.3 Theoretical methods

The geometries of the water dimer and the different water dimer radical cation structures were optimized at the unrestricted coupled cluster with single and double excitations (UCCSD)[57–59] and UCCSD with a perturbative approximation of triple excitations [UCCSD(T)][57,60,61] levels of theory. However, restricted open-shell Hartree-Fock (ROHF) wave functions were used as a reference. Structures of neutral water dimers and water dimer

radical cations discussed previously[47,51,55,56] were used as starting points for geometry optimizations. Dunning's correlation-consistent polarized valence basis sets (cc-pV$X$Z and aug-cc-pV$X$Z, where $X$ = D, T, Q)[62,63] were employed. The harmonic vibrational frequencies of stationary points were determined via numerical differentiation of total energies. Second order Møller-Plesset perturbation theory (MP2)[64] was employed in the intrinsic reaction coordinate (IRC) analysis.

The computations were carried out using QChem 3.1,[65] Molpro 2006.1,[66] the Mainz-Austin-Budapest (MAB) version of ACESII,[67,68] and PSI3.[69]

## 2.4 Results and Discussion

### 2.4.1 structural analyses

The optimized structures of the neutral water dimer and the fourteen stationary points (**1** – **14**, numbered in order of increasing energy) of the water dimer radical cation [at the aug-cc-pVQZ CCSD(T) level of theory] are displayed in Figures. 1 – 4 and Table 1.

These fourteen $(H_2O)_2{}^+$ stationary points may be classified in the following three categories: Group A ($H_2O$–$H^+ \cdots OH$) – proton transferred structures (**1** – **5**) with a bridging hydrogen, Group B ($H_3O^+ \cdots OH$) – proton transferred structures (**6** and **9**) without the hydrogen bridge, and Group C ($[H_2O \cdots H_2O]^+$) – hemi-bonded structures (**7**, **8**, **10** – **14**). For the proton-transferred ($H_3O^+ \cdots OH$) complex, the positive charge lies mainly on the $H_3O^+$ fragment, while for the hemi-bonded ($[H_2O \cdots H_2O]^+$) complex, the positive charge is delocalized between the two monomers.

#### Group A

Structures **1** – **5** (shown in Figure. 2) all fall into group A as a result of their connectivity, but have different orientations of the OH group. Among these five structures isomer **1** is the global minimum on the doublet electronic ground state PES, while **2** and **3** are transition states connecting mirror images of **1** via OH torsion. Structures **4** and **5** are analogous to **1**

– **3**, but with different symmetry constraints imposed. Comparing the neutral water dimer global minimum ($^1$A' $C_s$) and the water dimer radical cation **1** ($^2$A $C_1$) structure, there are significant geometrical changes:

1) the symmetry of the dimer is lowered from $C_s$ to $C_1$ upon ionization;

2) the hydrogen bond (H-bond) is slightly closer to linearity for the dimer radical cation [$\theta_e(\mathrm{OH}\cdots\mathrm{O}) = 173.4°$] than for the neutral [$\theta_e((\mathrm{OH}\cdots\mathrm{O}) = 171.6°$];

3) the oxygen-oxygen distance of the dimer radical cation [$r_e(\mathrm{O}_1\cdots\mathrm{O}_2) = 2.506$ Å] is shorter than that of the neutral [$r_e(\mathrm{O}_1\cdots\mathrm{O}_2) = 2.910$ Å];

4) the H-bonded OH bond distance for the dimer radical cation [$r_e(\mathrm{O_2H_4}) = 1.048$ Å] is longer than that for the neutral [$r_e(\mathrm{O_1H_4}) = 0.965$ Å];

5) the non H-bonded OH bond distances for the dimer radical cation [$r_e(\mathrm{O_2H_5}) \approx r_e(\mathrm{O_2H_6}) = 0.971$ Å] are longer than those of the neutral water dimer [$r_e(\mathrm{O_2H_5}) = r_e(\mathrm{O_2H_6}) = 0.960$ Å], but shorter than that of the isolated $H_3O^+$ cation [$r_e(\mathrm{OH}) = 0.977$ Å];

6) the non H-bonded OH bond distance of the dimer radical cation [$r_e(\mathrm{O_1H_3}) = 0.978$ Å] is elongated compared to those of the isolated OH radical [$r_e(\mathrm{OH}) = 0.971$ Å] and especially the neutral dimer [$r_e(\mathrm{O_1H_3}) = 0.958$ Å];

7) the non H-bonded HOH bond angle for the $(H_2O)_2{}^+$ radical cation [$\theta_e(\mathrm{H_5O_2H_6}) = 110.2°$] is larger than that for the neutral $(H_2O)_2$ [$\theta_e(\mathrm{H_5O_2H_6}) = 104.8°$], but smaller than that for the isolated $H_3O^+$ cation [$\theta_e(\mathrm{HOH}) = 111.7°$].

### Group B

Structure **6** and **9** (shown in Figure. 3) are similar to the group A structures because of their proton transferred nature, but lack a hydrogen bond. These structures are not minima on the potential energy surface.

## GROUP C

All seven structures in group C (shown in Figure. 4) lack hydrogen bonding between the two $H_2O$ units; they are instead hemi-bonded complexes. Of all group C structures, only **7**, which possesses $C_2$ symmetry, is a local minimum. Comparing the water dimer radical cation **7**, to the neutral water monomer $H_2O$, and the isolated water radical cation $H_2O^+$, there are some notable geometric differences due to complexation:
1) the OH bond distance for the dimer radical cation **7** [$r_e$(OH) = 0.977 Å] is in-between those for $H_2O$ [$r_e$(OH) = 0.959 Å] and $H_2O^+$ [$r_e$(OH) = 1.000 Å];
2) the HOH bond angle for the dimer radical cation **7** [$\theta_e$(HOH) = 105.7°] is in-between those for $H_2O$ [$\theta_e$(HOH) = 104.4°] and $H_2O^+$ [$\theta_e$(HOH) = 109.3°].

The water dimer radical cation **10** is the isomerization transition state connecting **1** and **7**. The transition from **1** to **7** primarily involves the transfer of hydrogen atom 4 from $O_1$ to $O_2$, followed by a rotation of the $H_3$-$O_1$-$H_4$ subunit. To trace the path of this proton transfer reaction within the water dimer radical cation, the intrinsic reaction coordinate (IRC) method was adopted using the aug-cc-pVDZ MP2 method. The schematic potential energy surface (in kcal $mol^{-1}$) is shown pictorially in Figure. 5, where selected geometries along the intrinsic reaction coordinate (IRC) between **1**, **10** and **7** are included. By starting at the transition structure **10** and following the line of steepest decent in the metric of mass-weighted coordinates we confirm that **10** does, indeed, connect structures **1** and **7**. The reaction path shows the hydrogen donor water fragment of the minimum $C_2$ rotates one of its hydrogen atoms toward the hydrogen acceptor water, and rotates another hydrogen away from the acceptor, which connects to the transition state **10**. Then the inner hydrogen moves all the way to the oxygen of the hydrogen acceptor water, which connects to the global minimum **1**.

The other five stationary points in category C were located on the PES using symmetry constraints to the structure.

### 2.4.2 Electron Configurations and Charge Distribution

#### Electron configurations of standard $H_2O$, $H_2O^+$, $(H_2O)_2$, and vertical ionized states of $(H_2O)_2$

The highest occupied molecular orbitals (HOMO) of $H_2O$, $(H_3O)^+$, and $(H_2O)_2$, and the singly occupied molecular orbital (SOMO) of $H_2O^+$ and OH· are shown in Figure. 6.

The ground electronic state of the $H_2O$ monomer $\tilde{X}\ ^1A_1$ ($C_{2v}$) has the electron configuration

[core]$2a_1^2 1b_2^2 3a_1^2 1b_1^2$,

where [core] denotes the lowest-lying core [O: *1s*-like] orbital $1a_1$. The highest occupied molecular orbital (HOMO) $1b_1$ is predominantly the *2p* (out of plane orbital) of the O atom

The ground electronic state of the $H_2O^+$ $2B_1$ ($C_{2v}$) has the electron configuration:

[core]$2a_1^2 3a_1^2 1b_2^2 1b_1$,

where the singly occupied molecular orbital (SOMO) is the $1b_1$ orbital ($2p$ of the oxygen atom) as mentioned above. The ground electronic state of the neutral water dimer $(H_2O)_2$ $\tilde{X}\ ^1$A' ($C_s$) has the electron configuration

[core]$3a'^2 4a'^2 1a''^2 5a'^2 6a'^2 7a'^2 8a'^2 2a''^2$,

where [core] denotes the two lowest-lying core [O: $1s$-like] orbitals $1a'$ and $2a'$. The $7a'$ orbital represents the in-plane O-H bonding orbital which is formed from the proton donor $3a_1$ orbital and the proton acceptor $1b_1$ orbital. The $8a'$ orbital mainly consists of the $O_2$ oxygen $2p$ orbital in the $C_s$ plane, while the $2a''$ (HOMO) orbital represents the $O_1$ oxygen $2p$ orbital perpendicular to the $C_s$ plane. The orbital energy of the $8a'$ orbital ($-0.53$ hartree at the aug-cc-pVQZ RHF level) is significantly lower than that of the $2a''$ orbital ($-0.48$ hartree at the same level).

The lowest energy $\tilde{X}\ ^2$A" ($C_s$) vertical ionized state of the neutral water dimer has the following electron configuration:

[core]$3a'^2 4a'^2 5a'^2 6a'^2 1a''^2 7a'^2 8a'^2 2a''$,

where the $8a'$ and $2a''$ (SOMO) orbital energies are $-0.72$ and $-0.66$ hartree at the aug-cc-pVQZ ROHF level, whereas the $\tilde{A}$ $^2$A' ($C_s$) vertical ionized state of the $(H_2O)_2$ has the electron configuration:

[core]$3a'^2 4a'^2 1a''^2 5a'^2 6a'^2 7a'^2 2a''^2 8a'$,

where the $2a''$ and $8a'$ (SOMO) orbital energies are $-0.93$ and $-0.73$ hartree at the same level.

## Electron configurations of the water dimer radical cation isomers 1 and 7

The singly occupied molecular orbitals (SOMO) of the $(H_2O)_2^+$ isomers **1** and **7** are shown in Figure. 6.

The hydrogen-bonded equilibrium structure **1** of the water dimer radical cation $(H_2O)_2^+$ $\tilde{X}$ $^2$A ($C_1$) in Group A has the following electron configuration:

[core]$3a^2 4a^2 5a^2 6a^2 7a^2 8a^2 9a^2 10a$,

where [core] denotes the two lowest-lying core [O: 1$s$-like] orbitals $1a$ and $2a$. The single electron occupying the $10a$ orbital "experiences" predominantly $O_1$ oxygen $2p$ character. The hemi-bonded structure **7** of the water dimer radical cation $(H_2O)_2^+$ $^2$B ($C_2$) has the following electron configuration:

[core]$2a^2 2b^2 3a^2 3b^2 4a^2 4b^2 5a^2 5b$,

where the $5b$ orbital (SOMO) also has $O_1$ oxygen $2p$ character. For this isomer there is the possibility of symmetry breaking of the ROHF reference wave function.[70–73] In particular, the SOMO may have a propensity to localize on either oxygen atom. We consider this problem in more detail when discussing the vibrational frequencies of isomer **7**.

## Charge distributions of the neutral water dimer and the water dimer radical cation isomers 1 and 7

NPA atomic populations[74–76] for the neutral water dimer and the water dimer radical cation isomers **1** and **7** are reported in Figure. 7. In order to form the cation, one electron

must be removed from the electron-rich $O_1$ $2p$ orbital in neutral water dimer. There are two possibilities for charge redistribution to prevent $O_1$ from carrying a positive charge. The lowest energy isomer **1** results from atom $H_4$ migrating toward atom $O_2$ to form $H_3O^+$, and OH·, which are bound by a hydrogen bond. The other option is for the monomers to reorient and equally share the charge.

This will lead to isomer **7**, which has $C_2$ symmetry. The NPA results of isomer **1** and **7** with ROHF reference agree with those with UHF reference.

### 2.4.3 Harmonic vibrational analyses: comparison to related experiments

The 12 harmonic vibrational frequencies for the different structures of $(H_2O)_2{}^+$ at the aug-cc-pVQZ CCSD(T) level of theory are presented in Table 2. The harmonic vibrational frequencies for the two minima **1** and **7** with the six different basis sets at the CCSD and CCSD(T) levels of theory are provided as Table III of supplementary materials, the IR intensities at the cc-pVTZ CCSD level of theory are also included.

Accompanying the formation of the water dimer, six additional low frequency vibrational motions are generated. Due to low energy barriers along those six vibrational modes, a number of stationary points have been located on the potential energy surface, specifically incorporating symmetry constraints for the dimer.

Among the five structures (**1** – **5**) in Group A ($H_2O$–$H^+ \cdots OH$ hydrogen-bonded system), isomer **1** is found to be the equilibrium structure, **2**, **3**, and **4** are transition states, and structure **5** is a second-order saddle point. The eigenvectors for the imaginary vibrational frequencies of structures **2** and **3** are associated with $O_1H_3$ group rotations along the $O_1H_4O_2$ axis. Structures **2** and **3** connect the two mirror images of isomer **1** in *trans*− and *cis*− conformation, respectively. The imaginary frequency of structure **4** may be attributed to the constraint on the planar conformation of the $H_3O^+$ fragment, since the eigenvector of this frequency is the pyramidalization mode of $H_3O^+$, leading to **1**. There are two imaginary

frequencies of structure **5**, and the corresponding eigenvectors are related to the tilting of the $O_1H_3$ bond from linearity and the pyramidalization of the planar $H_3O^+$ fragment.

Group B structure **6** ($H_3O^+ \cdots OH$) is found to be a transition state and structure **9** a second-order saddle point. The eigenvector corresponding to the imaginary frequency of structure **6** involves the rotation of the H atoms of the $H_3O^+$ fragment along the $O \cdots O$ axis to form a hydrogen-bonded structure. The two eigenvectors corresponding to imaginary frequencies for structure **9** are related to the rotation of the H atoms along the $O \cdots O$ axis and the pyramidalization of the planar $H_3O^+$ fragment.

Among the seven structures in Group C (the $[H_2O \cdots H_2O]^+$ hemi-bonded system), isomer **7** is found to be a minimum, **8**, **10**, and **11** to be transition states, and structures **12** –**14** to be higher-order saddle points. The normal mode with an imaginary frequency for structure **8** lowers the symmetry from $C_{2h}$ (**8**) to $C_2$ (**7**), while that for structure **11** lowers the symmetry from $C_{2v}$ (**11**) to $C_2$ (**7**). Structure **10** is the transition state for the isomerization reaction between **1** and **7**. The eigenvector of imaginary frequency ($615i$ $cm^{-1}$) lowers the symmetry of **7** from $C_2$ to $C_1$ by shifting the $H_4$ atom towards the $O_2$ atom to form a hydrogen bond.

Among the 12 vibrational modes of all the water dimer radical cations, the four highest frequencies are associated with the four OH stretching motions. Structures **1** – **3** in Group A and structure **6** in Group B all have three HOH bending modes (the next highest frequencies) related to the $H_3O^+$ moiety of the cation, the third one corresponds to the pyramidalization motion including all three OH bonds. While structures **4** and **5** in Group A and structure **9** in Group B present two HOH bending and one out-of-plane motions. The seven structures (**7**, **8**, **10** – **14**) in Group C show two HOH bending motions from each of the $H_2O$ and $H_2O^+$ fragments, respectively.

For the $(H_2O)_2{}^+$ isomer **1** the antisymmetric ($\omega_1 = 3780$ $cm^{-1}$), and symmetric ($\omega_2 = 3702$ $cm^{-1}$) stretches of the $H_3O^+$ fragment, are higher than those for the isolated $H_3O^+$ molecule, whereas they are lower than those for the neutral water dimer. The third OH stretch ($\omega_3 =$ 3666 $cm^{-1}$, OH radical moiety) is lower than that (3738 $cm^{-1}$) of the isolated OH radical,

due to the longer OH bond distance. The shared $O_2H_4$ ($\omega_4$ = 2373 cm$^{-1}$) stretching feature of isomer **1** shows the lowest OH stretching frequency, reflecting the longest OH separation (1.048 Å hydrogen-bonded) in the molecule.

Very recently, Gardenier, Johnson and McCoy (GJM) trapped the nascent [$H_3O^+ \cdot\cdot OH$] exit channel intermediate via Ar-mediated ionization of the neutral water dimer. They characterized the nature of the ion-radical complex using vibrational predissociation spectroscopy of the Ar-tagged species.[27] Gardenier reported the spectra of $H_4O_2^+ \cdot Ar_n$, for one or two argon atoms bound to the $H_3O^+$ end of the [$H_3O^+ \cdot\cdot OH$] complex. The Johnson – McCoy collaboration also computed the harmonic vibrational frequencies of the equilibrium structure at the UMP2/aug-cc-pVDZ level. There are considerable differences between the experimental fundamental and theoretical harmonic frequencies, presumably largely due to anharmonic effects. The comparison of vibrational frequencies (in cm$^{-1}$) from Gardenier, Johnson, and McCoy and our research is shown in Table 3.

For both the one and two argon-bound [$H_3O^+ \cdot\cdot OH$] spectra, there are three peaks corresponding to OH stretching, in the 3200 – 3600 cm$^{-1}$region. The experimental asymmetric OH stretches are at 3408 and 3591 cm$^{-1}$, respectively, for the $(H_2O)_2^+ \cdot Ar_2$ and $(H_2O)_2^+ \cdot Ar$ complexes. This large difference between the above two frequencies reflects the strong interaction of the radical cation with argon. For isomer **1**, from our research, the harmonic asymmetric OH stretch ($\omega_1$) of the $H_3O^+$ fragment at the aug-cc-pVQZ/CCSD(T) level is 3780 cm$^{-1}$, necessarily higher than the observed fundamentals, but in good agreement with the aug-cc-pVDZ/UMP2 harmonic frequencies 3758 cm$^{-1}$ for the no Ar-attatched $(H_2O)_2^+$ [3732 and 3614 cm$^{-1}$ for $(H_2O)_2^+ \cdot Ar_n$ (n = 1 and 2)]. The symmetric stretch harmonic frequency ($\omega_2$ = 3702 cm$^{-1}$) of the $H_3O^+$ fragment at the aug-cc-pVQZ/CCSD(T) level is also in reasonable agreement with the aug-cc-pVDZ/UMP2 result at 3660 cm$^{-1}$ [3450 and 3544 cm$^{-1}$ for $(H_2O)_2^+ \cdot Ar$ and $(H_2O)_2^+ \cdot Ar_2$]. The analogous experimental features for $(H_2O)_2^+ \cdot Ar$ and $(H_2O)_2^+ \cdot Ar_2$ lie at 3392 and 3392 cm$^{-1}$. The third high-frequency peak corresponding to the OH stretch of the OH radical moiety, is observed at 3511 and 3499 cm$^{-1}$ for $(H_2O)_2^+ \cdot Ar$

and $(H_2O)_2^+ \cdot Ar_2$. Our result ($\omega_3$ = 3666 cm$^{-1}$) is in good agreement with GJM's aug-cc-pVDZ/UMP2 harmonic frequency at 3678 cm$^{-1}$ [3685 and 3691 cm$^{-1}$ for $(H_2O)_2^+ \cdot Ar$ and $(H_2O)_2^+ \cdot Ar_2$].

With the introduction of the first and second argon atoms, there is an approximately 100 cm$^{-1}$ blue shift in the shared O$\cdots$H stretch region (1800 – 2000 cm$^{-1}$) of the spectra. This experimental shift is opposite in direction to the shift in the exterior OH stretch [the shared O$\cdots$H stretching frequency in $H_2O)_2^+ \cdot Ar_2$ is higher than that in $H_2O)_2^+ \cdot Ar$]. We predict this O$\cdots$H stretching mode to be at 2373 cm$^{-1}$ for the Ar-free $(H_2O)_2^+$ from the aug-cc-pVQZ/CCSD(T) level, 53 cm$^{-1}$ higher than the aug-cc-pVDZ/UMP2 result for $(H_2O)_2^+$ (2320 cm$^{-1}$), but lower than the aug-cc-pVDZ/UMP2 results for $(H_2O)_2^+ \cdot Ar$ and $(H_2O)_2^+ \cdot Ar_2$ (2475 and 2593 cm$^{-1}$). GJM states that the fundamental in the intracomplex proton-transfer mode appears as a triplet rather than as a single peak. They tentatively assigned this feature to reflect the hindered OH rotational structure of the hydroxyl moiety, built off the fundamental associated with the bridging proton vibration parallel to the O$\cdots$O axis. In our research, among the seven proton-transferred structures in Group A (**1** – **5**) and B (**6** and **9**), four structures (**2** – **4**, and **6**) were found to be transition states, which may be connected to the global minimum **1**. Specifically, three transition states (**2** – **4**) lie no more than 1.44 kcal mol$^{-1}$ (0.60 kcal mol$^{-1}$ with ZPVE corrections) above **1**. Therefore, these low barrier (low imaginary frequency) motions might produce such complicated triplet splitting spectra for the Ar-tagged $(H_2O)_2^+$ complexes, as also suggested by GJM.

In the $(H_2O)_2^+$ vibrational spectrum, there is also a water bend region (1500 – 1600 cm$^{-1}$), which corresponds to the intermolecular (HOH) bend of the hydronium constituent or the off-axis displacement of the shared proton. We predict the corresponding harmonic frequencies at 1719 and 1658 cm$^{-1}$ with aug-cc-pVQZ/CCSD(T) method; while at aug-cc-pVDZ/UMP2 level of theory, GJM computed the two harmonic frequencies at 1696 and 1643 cm$^{-1}$ for the Ar-free $(H_2O)_2^+$.

The four OH stretching frequencies of the hemi-bonded structure **7** fall between the two OH stretching frequencies of the neutral water monomer and those of the water monomer cation, due to the intermediate OH bond distances. The two HOH bending frequencies of **7** again fall between the bending frequencies of $H_2O$ and $H_2O^+$, reflecting the intermediate HOH bond angles. An orbital stability analysis of the ROHF wave function used in the harmonic vibrational frequencies calculation reveals that there is one instability connected to the mixing of SOMO and SOMO $-$ 1. This leads to localization of the SOMO and SOMO $-$ 1 as well as charge localization on the two equivalent oxygen atoms. In order to examine the effect of this orbital instability on the frequencies, we have reoptimized the geometry and recomputed vibrational frequencies for isomer **7** at the UHF UCCSD level using the cc-pVTZ basis set. At this level of theory, the UHF reference does not show any orbital instability and the relative energy and frequencies are in very good agreement with the ROHF-UCCSD results. The UHF UCCSD relative energy deviates from the ROHF-UCCSD value by 0.44 kcal $mol^{-1}$. The largest shift in the vibrational frequencies is found for the HOH wagging (B) mode (676 $cm^{-1}$ for UHF-UCCSD and 660 $cm^{-1}$ for ROHF-UCCSD). Consequently, we believe that for the highly correlated wave functions adopted in the work, there are no significant effects from the instability of the ROHF reference on the energetics and the physical properties of water dimer cation. Table 2 reveals that structures **13** and **14** possess imaginary vibrational frequencies with alarming high magnitudes. To confirm that these are not artifacts of symmetry breaking, we preformed stability analyses on the ROHF reference wavefunctions, confirming their stability. UHF-UCCSD theory yields similar results.

### 2.4.4 Energetics

The schematic potential energy surface [CCSD(T) level with aug-cc-pVQZ basis] for proton-transfer and dissociation processes for the hemi-bonded isomer **7** and the hydrogen-bonded isomer **1** is shown in Figure. 8. The complete list of electronic energies for all stationary points is provided in the supplementary material.

Relative energies (in kcal mol$^{-1}$) of all the stationary points of $(H_2O)_2^+$ with respect to the global minimum of water dimer radical cation (isomer **1**) at the CCSD and CCSD(T) levels with the cc-pVQZ and aug-cc-pVQZ basis sets are presented in Table 4. The energy differences between these 14 stationary points are in the range 0.05  45.5 kcal mol$^{-1}$ with the aug-cc-pVQZ CCSD method, and 0.05 – 44.6 kcal mol$^{-1}$ with the aug-cc-pVQZ CCSD(T) method.

At our highest level of theory, aug-cc-pVQZ CCSD(T), the global minimum of the water dimer radical cation isomer **1** (in group A, hydrogen-bonded system) is predicted to be 7.1 kcal mol$^{-1}$ (8.8 kcal mol$^{-1}$ with the zero point vibrational energy, ZPVE) lower in energy than isomer **7** in Group C (hemi-bonded system). Gill and Radom computed this energy difference to be 8.9 kcal mol$^{-1}$ at the MP4/6-311G(MC)**//MP2/6-31G* level of theory,[55] while Sodupe and Bertran determined the energy difference to be 9.8 kcal mol$^{-1}$ at the MCPF/TZ2P++//MP2/TZ2P++ level of theory,[56] and 7.7 kcal mol$^{-1}$ using DFT.[77] Quite recently, Pieniazek et al. computed the energy difference of the two isomers to be 8.2 kcal mol$^{-1}$ at the CCSD(T)/6-311++G**//EOM-IP-CCSD/6-311++G** level of theory.[1] The energy barrier for the forward (**1** $\rightarrow$ **10** $\rightarrow$ **7**) reaction between the two isomers is here predicted to be 15.1 (also 15.1 with ZPVE correction) kcal mol$^{-1}$ at the aug-cc-pVQZ CCSD(T) level of theory. For the reverse (**7** $\rightarrow$ **10** $\rightarrow$ **1**) reaction the barrier is predicted to be 8.1 (7.4 with ZPVE correction) kcal mol$^{-1}$.

The potential energy surface that connects the hydrogen-bonded isomers **1**, **2** and **3** is extremely flat. The transition states **2** ($trans-C_s$) lies 0.05 kcal mol$^{-1}$, and **3** ($cis-C_s$) is 0.73 kcal mol$^{-1}$ higher in energy than the global minimum **1** at the aug-cc-pVQZ CCSD(T) level. With ZPVE correction, **2** ($trans-C_s$) is 0.06 kcal mol$^{-1}$ lower in energy and **3** ($cis-C_s$) is 0.60 kcal mol$^{-1}$ higher in energy at the same level of theory. Since the imaginary vibrational frequencies of **2** and **3** are only 78 and 158 cm$^{-1}$ (0.22 and 0.45 kcal mol$^{-1}$), such small PES energy differences cannot hinder essentially free $O_1H_3$ rotation about the $O_1H_4O_2$ axis.

The neutral water dimer $(H_2O)_2$ ($^1$A' state with $C_s$ symmetry) obviously has a lower energy than two separated water molecules. This is due to hydrogen bonding, yielding a destabilization of the HOMO orbital of the proton donor and stabilization of the HOMO orbital of the proton acceptor. Removing one electron from the neutral water dimer forms a $^2$A" vertical ionized state, and subsequent geometrical relaxation of the $^2$A" ionic state leads to the structure with the hydrogen atom involved in the hydrogen bonding transferred to the water acceptor molecule.

The binding energies of $(H_2O)_2^+$ with respect to isolated $H_3O^+$ plus OH· and isolated $H_2O^+$ plus $H_2O$ are presented in Table 5. With the aug-cc-pVQZ basis set, the binding energies for the 14 stationary points fall in the range 0.9 – 46.4 kcal mol$^{-1}$ (CCSD), 2.1 – 46.7 kcal mol$^{-1}$ [CCSD(T)] compared to ($H_2O^+$+ $H_2O$) fragments. Therefore, all these stationary points of the water dimer radical cation are at least somewhat more favorable than the isolated $H_2O^+$ and $H_2O$ molecules. The total energy of isolated OH radical and $H_3O^+$ molecules is lower than the isolated $H_2O$ and $H_2O^+$ molecules [24.8 kcal mol$^{-1}$ lower at CCSD and 24.4 kcal mol$^{-1}$ lower at CCSD(T)]. The binding energies for all these stationary points with respect to the fragments ($H_3O^+$+ OH·) are determined to be −23.9 – 21.7 kcal mol$^{-1}$ (CCSD), and −22.3 – 22.3 kcal mol$^{-1}$ [CCSD(T)]. The water dimer radical cation structures **12**, **13**, and **14** have higher energies than the isolated $H_3O^+$ and OH· molecules. The binding energies in Table V confirm that the dissociation of $(H_2O)_2^+$ is more likely going through the oxonium channel ($H_3O^+$+ OH·) rather than the water channel ($H_2O^+$+ $H_2O$), especially considering the structure of **1**.

Relative energies (in eV) of all the stationary points of $(H_2O)_2^+$ with respect to the ground electronic state of the neutral water dimer $\tilde{X}$ $^1$A' at the CCSD and CCSD(T) levels with the cc-pVTZ, cc-pVQZ, aug-cc-pVTZ and aug-cc-pVQZ basis sets are displayed in Table 6. With the aug-cc-pVQZ basis set, the energy differences range 10.74 – 12.71 eV at the CCSD level and 10.84 – 12.77 eV at CCSD(T) level. Including the zero point vibrational

energy (ZPVE) correction, the energy differences are 10.71 – 12.57 eV and 10.81 – 12.63 eV at the CCSD and CCSD(T) levels of theory with the same basis set, respectively.

The adiabatic ionization energy of the water dimer from our study is 10.8 eV (also 10.8 eV with ZPVE correction) using the aug-cc-pVQZ CCSD(T) method, which is in excellent agreement with the experimental adiabatic (threshold) ionization energy of 10.8 – 10.9 eV. The theoretical $^2$A" state vertical ionization energy of 11.9 eV at the same level of theory is in reasonable agreement with the experimental value of 12.1 ± 0.1 eV.[52] This large difference (1.1 eV) between the vertical and adiabatic ionization energies is due to the tremendous change in the equilibrium geometries between the neutral water dimer and the water dimer radical cation. The theoretical vertical ionization energy for the $^2$A' state is 13.2 eV (at the same level of theory), where the experimental value is 13.2 ± 0.2 eV.[52] This IP is significantly higher than the first ionization energy, reflecting the considerable difference in the $2a''$ (−0.48 hartree) and $8a'$ (−0.53 hartree) orbital energies for the neutral water dimer.

## 2.5 Conclusions

*Ab initio* coupled-cluster electronic structure theory has been employed in order to investigate the water dimer radical cation molecules. Fourteen stationary points have been located on the electronic doublet ground state PES. Based on the harmonic vibrational frequency analyses, two minima ($0i$) with $C_1$ and $C_2$ symmetries, 7 transition states ($1i$), and 5 higher order saddle points ($2i$ or more) have been characterized. Stationary point geometries and energetics are very sensitive to basis sets and levels of sophistication. At our highest level of theory, aug-cc-pVQZ CCSD(T), the energy differences among all these radical cation stationary points fall in the range of 44.6 kcal mol$^{-1}$. The global minimum of the water dimer radical cation has been confirmed to be a hydrogen-bonded system with $C_1$ point group symmetry **1**, which lies 7.1 (8.8 with ZPVE correction) kcal mol$^{-1}$ lower in energy than the hemi-bonded isomer **7** with $C_2$ point group symmetry. The dissociation energy of isomer **1** via the oxonium channel [$H_2O$–$H^+ \cdots OH \rightarrow H_3O^+ +$ OH·] has been predicted to be 22.3 (26.4

with ZPVE correction) kcal $mol^{-1}$. The dissociation energy of isomer **7** via the water channel [$(H_2O)_2^+ \rightarrow H_2O^+ + H_2O$] is predicted to be 39.6 (34.7 with ZPVE correction) kcal $mol^{-1}$. The energy barrier for the forward (**1** $\rightarrow$ **10** $\rightarrow$ **7**) isomerization reaction between the two isomers has been determined to be 15.1 (also 15.1 with ZPVE correction) kcal $mol^{-1}$ at the aug-cc-pVQZ CCSD(T) level of theory. Therefore, the dissociation of the water dimer cation is likely to occur via the oxonium channel.

## 2.6 Acknowledgements

The authors would like to thank Dr. Justin M. Turney and Mr. Jeremiah Wilke for insightful discussions and technical expertise. This research was funded by the Department of Energy, Basic Energy Sciences, Division of Chemical Sciences, Fundamental Interactions Team. This research used the resources of the National Energy Research Scientific Computing Center (NERSC), supported by the Office of Science of the U.S. Department of Energy under Contract No. DE-AC02-05CH11231.

Table 2.1: Optimized geometrical parameters of $(H_2O)_2$ and the fourteen stationary points of $(H_2O)_2{}^+$ at the aug-cc-pVQZ CCSD(T) level of theory. Bond lengths are in Å, bond angles and dihedral angles are in degrees.

| | Structure | $r_{O_1O_2}$ | $r_{O_2H_4}$ | $\theta_{O_2H_4O_1}$ | $\theta_{H_5O_2H_4}$ | $\tau_{H_4O_1O_2H_3}$ | $\tau_{H_5O_1O_2H_4}$ | $\tau_{H_6O_1O_2H_4}$ |
|---|---|---|---|---|---|---|---|---|
| $(H_2O)_2$ | $C_s$ | 2.910 | 1.951 | 171.6 | 110.9 | 0.0 | 122.9 | $-122.9$ |
| **1** | $C_1$ | 2.506 | 1.048 | 173.4 | 112.8 | $-39.7$ | $-154.5$ | $-28.3$ |
| **2** | $trans$-$C_s$ | 2.513 | 1.049 | 177.4 | 113.0 | 0.0 | 117.8 | $-117.8$ |
| **3** | $cis$-$C_s$ | 2.508 | 1.046 | 169.9 | 114.0 | 0.0 | $-66.6$ | 66.63 |
| **4** | planar $C_s$ | 2.469 | 1.054 | 172.1 | 122.8 | 0.0 | 0.0 | 180.0 |
| **5** | planar $C_{2v}$ | 2.548 | 1.006 | 180.0 | 121.1 | 0.0 | – | – |
| **6** | $C_s$ | 2.548 | 0.974 | 30.3 | 112.5 | 180.0 | $-83.3$ | 83.3 |
| **7** | $C_2$ | 2.024 | 2.296 | 61.7 | 123.0 | 106.6 | $-156.7$ | 96.8 |
| **8** | $C_{2h}$ | 2.029 | 2.342 | 59.5 | 120.5 | 106.2 | 180.0 | 73.8 |
| **9** | planar $C_{2v}$ | 2.511 | 0.966 | 0.0 | 122.5 | 0.0 | – | – |
| **10** | $C_1$ | 2.210 | 1.715 | 106.2 | 130.5 | 104.5 | $-133.7$ | 118.4 |
| **11** | $cis$-bifurcated $C_{2v}$ | 2.505 | 3.172 | 38.5 | 50.4 | 180.0 | 90.0 | $-90.0$ |
| **12** | $trans$-bifurcated $C_{2v}$ | 2.693 | 3.373 | 38.8 | 124.4 | 180.0 | 90.0 | $-90.0$ |
| **13** | $D_{2h}$ | 1.897 | 2.511 | 41.4 | 138.6 | 180.0 | 180.0 | 0.0 |
| **14** | planar $C_{2v}$ | 2.173 | 2.150 | 78.3 | 152.0 | 180.0 | 180.0 | 0.0 |

Table 2.2: Harmonic vibrational frequencies (in $cm^{-1}$) of the neutral water dimer $(H_2O)_2$ and the fourteen stationary points of water dimer radical cation $(H_2O)_2{}^+$ at the aug-cc-pVQZ CCSD(T) level of theory.

| | $\omega_1$ | $\omega_2$ | $\omega_3$ | $\omega_4$ | $\omega_5$ | $\omega_6$ | $\omega_7$ | $\omega_8$ | $\omega_9$ | $\omega_{10}$ | $\omega_{11}$ | $\omega_{12}$ |
|---|---|---|---|---|---|---|---|---|---|---|---|---|
| $H_2O$ | 3940 | 3831 | 1649 | | | | | | | | | |
| $H_2O^+$ | 3440 | 3383 | 1474 | | | | | | | | | |
| $H_3O^+$ | 3699 | 3699 | 3600 | 1699 | 1699 | 896 | | | | | | |
| OH | 3738 | | | | | | | | | | | |
| neutral | 3931 | 3912 | 3825 | 3748 | 1671 | 1651 | 618 | 354 | 186 | 151 | 143 | 127 |
| **1** | 3780 | 3702 | 3666 | 2373 | 1719 | 1658 | 1050 | 617 | 503 | 400 | 360 | 98 |
| **2** | 3776 | 3700 | 3662 | 2364 | 1675 | 1651 | 1157 | 625 | 447 | 439 | 359 | $78i$ |
| **3** | 3787 | 3708 | 3668 | 2403 | 1670 | 1649 | 1111 | 579 | 454 | 452 | 357 | $158i$ |
| **4** | 3872 | 3769 | 3663 | 2254 | 1692 | 1568 | 784 | 618 | 396 | 375 | 148 | $521i$ |
| **5** | 3864 | 3764 | 3738 | 3033 | 1674 | 1621 | 584 | 475 | 334 | 330 | $476i$ | $620i$ |
| **6** | 3728 | 3720 | 3628 | 3588 | 1680 | 1655 | 1016 | 403 | 289 | 284 | 246 | $349i$ |
| **7** | 3713 | 3711 | 3638 | 3594 | 1611 | 1585 | 804 | 653 | 637 | 631 | 481 | 67 |
| **8** | 3709 | 3708 | 3637 | 3592 | 1621 | 1584 | 808 | 654 | 641 | 631 | 477 | $52i$ |
| **9** | 3841 | 3762 | 3728 | 3650 | 1609 | 1557 | 468 | 321 | 285 | 257 | $328i$ | $663i$ |
| **10** | 3815 | 3702 | 3575 | 3351 | 1610 | 1545 | 637 | 511 | 465 | 412 | 302 | $615i$ |
| **11** | 3865 | 3783 | 3337 | 3270 | 1685 | 1461 | 465 | 454 | 348 | 332 | 172 | $600i$ |
| **12** | 3908 | 3817 | 3472 | 3404 | 1679 | 1462 | 328 | 290 | 173 | $162i$ | $252i$ | $576i$ |
| **13** | 3884 | 3883 | 3710 | 3672 | 1497 | 1130 | 565 | 545 | 532 | $330i$ | $1096i$ | $1244i$ |
| **14** | 3869 | 3816 | 3756 | 3558 | 1573 | 568 | 523 | 353 | 81 | $383i$ | $603i$ | $2042i$ |

Table 2.3: Comparison of the present water dimer radical cation vibrational frequencies ($cm^{-1}$) with those of Gardenier, Johnson, and McCoy.[27] The latter authors also report results for $(H_2O)_2{}^+ \cdot Ar_n$ (n=0, 1 and 2). The theoretical frequencies are harmonic, while the experimental frequencies are fundamentals.

| mode | motion | $(H_2O)_2^+$ | | $(H_2O)_2^+ \cdot Ar$ | | $(H_2O)_2^+ \cdot Ar_2$ | |
|---|---|---|---|---|---|---|---|
| | | CCSD(T) aug-cc-pVQZ | UMP2 aug-cc-pVDZ | Experiment | UMP2 aug-cc-pVDZ | Experiment | UMP2 aug-cc-pVDZ |
| $\nu_{\phi}$ | | 98 | 99 | | 89 | | 89 |
| $\nu_{bend}$ | | 1658 | 1643 | 1543 | 1635 | 1601 | 1644 |
| $\nu_{sp(\perp)}$ | | 1719 | 1696 | | 1699 | | 1697 |
| $\nu_{sp(\parallel)}$ |  | 2373 | 2320 | 1863<br>1975<br>2078 | 2479 | 1916<br>2021<br>2155 | 2601 |
| $\nu_{OH_2}^{sym}$ |  | 3702 | 3660 | 3392 | 3534 | 3392 | 3538 |
| $\nu_{OH}$ |  | 3666 | 3678 | 3511 | 3685 | 3499 | 3692 |
| $\nu_{OH_2}^{asym}$ | 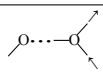 | 3780 | 3758 | 3591 | 3732 | 3408 | 3607 |

Table 2.4: Relative energies (in kcal $mol^{-1}$, ZPVE corrected values in parentheses) of the fourteen stationary points of the water dimer radical cation $(H_2O)_2^+$ with respect to isomer **1** at the CCSD and CCSD(T) levels.

| | CCSD/cc-pVQZ | CCSD/aug-cc-pVQZ | CCSD(T)/cc-pVQZ | CCSD(T)/aug-cc-pVQZ |
|---|---|---|---|---|
| **1** | 0.00 (0.00) | 0.00 (0.00) | 0.00 (0.00) | 0.00 (0.00) |
| **2** | 0.04 (−0.07) | 0.05 (−0.06) | 0.04 (−0.08) | 0.05 (−0.06) |
| **3** | 0.74 (0.58) | 0.71 (0.58) | 0.75 (0.60) | 0.73 (0.60) |
| **4** | 1.37 (0.26) | 1.39 (0.27) | 1.42 (0.29) | 1.44 (0.31) |
| **5** | 4.19 | 4.18 | 5.29 | 5.24 |
| **6** | 6.30 | 6.25 | 6.75 | 6.67 |
| **7** | 10.15 (12.01) | 9.90 (11.74) | 7.41 (9.14) | 7.09 (8.80) |
| **8** | 10.15 (11.94) | 9.90 (11.69) | 7.41 (9.05) | 7.10 (8.72) |
| **9** | 8.68 | 8.62 | 9.26 | 9.17 |
| **10** | 16.81 (16.99) | 16.65 (16.49) | 15.37 (15.41) | 15.14 (15.14) |
| **11** | 20.34 (19.35) | 20.27 (19.23) | 20.27 (19.25) | 20.18 (19.10) |
| **12** | 36.59 | 36.11 | 36.85 | 36.29 |
| **13** | 36.75 | 36.38 | 34.71 | 34.24 |
| **14** | 45.89 | 45.52 | 45.09 | 44.63 |

Table 2.5: Relative energies (in kcal mol$^{-1}$, ZPVE corrected values in parentheses) of the fourteen stationary points of water dimer radical cation $(H_2O)_2{}^+$ with respect to the water ($H_2O^+ + H_2O$) and the oxonium ($H_3O^+ + OH$) dissociation channels at the CCSD and CCSD(T) levels using the aug-cc-pVQZ basis set.

| | Structure | ($H_2O^+$-$H_2O$) | | ($H_3O^+$-OH) | |
|---|---|---|---|---|---|
| | | CCSD/ aug-cc-pVQZ | CCSD(T)/ aug-cc-pVQZ | CCSD/ aug-cc-pVQZ | CCSD(T)/ aug-cc-pVQZ |
| **1** | $C_1$ | 46.43 (43.20) | 46.68 (43.52) | 21.66 (25.69) | 22.31 (26.38) |
| **2** | $trans$-$C_s$ | 46.38 (43.26) | 46.64 (43.58) | 21.61 (25.75) | 22.27 (26.43) |
| **3** | $cis$-$C_s$ | 45.71 (42.62) | 45.96 (42.92) | 20.94 (25.11) | 21.59 (25.77) |
| **4** | planar $C_s$ | 45.03 (42.93) | 45.24 (43.21) | 20.26 (25.42) | 20.88 (26.06) |
| **5** | planar $C_{2v}$ | 42.25 | 41.44 | 17.48 | 17.07 |
| **6** | $C_s$ | 40.18 | 40.01 | 15.41 | 15.64 |
| **7** | $C_2$ | 36.53 (31.46) | 39.59 (34.72) | 11.76 (13.95) | 15.22 (17.57) |
| **8** | $C_{2h}$ | 36.53 (31.51) | 39.59 (34.80) | 11.76 (14.00) | 15.22 (17.65) |
| **9** | planar $C_{2v}$ | 37.81 | 37.51 | 13.04 | 13.14 |
| **10** | $C_1$ | 29.78 (26.71) | 31.54 (28.39) | 5.01 (9.20) | 7.17 (11.24) |
| **11** | $cis$-bifurcated $C_{2v}$ | 26.16 (23.97) | 26.50 (24.42) | 1.39 (6.46) | 2.13 (7.27) |
| **12** | $trans$-bifurcated $C_{2v}$ | 10.31 | 10.39 | -14.45 | -13.98 |
| **13** | $D_{2h}$ | 10.05 | 12.45 | -14.72 | -11.92 |
| **14** | planar $C_{2v}$ | 0.90 | 2.05 | -23.87 | -22.32 |

Table 2.6: Relative energies (in eV, ZPVE corrected values in parentheses) of the $^2$A" and $^2$A' vertical ionized states of the neutral water dimer and the fourteen stationary points of water dimer radical cation $(H_2O)_2{}^+$ with respect to the ground electronic state of the neutral water dimer at the CCSD and CCSD(T) levels.[a]

| | CCSD/ aug-cc-pVQZ | CCSD(T)/ aug-cc-pVQZ | CCSD/ aug-cc-pVQZ | CCSD(T) aug-cc-pVQZ |
|---|---|---|---|---|
| $(H_2O)_2$ | 0.00 (0.00) | 0.00 (0.00) | 0.00 (0.00) | 0.00 (0.00) |
| $^2$A' | 13.22 | 13.28 | 13.16 | 13.21 |
| $^2$A" | 11.71 | 11.77 | 11.78 | 11.85 |
| **1** | 10.66 (10.63) | 10.74 (10.72) | 10.74 (10.72) | 10.84 (10.81) |
| **2** | 10.66 | 10.74 | 10.75 | 10.84 |
| **3** | 10.69 | 10.77 | 10.78 | 10.87 |
| **4** | 10.72 | 10.80 | 10.81 | 10.90 |
| **5** | 10.84 | 10.92 | 10.97 | 11.06 |
| **6** | 10.93 | 11.01 | 11.04 | 11.13 |
| **7** | 11.10 (11.15) | 11.17 (11.23) | 11.07 (11.11) | 11.14 (11.19) |
| **8** | 11.10 | 11.17 | 11.07 | 11.14 |
| **9** | 11.03 | 11.11 | 11.15 | 11.23 |
| **10** | 11.39 | 11.46 | 11.41 | 11.49 |
| **11** | 11.54 | 11.62 | 11.62 | 11.71 |
| **12** | 12.24 | 12.30 | 12.34 | 12.41 |
| **13** | 12.25 | 12.32 | 12.25 | 12.32 |
| **14** | 12.65 | 12.71 | 12.70 | 12.77 |

[a] Experimental value = 10.8 – 10.9 eV from Ref. 14.

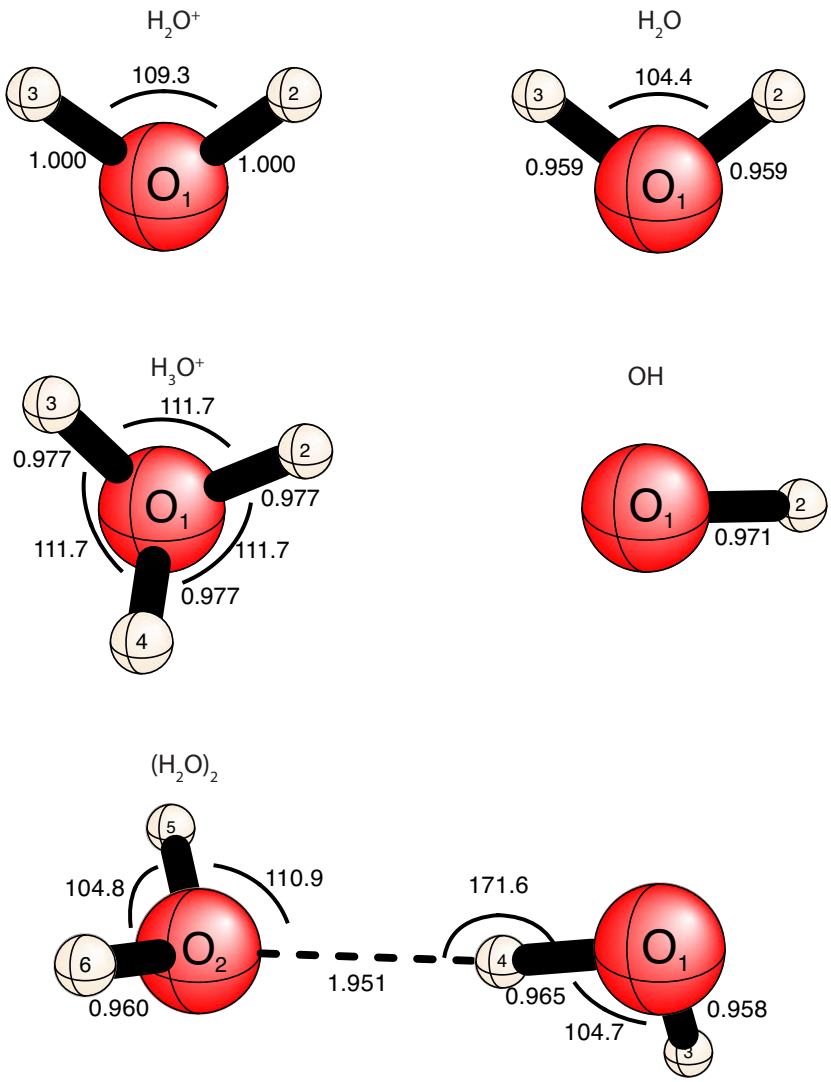


Figure 2.1: Geometries of the water radical cation, water, hydronium, hydroxyl radical, and the neutral water dimer predicted at the CCSD(T) level of theory using the aug-cc-pVQZ basis set. Bond distances are in Å and bond angles in degrees.

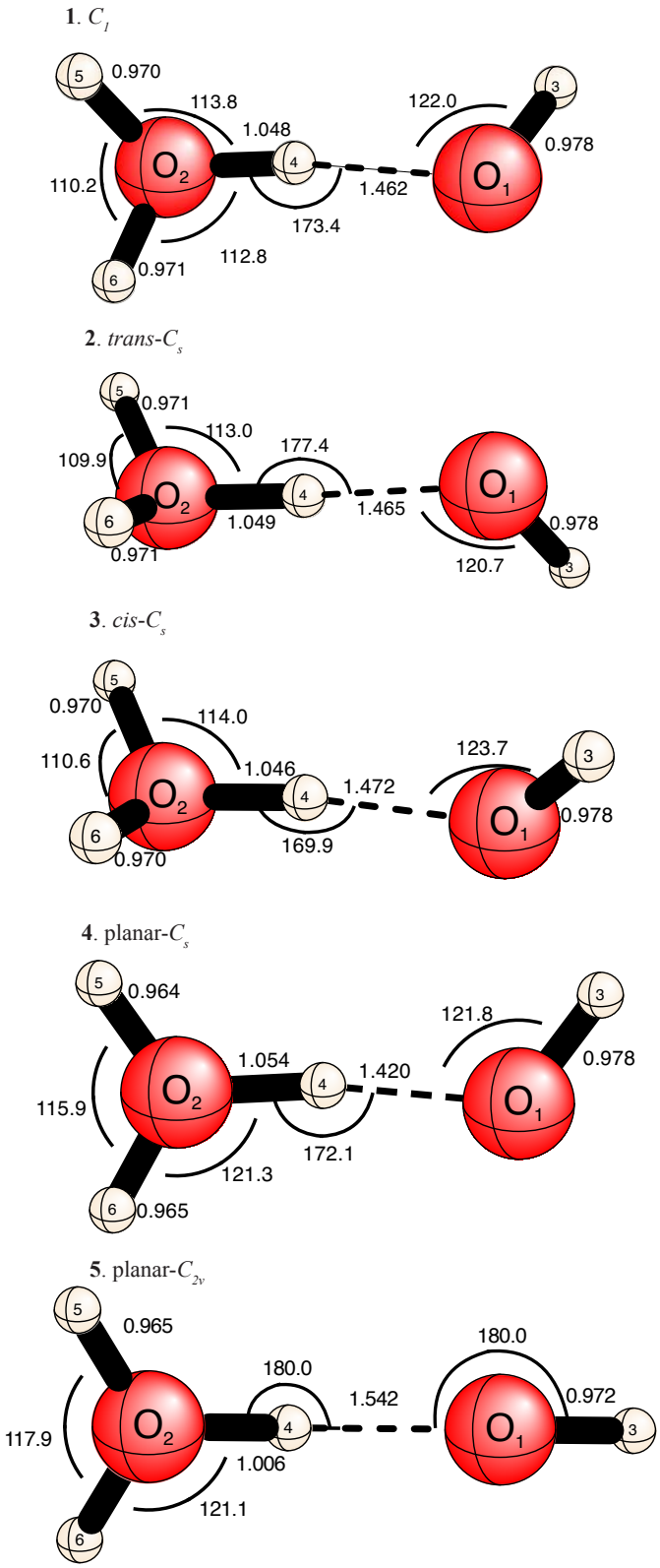


Figure 2.2: Geometries of the water dimer radical cation structures **1** – **5** predicted at the CCSD(T) level of theory using the aug-cc-pVQZ basis set. Bond distances are in Å and bond angles in degrees.

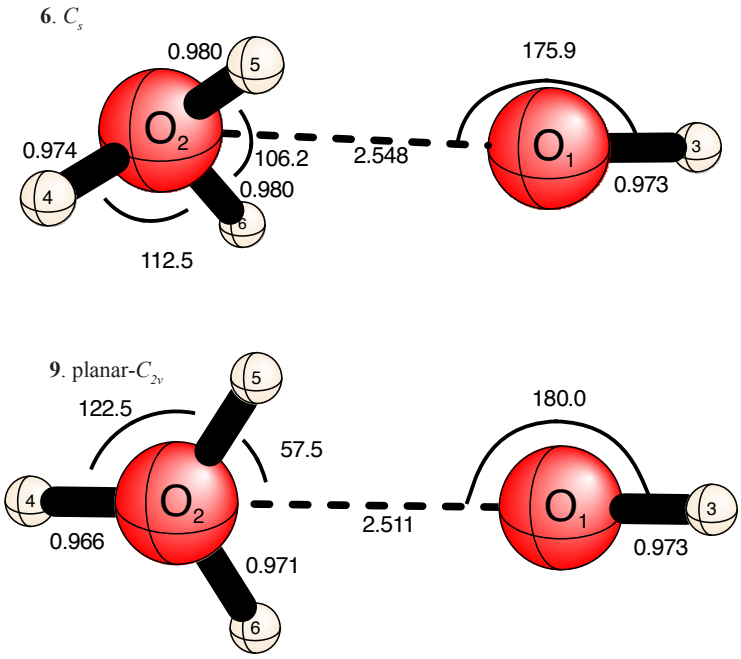


Figure 2.3: Geometries of the water dimer radical cation structures 6 and 9 predicted at the CCSD(T) level of theory using the aug-cc-pVQZ basis set. Bond distances are in  and bond angles in degrees.

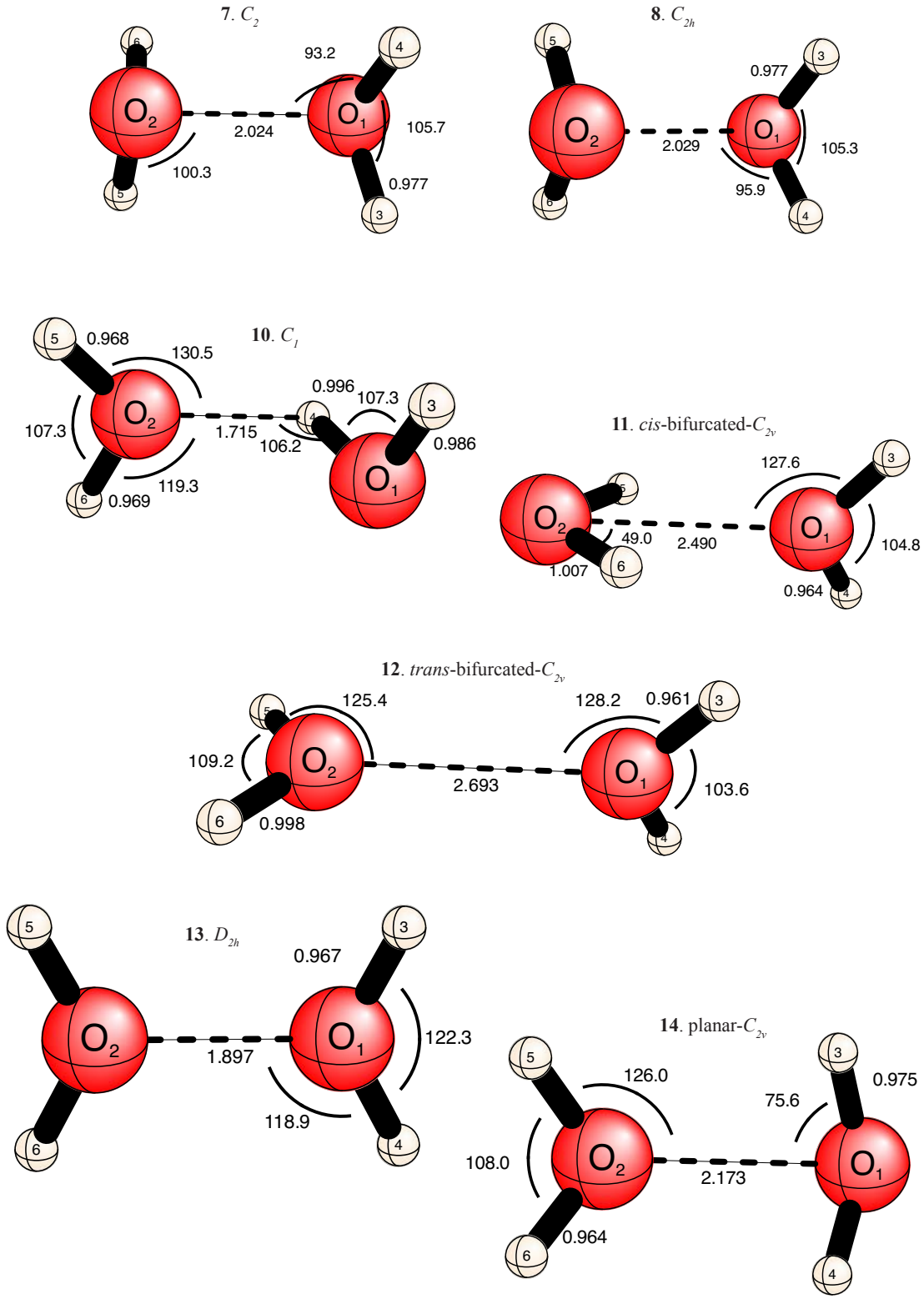


Figure 2.4: Geometries of the water dimer radical cation structures **7**, **8** and **10** – **14** predicted at the CCSD(T) level of theory using the aug-cc-pVQZ basis set. Bond distances are in Å and bond angles in degrees.

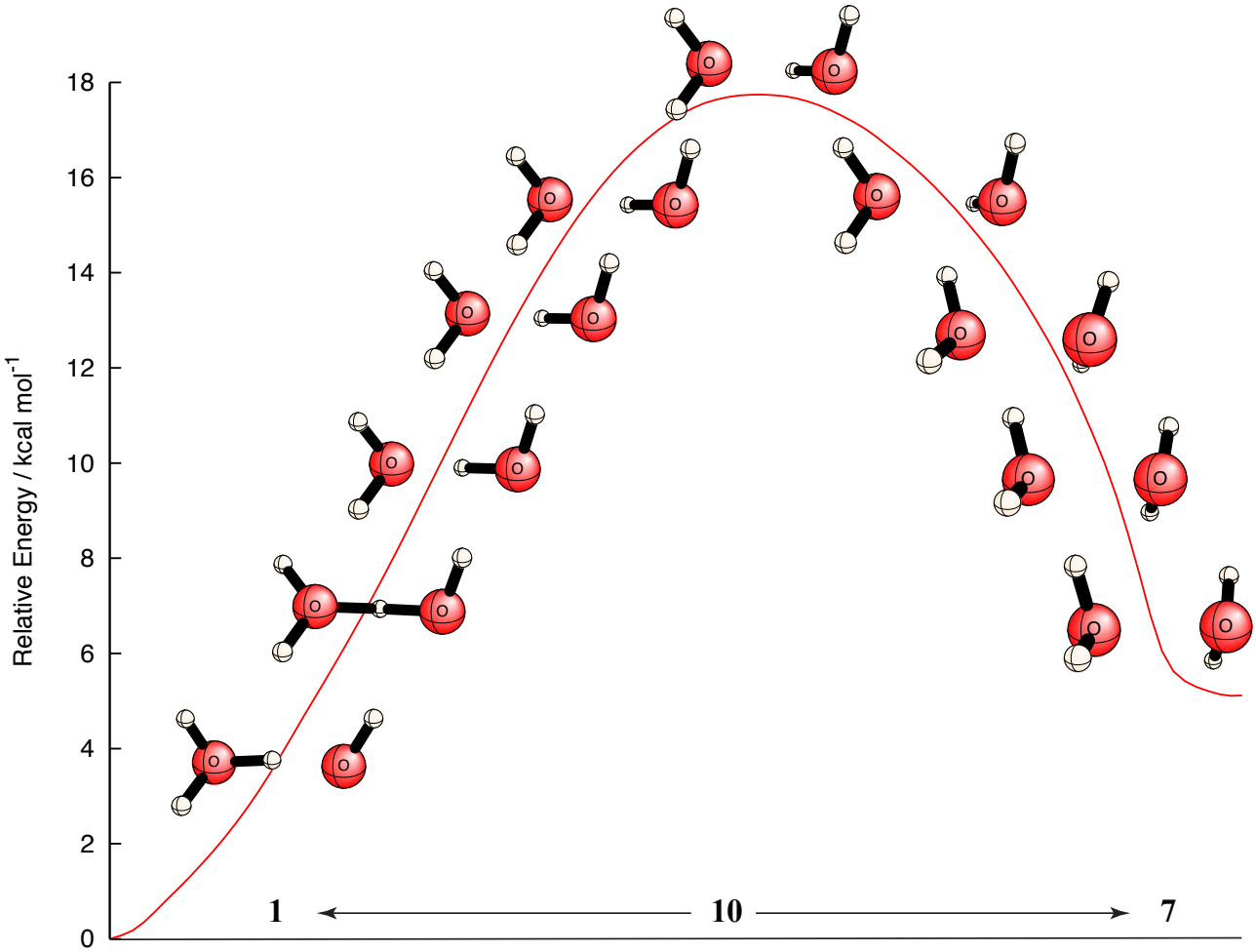


Figure 2.5: Intrinsic reaction coordinate (IRC) for the proton-transfer process involving water dimer radical cation structures **1**, **7** and **10** at the aug-cc-pVDZ MP2 level of theory.

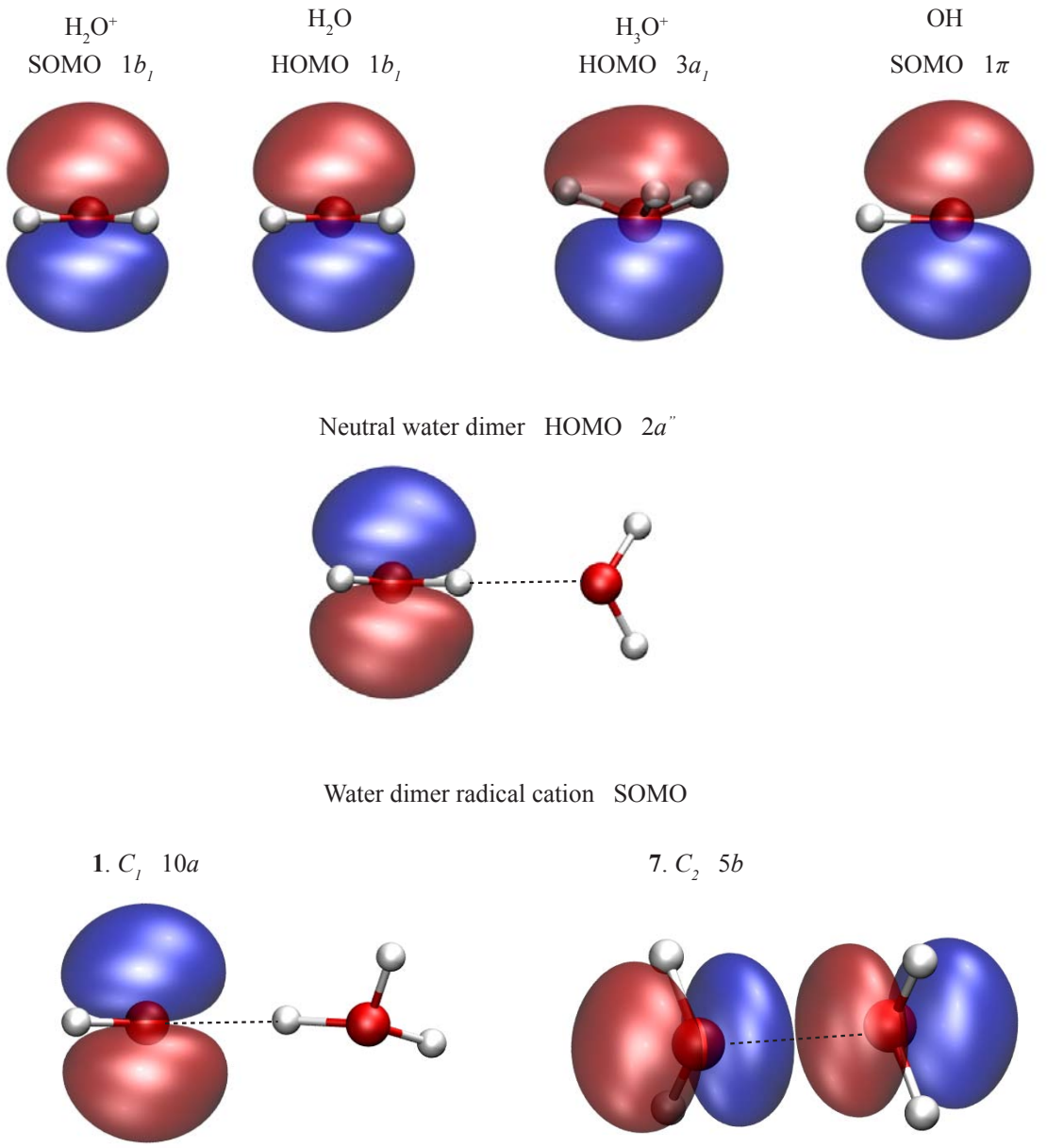


Figure 2.6: Singly occupied molecular orbitals (SOMO) of $H_2O^+$, OH, and the $(H_2O)_2^+$ equilibria **1** and **7**. Also shown are the highest occupied molecular orbitals (HOMO) of $H_2O$, $H_3O^+$, and the $(H_2O)_2$.

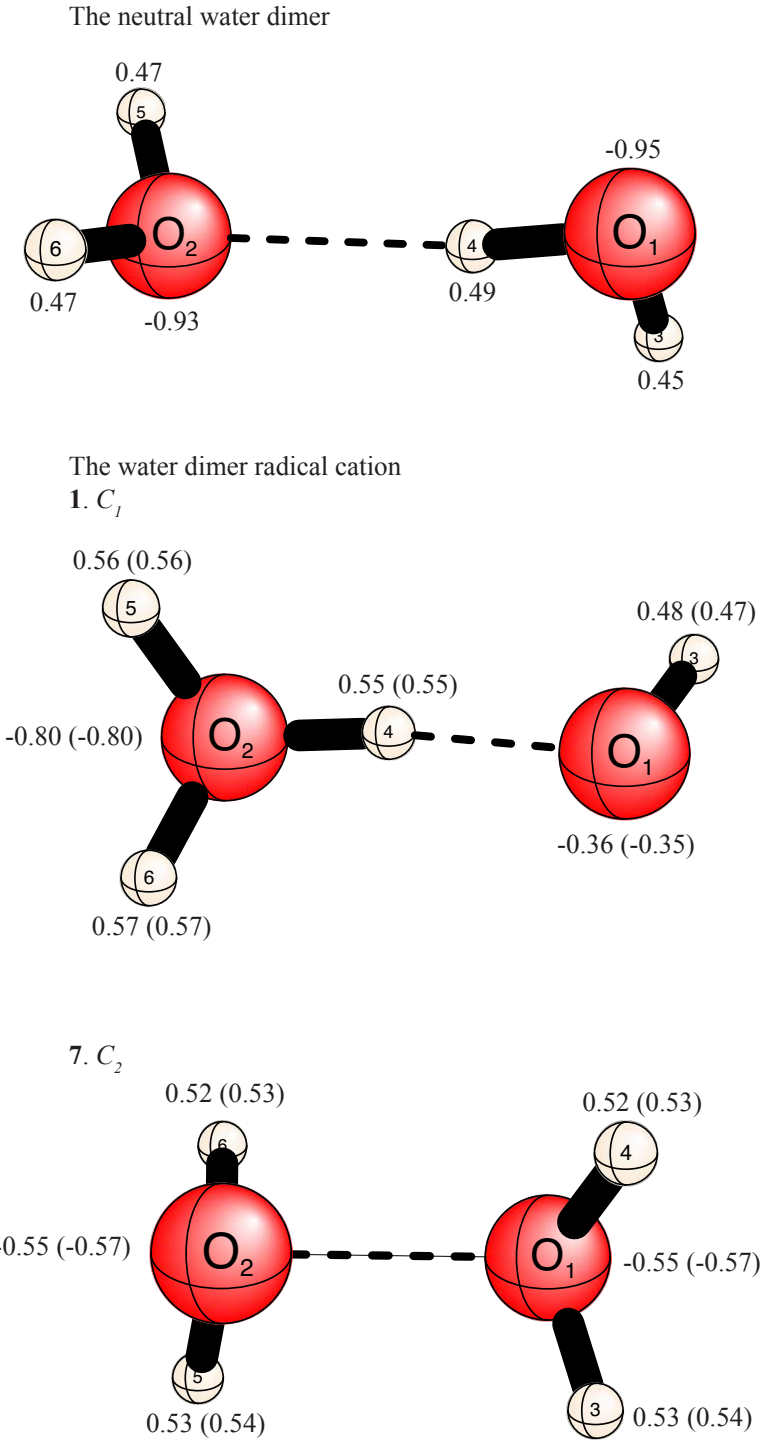


Figure 2.7: NPA atomic populations for the neutral water dimer and the water dimer radical cation isomers **1** and **7** with ROHF reference (values with UHF reference are in parentheses).

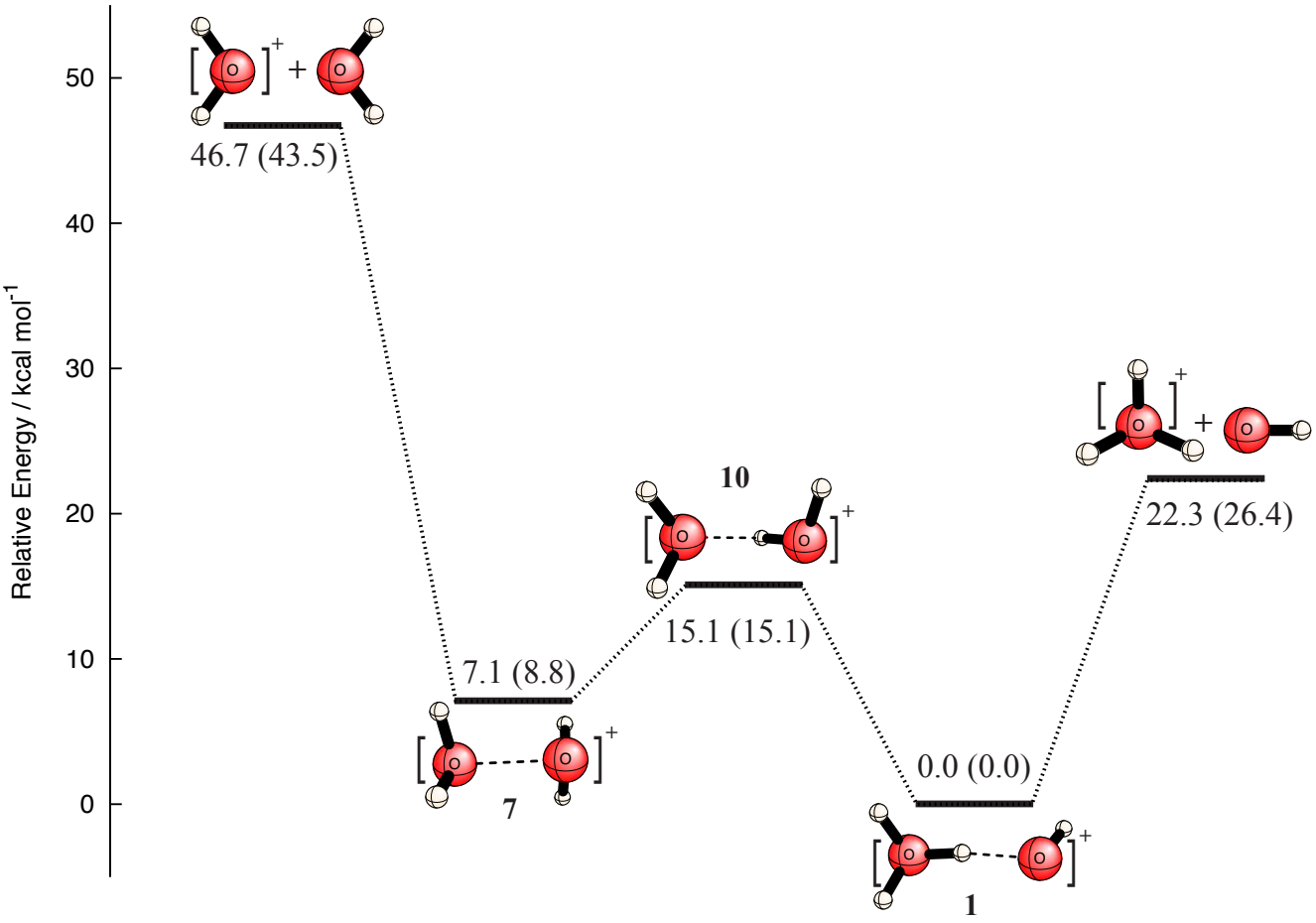


Figure 2.8: Schematic potential energy surface (in kcal $mol^{-1}$, ZPVE corrected values in parentheses) showing proton-transfer and dissociation processes for the hemi-bonded and hydrogen-bonded water dimer radical cation structures **1**, **7** and **10** at the aug-cc-pVQZ CCSD(T) level of theory.

## Bibliography


[1] P. A. Pieniazek, J. VandeVondele, P. Jungwirth, A. I. Krylov, and S. E. Bradforth, J. Phys. Chem. A **112**, 6159 (2008).

[2] P. A. Pieniazek, E. J. Sundstrom, S. E. Bradforth, and A. I. Krylov, J. Phys. Chem. A **113**, 4423 (2009).

[3] K. Liu, J. D. Cuzan, and R. J. Saykally, Science **271**, 929 (1996).

[4] A. W. J. Castleman and K. H. J. Bowen, J. Phys. Chem. **100**, 12911 (1996).

[5] R. N. Barnett, U. Landman, and C. L. Cleveland, J. Chem. Phys. **88**, 4421 (1988).

[6] R. N. Barnett, U. Landman, and C. L. Cleveland, J. Chem. Phys. **88**, 4429 (1988).

[7] Y. V. Novakovskaya and N. F. Stepanov, J. Phys. Chem. **103**, 3285 (1999).

[8] Z. Su, M. Buhl, and W. Zhou, J. Am. Chem. Soc. **131**, 8697 (2009).

[9] H. P. Kaukonen, R. N. Barnett, and U. Landman, J. Chem. Phys. **97**, 1365 (1992).

[10] C. E. Klots and R. N. Compton, J. Chem. Phys. **69**, 1644 (1978).

[11] H. Shinohara, N. Nishi, and N. Washida, J. Chem. Phys. **84**, 5561 (1986).

[12] C. Y. Ng, D. J. Trevor, P. W. Tiedemann, S. T. Ceyer, P. L. Kronebusch, B. H. Mahan, and Y. T. Lee, J. Chem. Phys. **67**, 4235 (1977).

[13] H. Haberland and H. Z. Langosch, Phys. D **2**, 243 (1986).

[14] S. P. DeVisser, L. J. DeKoning, and N. M. M. Nibbering, J. Phys. Chem. **99**, 15444 (1995).

[15] A. W. J. Castleman, Springer Series in Chemical Physics **56**, 77 (1994).

[16] L. Angel and A. J. Stace, Chem. Phys. Lett. **345**, 277 (2001).

[17] S. Yamaguchi, S. Kudoh, Y. Kawai, Y. Okada, T. Orii, and K. Takeuchi, Chem. Phys. Lett. **377**, 37 (2003).

[18] A. A. Golubeva, P. A. Pieniazek, and A. I. Krylov, J. Chem. Phys. **130**, 124113 (2009).

[19] A. B. McCoy, X. Huang, S. Carter, and J. M. Bowman, J. Chem. Phys. **123**, 064317 (2005).

[20] L. R. McCunn, J. R. Roscioli, M. A. Johnson, and A. B. McCoy, J. Phys. Chem. B **112**, 321 (2008).

[21] A. B. McCoy, Int. Rev. Phys. Chem. **25**, 77 (2006).

[22] M. W. Crofton, J. M. Price, and Y. T. Lee, Springer Series in Chemical Physics **56**, 44 (1994).

[23] A. J. Stace, Phys. Rev. Lett. **61**, 306 (1988).

[24] A. J. Stace, Chem. Phys. Lett. **174**, 103 (1990).

[25] U. Buck and M. Winter, Z. Phys. D **31**, 291 (1994).

[26] R. N. Barnett and U. Landman, J. Phys. Chem. **99**, 17305 (1995).

[27] G. Gardenier, M. A. Johnson, and A. B. McCoy, J. Phys. Chem. **113**, 4772 (2009).

[28] C. P. Schulz and J. V. Hertel, Springer Series in Chemical Physics **56**, 7 (1994).

[29] R. N. Barnett and U. Landman, Phys. Rev. Lett. **70**, 1775 (1993).

[30] N. I. Hammer, E. G. Diken, J. R. Roscioli, M. A. Johnson, E. M. Myshakin, K. D. Jordan, A. B. McCoy, X. Huang, J. M. Bowman, and S. Carter, J. Chem. Phys. **122**, 244301 (2005).

[31] M. J. Frisch, J. E. Del Bene, J. S. Binkley, and H. F. Schaefer, J. Chem. Phys. **84**, 2279 (1986).

[32] R. N. Barnett, H. P. Cheng, H. Hakkinen, and U. Landman, J. Phys. Chem. **99**, 7731 (1995).

[33] E. F. Valeev and H. F. Schaefer, J. Chem. Phys. **108**, 7197 (1998).

[34] S. Tomoda, Y. Achiba, and K. Kimura, Chem. Phys. Lett. **87**, 197 (1982).

[35] F. Dong, S. Heinbuch, J. J. Rocca, and E. R. Bernstein, J. Chem. Phys. **124**, 224319 (2006).

[36] K. H. Bowen and J. G. Eaton, *The Structure of Small Molecules and Ions*, 147 (New York, 1988).

[37] J. V. Coe, G. H. Lee, J. G. Eaton, S. T. Arnold, H. W. Sarkas, K. H. Bowen, C. Ludewigt, H. Haberland, and D. R. Worsnop, J. Chem. Phys. **92**, 3980 (1990).

[38] G. H. Lee, S. T. Arnold, J. G. Eaton, H. W. Sarkas, K. H. Bowen, C. Ludewigt, and H. Haberland, Z. Phys. D **20**, 9 (1991).

[39] C. Desfrancois, N. Khelifa, J. P. Schermann, J. G. Eaton, and K. H. Bowen, J. Chem. Phys. **95**, 7760 (1991).

[40] K. D. Jordan, Science **306**, 618 (2004).

[41] A. E. Bragg, J. R. R. Verlet, A. Kammrath, O. Cheshnovsky, and D. M. Neumark, Science **306**, 669 (2004).

[42] P. Ayotte and M. A. Johnson, J. Chem. Phys. **106**, 811 (1997).

[43] A. D. Bailey and R. S. Narcisi, J. Geophys. Res. **70**, 3687 (1965).

[44] S. Wei, Z. Shi, and A. W. J. Castleman, J. Chem. Phys. **94**, 3268 (1991).

[45] S. Tomoda and K. Kimura, Chem. Phys. **82**, 215 (1983).

[46] R. N. Barnett and U. Landman, J. Phys. Chem. A **101**, 164 (1997).

[47] G. S. Tschumper, M. L. Leininger, B. C. Hoffman, E. F. Valeev, H. F. Schaefer, and M. Quack, J. Chem. Phys. **116**, 690 (2002).

[48] S. Tomoda and K. Kimura, Chem. Phys. Lett. **111**, 434 (1984).

[49] H. Tachikawa, J. Phys. Chem. **106**, 6159 (2002).

[50] I. G. Gurtubay, N. D. Drummond, M. D. Towler, and R. J. Needs, J. Chem. Phys. **124**, 24318 (2006).

[51] B. J. Smith, D. J. Swanton, J. A. Pople, H. F. Schaefer, and L. Radom, J. Chem. Phys. **92**, 1240 (1990).

[52] K. Sato, S. Tomoda, K. Kimura, and S. Iwata, Chem. Phys. Lett. **95**, 579 (1983).

[53] T. K. Ghanty and S. K. Ghosh, J. Phys. Chem. **106**, 11815 (2002).

[54] H. M. Lee and K. S. Kim, J. Chem. Theory Comput. **5**, 976 (2009).

[55] P. M. W. Gill and L. Radom, J. Am. Chem. Soc. **110**, 4931 (1987).

[56] M. Sodupe, A. Oliva, and J. Bertran, J. Am. Chem. Soc. **116**, 8249 (1994).

[57] T. D. Crawford and H. F. Schaefer, Reviews in Computational Chemistry **14**, 33 (2000).

[58] M. Rittby and R. J. Bartlett, J. Phys. Chem. **92**, 3033 (1988).

[59] G. D. Purvis and R. J. Bartlett, J. Chem. Phys. **76**, 1910 (1982).

[60] G. E. Scuseria, Chem. Phys. Lett. **176**, 27 (1991).

[61] K. Raghavachari, G. W. Trucks, J. A. Pople, and M. Head-Gordon, Chem. Phys. Lett. **157**, 479 (1989).

[62] T. H. Dunning, J. Chem. Phys. **90**, 1007 (1989).

[63] R. A. Kendall, T. H. Dunning, and R. J. Harrison, J. Chem. Phys. **96**, 6796 (1992).

[64] D. Cremer, *Møller-Plesset Perturbation Theory*, vol. 3 (Wiley: Chichester, 1998).

[65] Y. Shao, L. Fusti-Molnar, Y. Jung, J. Kussmann, C. Ochsenfeld, S. T. Brown, A. T. B. Gilbert, L. V. Slipchenko, S. V. Levchenko, D. P. O'Neill, R. A. D. Jr., R. C. Lochan, T. Wang, G. J. O. Beran, N. A. Besley, J. M. Herbert, C. Y. Lin, T. V. Voorhis, S. H. Chien, A. Sodt, R. P. Steele, V. A. Rassolov, P. E. Maslen, P. P. Korambath, R. D. Adamson, B. Austin, J. Baker, E. F. C. Byrd, H. Dachsel, R. J. Doerksen, A. Dreuw, B. D. Dunietz, A. D. Dutoi, T. R. Furlani, S. R. Gwaltney, A. Heyden, S. Hirata, C. P. Hsu, G. Kedziora, R. Z. Khalliulin, P. Klunzinger, A. M. Lee, M. S. Lee, W. Liang, I. Lotan, N. Nair, B. Peters, E. I. Proynov, P. A. Pieniazek, Y. M. Rhee, J. Ritchie, E. Rosta, C. D. Sherrill, A. C. Simmonett, J. E. Subotnik, H. L. W. III, W. Zhang, A. T. Bell, A. K. Chakraborty, D. M. Chipman, F. J. Keil, A. Warshel, W. J. Hehre, H. F. Schaefer, J. Kong, A. I. Krylov, P. M. W. Gill, and M. Head-Gordon, Phys. Chem. Chem. Phys. **8**, 3172 (2006).

[66] H.-J. Werner, P. J. Knowles, R. Lindh, F. R. Manby, M. Schütz, P. Celani, T. Korona, G. Rauhut, R. D. Amos, A. Bernhardsson, A. Berning, D. L. Cooper, M. J. O. Deegan, A. J. Dobbyn, F. Eckert, C. Hampel, G. Hetzer, A. W. Lloyd, S. J. McNicholas, W. Meyer, M. E. Mura, A. Nicklass, P. Palmieri, R. Pitzer, U. Schumann, H. Stoll, A. J. Stone, R. Tarroni, and T. Thorsteinsson, Molpro, version 2006.1, a package of ab initio programs.

[67] J. F. Stanton, J. Gauss, J. D. Watts, W. J. Lauderdale, and R. J. Bartlett, Int. J. Quantum Chem. **44 (S26)**, 879 (1992).

[68] J. F. Stanton, J. Gauss, J. D. Watts, P. G. Szalay, R. J. Bartlett with contributions from A. A. Auer, D. E. Bernholdt, O. Christiansen, M. E. Harding, M. Heckert,

O. Heun, C. Huber, D. Jonsson, J. Jusélius, W. J. Lauderdale, T. Metzroth, C. Michauk, D. P. O'Neill, D. R. Price, K. Ruud, F. Schiffmann, A. Tajti, M. E. Varner, J. Vázquez and the integral packages: MOLECULE (J. Almlöf and P. R. Taylor), PROPS (P. R. Taylor), and ABACUS (T. Helgaker, H. J. Aa. Jensen, P. Jørgensen, and J. Olsen). Current version see http://www.aces2.de.

[69] T. D. Crawford, C. D. Sherrill, E. F. Valeev, J. T. Fermann, R. A. King, M. L. Leininger, S. T. Brown, C. L. Jassen, E. T. Seidl, J. P. Kenny, and W. D. Allen, J. Comp. Chem. **28**, 1610 (2007).

[70] Y. Yamaguchi, I. L. Alberts, J. D. Goddard, and H. F. Schaefer, Chem. Phys. **147**, 309 (1990).

[71] T. D. Crawford, J. F. Stanton, W. D. Allen, and H. F. Schaefer, J. Chem. Phys. **107**, 10626 (1997).

[72] N. A. Burton, Y. Yamaguchi, I. L. Alberts, and H. F. Schaefer, J. Chem. Phys. **95**, 7466 (1991).

[73] Jensen, *Computational Molecular Spectroscopy* (John Wiley & Sons, LTD., 2000).

[74] A. Szabo and N. S. Ostlund, *Modern Quantum Chemistry: Introduction To Advanced Electronic Structure Theory* (Dover: New York, 1998).

[75] A. E. Reed, R. B. Weinstock, and F. Weinhold, J. Chem. Phys. **83**, 735 (1985).

[76] A. E. Reed and F. Weinhold, J. Chem. Phys. **78**, 4066 (1983).

[77] M. Sodupe, J. Bertran, L. Rodriguez-Santiago, and E. J. Baerends, J. Phys. Chem. **103**, 166 (1999).

# CHAPTER 3

## CHARACTERIZATION OF THE BNNO RADICAL[†]

[†]Reproduced with permission from [Qianyi Cheng, Andrew C. Simmonett, Francesco A. Evangelista, Yukio Yamaguchi and Henry F. Schaefer, III, *J. Chem. Theory Comput.*, 2010, **6**, 1915-1923] Copyright [2010] American Chemical Society.

## 3.1 Abstract

The cyclic, *trans*, and *cis* BNNO molecules and the two isomerization reactions on their doublet electronic states potential energy surface (PES) are systematically investigated. *Ab initio* self-consistent field (SCF), complete active space self-consistent field (CASSCF), coupled cluster with single and double excitations (CCSD), and CCSD including perturbative triple excitations [CCSD(T)] quantum mechanical techniques were employed, in conjunction with Dunning's correlation consistent polarized valence basis sets (cc-pV$X$Z and aug-cc-pV$X$Z, where $X$ = D, T, and Q). All stationary points located on the doublet PES lie within 19 kcal mol$^{-1}$ of the global minimum cyclic isomer at the aug-cc-pVQZ CCSD(T) level of theory. The cyclic and *trans* minima are separated by 2.4 kcal mol$^{-1}$ with an interconversion barrier (cyclic $\rightarrow$ TS2 $\rightarrow$*trans*) of 18.3 kcal mol$^{-1}$; *trans* and *cis* isomers are separated by 10.4 kcal mol$^{-1}$ with a barrier (*trans* $\rightarrow$ TS1 $\rightarrow$ *cis*) of 10.4 kcal mol$^{-1}$. The dissociation energies BNNO ($\tilde{X}\ ^2A'$) $\rightarrow$ B ($^2P_u$) + NNO ($\tilde{X}\ ^1\Sigma^+$) for the cyclic, *trans*, and *cis* isomers are predicted to be 39.7, 37.3, and 27.0 kcal mol$^{-1}$, respectively. The diatomic fragment dissociation energies BNNO ($\tilde{X}\ ^2A'$) $\rightarrow$ BN ($X\ ^3\Pi$) + NO ($X\ ^2\Sigma^+$) for the three isomers are determined to be 50.7, 48.4, and 38.0 kcal mol$^{-1}$, respectively. Additionally, fundamental vibrational frequencies are computed for the cyclic and *trans* isomers through application of second-order vibrational perturbation theory (VPT2) at the cc-pCVTZ CCSD(T) level of theory. Comparison of the resulting vibrational frequencies and their isotopic shifts with those determined experimentally by Wang and Zhou yields the surprising result that the B ($^2P_u$) + NNO ($\tilde{X}\ ^1\Sigma^+$) reaction leads to formation of the *trans* isomer. The latter structure is not the global minimum, rather the second lowest lying isomer. This apparent disparity is rationalized by detailed examination of the PES describing this reaction.

## 3.2 Introduction

In the past few decades, boron nitrides have attracted much attention since they have various technical applications in nuclear technology, the semiconductor industry, and the steel industry, taking advantage of their mechanical, thermal, and electrical properties as well as their chemical inertness.[1,2] For the amount of energy stored in a given system or region of space per unit volume,

or per unit mass, boron is well known for its high energetic density, among many kinds of propellant additives.[3] Therefore, boron has potential applications as an advanced fuel in propulsion systems.[4] During the burning of boron-containing propellants, some portions of boron are oxidized to boron oxide releasing a large amount of energy, while some boron nitride (BN) is formed.[5,6]

As an important molecule in atmospheric chemistry, nitrous oxide ($N_2O$) has also received considerable attention and interest. In chemical industry, nitrous oxide is an effective oxidation agent.[7–23] Many experiments indicate that nitrous oxide is also important in the thermal decomposition of various propellants.[3] $N_2O$ is often used as a catalytic species for burn-rate modification of nitramine propellants as well.[24,25]

The reaction of boron and nitrous oxides and the resulting intermediate generation is an intriguing topic. In 2007, Wang and Zhou reported a combined matrix isolation infrared (IR) spectroscopic and theoretical study of the BNNO and AlNNO molecules.[26] The BNNO and AlNNO molecules were prepared via the reactions of laser-evaporated boron and aluminum atoms with nitrous oxide ($N_2O$) in solid argon and were identified on the basis of isotopically substituted IR absorptions as well as theoretical (density functional theory) calculations. From co-deposition of laser-evaporated isotopic-enriched $^{10}B$ atoms with 0.5% $N_2O$ in argon matrix, a group of new IR absorptions at 1837.0, 1502.3, 838.2, and 633.8 $cm^{-1}$ were observed, along with strong $N_2O$ absorptions. These four absorptions were assigned to the B-N stretching (1837.0 $cm^{-1}$), N-O stretching (1502.3 $cm^{-1}$), N-N stretching (838.2 $cm^{-1}$), and in plane bending (633.8 $cm^{-1}$) modes of the $^{10}BNNO$ molecule.[1] The experiment was repeated with naturally abundant boron atoms, yielding absorptions at 1795.7, 1500.3, 836.5, and 626.9 $cm^{-1}$ with IR intensities approximately four times stronger than the above mentioned absorptions. The latter vibrational features were assigned to the corresponding modes of the $^{11}BNNO$ molecule. In order to confirm their findings, Wang and Zhou carried out B3LYP DFT computations with the 6-311+G* basis set; the BNNO molecule was predicted to have a $^2A'$ ground electronic state with a planar *trans* structure.

Wang, Li, Zhang, Sheng, and Yu reported a theoretical study of boron nitride (BN) generated from the boron atom and several nitrogen oxides.[3] BN is one of the products formed in the burning of boron-containing propellant. Possible mechanisms for the reactions of boron and nitrogen oxides (NO, $NO_2$, and $N_2O$) were investigated using the G2-MP2 method. The reactions of the ground state

boron atom B ($^2P_u$) with nitrogen oxides were determined to be endothermic, while the reactions of an excited quartet state of the boron atom B ($^4P_g$) and nitrogen oxides are exothermic, and the BN product can be formed. For the BN formation reaction B ($^4P_g$) + $N_2O \rightarrow$ BN + NO, two *trans* and two *cis* forms of the BNNO molecule were located on the quartet potential energy surface (PES). Among the four, one *trans* and one *cis* forms were found as the reaction intermediates and the other *trans* and *cis* BNNO structures were characterized as transition states from the intermediates to the final products (BN + NO).

In this study we make the first attempt to theoretically interpret the experimentally observed vibrational frequencies by explicitly considering the effects of anharmonicity. Furthermore, we extend the previous studies of the potential energy surface by employing significantly more reliable methodologies and reveal a previously neglected isomer which, surprisingly, is revealed to be the global minimum.

## 3.3 THEORETICAL METHODS

In this work, six correlation-consistent basis sets cc-pV$X$Z and aug-cc-pV$X$Z, where $X$ = D, T, and Q, developed by Dunning and co-workers[27,28] were employed. *Ab initio* theoretical techniques included restricted open-shell Hartree-Fock (ROHF), unrestricted Hartree-Fock (UHF), complete active space self-consistent field (CASSCF),[29,30] spin-unrestricted coupled cluster with single and double excitations (UCCSD),[31,32] and UCCSD with perturbative triple excitations [UCCSD(T)].[33–35] For the unrestricted coupled cluster computations, an ROHF reference wave function was used to control spin contamination. Computations were performed with the MOLPRO program suite,[36] the Mainz-Austin-Budapest (MAB) version of the ACESII program suite,[37,38] and PSI3[39] quantum chemistry suite packages.

The four core orbitals (1$s$-like orbitals of B, N, and O) were frozen in all correlated calculations. The $T_1$ diagnostic values[40] of the five stationary points are 0.027 (cyclic isomer), 0.022 (*trans* isomer), 0.035 (*cis* isomer), 0.032 (TS1), and 0.034 (TS2) at the cc-pVQZ UCCSD(T) optimized geometries. Analytic and numerical gradient methods were used to optimize geometries and to determine the dipole moments, harmonic vibrational frequencies, and associated IR intensities. Vibrational anharmonicities were computed by application of second-order perturbation theory[41–48]

(VPT2) to the quartic force field. The GRENDEL[49] program was used to compute the force constants in internal coordinates, while INTDER2005[50–54] was used to perform the nonlinear transformation of the force constants from the internal to Cartesian coordinates. The ANHARM[53,55] program was adopted for the VPT2 analysis.

## 3.4 Results and Discussion

### 3.4.1 CASSCF Wave Functions

The electron configurations of the the linear NNO ($\tilde{X}\ ^1\Sigma^+$) and the cyclic, *trans*, *cis* BNNO isomers, as well as the two isomerization reaction transition states (TS1 and TS2) connecting them are shown in supplementary material Table S1. The five highest-lying occupied molecular orbitals (MO) of the five stationary points of BNNO molecule and the linear NNO molecule are depicted in supplementary material Figures S1−S6.[56]

In order to analyze correlation effects on the geometrical parameters and physical properties, full valence (19e/16MO) cc-pVQZ CASSCF wave functions were constructed for the five stationary points at the cc-pVQZ UCCSD(T) optimized geometries. There are 17,705,688 configuration state functions (CSFs) in $C_s$ point group symmetry. Furthermore, since multi-reference character might be present, given the moderately large $T_1$ diagnostics, we will examine the contributions of the reference wave function and important excited configurations. Therefore, the CI coefficients based on natural orbitals (NOs), presented in Table S2, are employed in the following discussion.

For cyclic BNNO, the $(2a'')^2 \rightarrow (3a'')^2$ double excitation provides the most significant correction to the reference configuration. For *trans* BNNO, the three most significant contributions to the CASSCF wave function come from the $(2a'')^2 \rightarrow (3a'')^2$, $(11a')^2 \rightarrow (13a')^2$, and $(1a'')^2 \rightarrow (4a'')^2$ double excitations relative to the reference configuration. A major contribution to the CASSCF wave function for *cis* isomer comes from the $(13a)^2 \rightarrow (15a)^2$ double excitation. Similar to the *cis* isomer, the primary contribution to the CASSCF wave function of TS1 comes from the $(13a)^2 \rightarrow (15a)^2$ double excitation, and the two important additional contributions are the $(12a)^2 \rightarrow (16a)^2$ and $(11a)(13a) \rightarrow (14a)(15a)$ double excitations. It should be noted that the CI coefficient of the reference configuration for the TS1 transition state ($C_1 = 0.912$) is the same as the *cis*

isomer, but smaller than those for the cyclic and *trans* isomers. For TS2, three important double excitations, $(2a'')^2 \rightarrow (3a'')^2$, $(11a')^2 \rightarrow (11a')(12a')(13a')$, and $(11a')^2 \rightarrow (13a')^2$ contribute to the CASSCF wave function. The CI coefficient of the reference configuration for the TS2 transition state ($C_1 = 0.914$) is smaller than those of the cyclic and *trans* isomers, as a result of the elongated bonds in the transition state. Despite the significant presence of some excited configurations, the reference CI coefficients should be large enough in all cases for single reference coupled cluster theory to be reliable.

### 3.4.2 Geometries

The optimized geometries for the five stationary points of the BNNO molecule are presented in Figure 1 and Table S3.

In the following discussion we used the most reliable aug-cc-pVQZ CCSD(T) geometries for all species, with the exception of TS1, for which we encountered difficulties. Notwithstanding the change (0.5°) in $\theta_e$(BNN) for the *cis* isomer, which has a very flat potential surface, it is evident from Table S3 that the aug-cc-pVQZ and cc-pVQZ geometries are nearly identical. In part for this reason, it was decided not to further pursue the aug-cc-pVQZ CCSD(T) geometry for TS1; instead we performed a single point energy computation at this level of theory using the cc-pVQZ CCSD(T) geometry, anticipating negligible error in the resulting barrier height.

The $r_e$(BN) bond distances in the five stationary points of the BNNO molecule are all predicted to be 1.417−1.437 Å, except for the *trans* minimum. These 1.4 Å values are very close to those of the boron and nitrogen containing three-membered rings from Richard and Ball's theoretical work[57] [1.410 Å for both *trans* and *cis* diazaboridine, and 1.420 Å for boradiazirine computed at the 6-31G(d,p) B3LYP level], in which B−N being a single bond. The *trans* BNNO isomer has the shortest BN bond distance of 1.257 Å, which may be attributed to the two BN $\pi$-bonding (out-of-plane $2a''$ MO and in-plane $11a'$ MO) orbitals shown in Figure S2. This bond length is shorter than those for BN ($X\ ^3\Pi$) (1.330 Å), which is considered to have the character between a double and a triple bond, and BN ($a\ ^1\Sigma^+$) (1.277 Å),[58] which is considered as a triple bond.

The N−N bond distances of the cyclic and *trans* minima are 1.351 Å and 1.373 Å, respectively, much longer than those of isolated nitrous oxide (N−N triple bond[59] 1.129 Å) and diazene (N−N

double bond 1.252 Å), much shorter than those of *cis* diazaboridine (1.585 Å)[57] and hydrazine (1.460 Å)[?], and close to that predicted for boradiazirine (1.300 Å)[57] at the B3LYP 6-31G(d,p) level. Therefore, the NN bonds in the cyclic and *trans* isomers fall between single and double bonds. For the *cis* minimum and the TS1 transition state, the N−N bond lengths are very close to diazene.

All of the O−N bond distances fall in the range 1.181 Å − 1.201 Å for the five stationary points. These values are much longer than that for ($X\ ^2\Pi$) diatomic nitric oxide (1.153 Å). Except for TS2, the O−N bond distances of the other four stationary points are also slightly longer than that for $N_2O$ (1.188 Å).

The equilibrium bond angle $\theta_e$(BNN) of the *trans* isomer is predicted to be the largest, around 164°, which suggests near *sp* hybridization for the B and N atoms. On the other hand, the bond angle $\theta_e$(NNO) of the *trans* isomer is determined to be the smallest among the five stationary points, about 114°, indicating something between $sp^2$ and $sp^3$ N and O hybridization. For the *cis* isomer, the bond angles $\theta_e$(BNN) and $\theta_e$(NNO) are predicted to be 137.4° and 134.7°, respectively. These geometrical features indicate a combination of *sp* and $sp^2$ hybridization for the B and N atoms, and the same type of hybridization for the O and N atoms in the *cis* isomer.

### 3.4.3 Intrinsic Reaction Coordinate (IRC)

Intrinsic reaction coordinate (IRC) analyses[61–64] are commonly used to ascertain the nature of transition states; this requires locating a reaction coordinate which is achieved by following appropriately mass-weighted energy gradients. The torsional motion that connects the *cis* and *trans* BNNO isomers has an extremely flat potential in the vicinity of the transition states, as exemplified by the small *cis* BNNO−TS1 separation of just 0.06 kcal $mol^{-1}$; this makes gradient-following algorithms susceptible to numerical error. Instead we manually varied the torsional angle, which is the primary contributor to the reaction coordinate, relaxing all other degrees of freedom to construct a potential energy curve at the cc-pVTZ CCSD(T) level of theory. This analysis, which is displayed in Figure 2, shows that the *cis* isomer does not reside in a deep enough potential well to be feasibly isolable and its formation would immediately be followed by isomerization to *trans* BNNO. The region of Figure 2 around the $C_1$ *cis* BNNO minimum reveals that equilibrium structure of

this isomer is ill-defined, as isomerization between the two equivalent $C_1$ minima occurs through a $C_s$ symmetry transition state that is almost isoenergetic.

The transition state connecting the cyclic and *trans* BNNO minima is much more well-defined, and its cc-pVDZ MP2 IRC is plotted in Figure 3. For the forward reaction (cyclic → TS2 → *trans*), the $BN_3N_2$ bond angle (see Figure 1 for atom numbering) of the cyclic isomer gradually opens up and the NN bond distance decreases toward TS2. At the transition state the $BN_2$ bond distance [1.839 Å with the aug-cc-pVQZ CCSD(T) method] is significantly elongated compared to that (1.437 Å with the same method) of the cyclic isomer. From the transition state (TS2) to the *trans* isomer, there is a cleavage of the $BN_2$ bond, followed by shortening of the $BN_3$ bond distance.

### 3.4.4 Relative Energies

The relative energies of the five stationary points are presented in Table 1. At the SCF level of theory the *trans* isomer is predicted to be the energetically lowest-lying isomer. However, at the coupled cluster levels of theory the cyclic isomer is found to be the global minimum on the ground state surface. With the aug-cc-pVQZ CCSD(T) method, the *trans* BNNO structure is predicted to be higher in energy than the cyclic minimum, by 3.5 kcal $mol^{-1}$ [2.4 kcal $mol^{-1}$ with zero point vibrational energy (ZPVE) correction], but lower in energy than the *cis* isomer by 10.6 kcal $mol^{-1}$ (10.4 kcal $mol^{-1}$ with ZPVE). The schematic potential energy surface at this level is shown in Figure 4.

The barrier height for the forward cyclic-*trans* isomerization reaction (cyclic→TS2→*trans*) is determined to be 19.7 kcal $mol^{-1}$ (18.3 kcal $mol^{-1}$ with ZPVE), while the reaction barrier for the reverse reaction (*trans*→TS2→cyclic) is predicted to be 16.2 kcal $mol^{-1}$ (15.9 kcal $mol^{-1}$ with ZPVE). Since the isomerization barrier heights are relatively high, the reaction may not happen at an appreciable rate in an argon matrix at 12K, and would be highly dependent upon boron tunneling. This cyclic−*trans* isomerization reaction will be addressed again later in the manuscript.

The reaction barrier for the forward *trans-cis* rotational (out-of-plane) isomerization reaction (*trans*→TS1→*cis*) was predicated to be 10.8 (10.4) kcal $mol^{-1}$. On the other hand there is almost no barrier [0.2 kcal $mol^{-1}$ (0.0 kcal $mol^{-1}$ with ZPVE correction)] for the reverse isomerization reaction

(*cis*→TS1→*trans*). Consequently, the existence of the *cis* isomer in a solid argon matrix (at 12K) seems questionable.

### 3.4.5 Dissociation Energies

The two BNNO dissociation limits at the aug-cc-pVQZ CCSD(T) level of theory are shown schematically in Figure 4.

#### 1. BNNO ($\tilde{X}\ ^2A'$) → B ($^2P_u$) + NNO ($\tilde{X}\ ^1\Sigma^+$)

The dissociation energies BNNO ($\tilde{X}\ ^2A'$) → B ($^2P_u$) + NNO ($\tilde{X}\ ^1\Sigma^+$) for the three BNNO isomers are presented in Table 2. With the aug-cc-pVQZ basis set the dissociation energy (ZPVE corrected values in parentheses) for the cyclic minimum is predicted to be 30.5 (28.5) (SCF), 38.3 (36.2) (CCSD), and 41.3 (39.7) kcal mol$^{-1}$ [CCSD(T)]. For the *trans* isomer the three corresponding values are 34.0 (32.8) (SCF), 36.8 (35.6) (CCSD), and 37.8 (37.3) kcal mol$^{-1}$ [CCSD(T)], while those for the *cis* isomer to be 11.9 (11.3) (SCF), 23.6 (23.4) (CCSD), and 27.3 (27.0) kcal mol$^{-1}$ [CCSD(T)]. With inclusion of correlation effects the dissociation energies increase relative to the SCF method by 11.2 (cyclic), 4.5 (*trans*), and 15.7 (*cis*) kcal mol$^{-1}$, respectively. The *cis* isomer is more favored energetically by correlation effects compared to the two dissociation products. It is seen that the B ($^2P_u$) + NNO ($\tilde{X}\ ^1\Sigma^+$) dissociation pathways are endothermic for all three BNNO isomers (see Figure 4).

#### 2. BNNO ($\tilde{X}\ ^2A'$) → BN ($X\ ^3\Pi$) + NO ($X\ ^2\Sigma^+$)

The dissociation energies BNNO ($\tilde{X}\ ^2A'$) → BN ($X\ ^3\Pi$) + NO ($X\ ^2\Sigma^+$) for the three BNNO isomers are reported in Table 2. The dissociation energy with the ZPVE correction for the cyclic minimum is 13.6 (SCF), 44.6 (CCSD), and 50.7 kcal mol$^{-1}$ [CCSD(T)]. For the *trans* isomer the dissociation energy is determined to be 17.9 (SCF), 44.0 (CCSD), and 48.4 kcal mol$^{-1}$ [CCSD(T)], whereas that for the *cis* isomer is −3.6 (SCF), 31.8 (CCSD), and 38.0 kcal mol$^{-1}$ [CCSD(T)] with the aug-cc-pVQZ basis set. For the three equilibrium structures the increases of the dissociation energies with inclusion of correlation effects are 37.1 (cyclic), 30.5 (*trans*), and 41.6 (*cis*) kcal mol$^{-1}$, respectively. These relatively large increments may be attributed to some multi-reference character

of the BNNO species. These BN ($X\ ^3\Pi$) + NO ($X\ ^2\Sigma^+$) dissociation reactions are thermodynamically disfavored relative to the B ($^2P_u$) + NNO ($\tilde{X}\ ^1\Sigma^+$) pathway discussed above (see Figure 4).

### 3.4.6 Dipole Moments

The dipole moments for the five stationary points are presented in Tables S6 − S10. For the three equilibrium structures the dipole moments are predicted to be 1.90 (cyclic), 2.27 (*trans*), and 1.16 (*cis*) debye at the aug-cc-pVTZ CCSD(T) (CCSD for *cis*) level of theory. The *trans* isomer has the largest dipole moment, with the expected sign $^+$BNNO$^-$.

### 3.4.7 Harmonic Vibrational Frequencies

The harmonic vibrational frequencies for the five stationary points of the BNNO molecule at the aug-cc-pVQZ CCSD(T) level of theory are reported in Table 3 and Tables S6 − S10. The four highest frequencies are predicted to be 1712, 1298, 1013 and 859 cm$^{-1}$ for the cyclic minimum, 1876, 1544, 874, and 646 cm$^{-1}$ for the *trans* isomer, while they are 1641, 1368, 1011, and 679 cm$^{-1}$ for the *cis* isomer.

The corresponding experimentally observed (fundamental) frequencies are 1795.7, 1500.3, 836.5, and 626.9 cm$^{-1}$ for the $^{11}$BNNO isotopologue.[65] Among three isomers four vibrational frequencies of the $^{11}$BNNO isotopomer for the *trans* isomer are most consistent with Wang and Zhou's experimental values. A more detailed comparison of the theoretical fundamental frequencies with Wang and Zhou's experimental observations will be given in subsection I below.

### 3.4.8 Infrared (IR) Intensities

The IR intensities of the six vibrational modes for three equilibrium isomers are presented in Tables S6 − S10. From the IR spectra of Wang and Zhou,[65] the IR intensities ($I_s$) for the four observed modes for the *trans* isomer were concluded to be in the order $I_2$ (NO stretching) > $I_3$ (NN stretching) > $I_1$ (BN stretching) > $I_4$ (in-plane bending). This experimental ordering is well reproduced for the *trans* isomer using the CCSD(T) level of theory (in Table S7), even within the double harmonic approximation.

### 3.4.9 Anharmonic Vibrational Frequencies and Isotopic Shifts

In Table 4, the fundamental vibrational frequencies for the $^{10}B^{14}N^{14}NO$ isotopologue, as well as the respective isotopic shifts of $^{11}B^{14}N^{14}NO$, and $^{10}B^{15}N^{15}NO$ are presented. The anharmonic vibrational frequencies are determined via VPT2 theory using our cc-pCVTZ CCSD(T) quartic force field. For the $^{10}B^{14}N^{14}NO$ *trans* isotopologue the deviations between theoretical harmonic and experimental fundamental frequencies of the four modes are +85, +50, +28, and +11 $cm^{-1}$, respectively. On the other hand the corresponding differences between theoretical anharmonic and experimental fundamental frequencies for the *trans* isomer are +36, +28, −6, and −15 $cm^{-1}$. The improvement in the agreement with inclusion of theoretical anharmonic effects is evident. However, the disagreement between experiment is unusually large for such a reliable level of theory. Of course, the theoretical results are directly comparable only to gas phase experiments, not matrix isolation results.

From the experimental observations, the 1837 $cm^{-1}$ transition exhibits the largest isotopic shift for $^{11}B$ (41 $cm^{-1}$) and $^{15}N$ (28 $cm^{-1}$), since it is primarily a B−N stretching mode. The 1502 $cm^{-1}$ frequency shows a very small $^{11}B$ shift (2 $cm^{-1}$) but quite a large nitrogen isotopic shift (26 $cm^{-1}$), consistent with its assignment as the N−O stretching mode. The 838 $cm^{-1}$ absorption shows almost no change among boron isotopes, but exhibits large nitrogen isotopic shift (23 $cm^{-1}$) and is therefore attributed to the N−N stretching mode.

For the the global minimum cyclic-isomer, the B−N stretching mode exhibits a large B isotopic shift (28 $cm^{-1}$) and N isotopic shift (19 $cm^{-1}$). In the case of the *trans* isomer the N−O stretching mode and N−N stretching mode have almost no shift within B isotopes, but quite large N isotopic shifts (27 $cm^{-1}$ for the N−O stretch and 22 $cm^{-1}$ for the N−N stretch). Our frequency shifts upon isotopic substitution for the *trans* isomer are in good agreement with the experimentally observed values, in contrast to those for the cyclic global minimum; this indicates that the *trans* isomer was observed in the experiment.

### 3.4.10 *Trans* or Cyclic Structure?

Our theoretical investigation clearly shows that the cyclic isomer is the global minimum, but the vibrational frequencies and isotopic shifts thereof provide compelling evidence for the experimental

observation of the *trans* isomer. To gain some insight into the conformational preferences of the reaction, we constructed a two-dimensional energetic contour plot with respect to the boron atom position, constraining the NNO moiety to its isolated ($\tilde{X}\ ^1\Sigma^+$) geometry and enforcing planarity. The cc-pVDZ CASSCF method with a (7, 7) active space was used in order to describe the various bonding schemes encountered on the resulting PES, which is shown in Figure 5. The area in the immediate vicinity of the molecule is repulsive within the constraints imposed, but crucially the region around the N terminus is less repulsive than that around the central nitrogen atom, favoring the formation of *trans* BNNO over cyclic BNNO. This feature may be explained from the NNO molecular orbitals shown in Figure S6. The $7\sigma$ MO of NNO mainly consists of the lone-pair orbital of the terminal N atom. The electropositive B atom, therefore, may be prone to approach the electron-rich terminal N atom along the NNO molecular axis.

Clearly, as the reaction proceeds, the NNO angle must decrease, so an analogous plot was generated (Figure 6) with the NNO geometry chosen as [$r_e$(NO) = 1.30 Å, $r_e$(NN) = 1.20 Å, $\theta_e$ = 123.0°] to represent a compromise between the NNO geometries adopted in the cyclic and *trans* isomers. The relaxation of the NNO unit changes the qualitative nature of the potential, introducing two bound minima. The minimum corresponding to the cyclic structure, although deeper than the *trans* minimum, has a relatively small area, which translates into a relatively low capture cross section for boron atoms leading to cyclic BNNO formation. Although this analysis is quite crude, it offers insight into the basins of attraction on the B + NNO potential energy surface.

## 3.5 Conclusions

*Ab initio* molecular electronic structure theory has been employed in order to investigate the cyclic, *trans*, and *cis* isomers of BNNO and two isomerization reactions connecting them. At our highest level of theory, aug-cc-pVQZ CCSD(T), the *trans* isomer was predicted to be 3.5 kcal mol$^{-1}$ (2.4 kcal mol$^{-1}$ with the ZPVE correction) higher than the cyclic minimum. The barrier height for the uphill isomerization reaction (cyclic → *trans*) is determined to be of 19.7 (18.3) kcal mol$^{-1}$. The *trans* and *cis* isomers are separated by 10.6 (10.4) kcal mol$^{-1}$ with a barrier (*trans* → TS1 → *cis*) of 10.8 (10.4) kcal mol$^{-1}$, which indicates that the *trans* to *cis* isomerization reaction is unlikely

to occur in an argon matrix. Theoretically computed harmonic and anharmonic vibrational frequencies and associated IR intensities are consistent with the experimental observation of *trans* BNNO in an argon matrix. The dissociation energies (with ZPVE corrections) associcated with BNNO ($\tilde{X}\ ^2A'$) $\rightarrow$ B ($^2P_u$) + NNO ($\tilde{X}\ ^1\Sigma^+$) for the cyclic, *trans*, and *cis* isomers were predicted to be 39.7, 37.3, and 27.0 kcal mol$^{-1}$, while the diatomic fragment dissociation energies BNNO ($\tilde{X}\ ^2A'$) $\rightarrow$ BN ($X\ ^3\Pi$) + NO ($X\ ^2\Sigma^+$) for the three isomers were determined to be 50.7, 48.4, and 38.0 kcal mol$^{-1}$, respectively. Therefore, the three equilibrium structures are well below the dissociation limits to [B ($^2P_u$) + NNO ($\tilde{X}\ ^1\Sigma^+$)] and [BN ($X\ ^3\Pi$) + NO ($X\ ^2\Sigma^+$)]. There are no bonding regions with the NNO fragment constrained (linear) to its native geometry; its geometry must relax for B ($^2P_u$) + NNO ($\tilde{X}\ ^1\Sigma^+$) association to proceed. Two distinct bonding regions are found on the relaxed (bent) surface. The first leads to formation of the *trans* isomer, this region being much broader but less deep than that leading to formation of cyclic BNNO. The larger capture cross section due to the broader *trans* well appears to explain the experimental observation of only the higher energy *trans* isomer.

## 3.6 Acknowledgments

The authors would like to thank Dr. Partha P. Bera, Dr. Justin M. Turney, and Dr. Steven E. Wheeler for insightful discussions and technical expertise. This research was supported by the Department of Energy, Basic Energy Sciences, Division of Chemical Sciences, Fundamental Interactions Team, Grant No. DEFG02-97-ER14748. This research used the resources of the National Energy Research Scientific Computing Center (NERSC), supported by the Office of Science of the U.S. Department of Energy under Contract No. DE-AC02-05CH11231 and VMD software developed by the Theoretical and Computational Biophysics Group in the Beckman Institute for Advanced Science and Technology at the University of Illinois at Urbana-Champaign.

Table 3.1: Relative energies (in kcal $mol^{-1}$, ZPVE corrected values are in parentheses) of five stationary points on the potential energy surface for the BNNO molecule at SCF, CCSD, and CCSD(T) levels of theory.

| Level of theory | cyclic | *trans* | *cis* | TS1 | TS2 |
|---|---|---|---|---|---|
| cc-pVTZ SCF | 0.00 (0.00) | -3.76 (-4.61) | 17.94 (16.50) | 19.50 (17.55) | 18.43 (16.64) |
| aug-cc-pVTZ SCF | 0.00 (0.00) | -3.35 (-4.19) | 18.67 (17.22) | 20.22 (18.25) | 18.49 (16.70) |
| cc-pVQZ SCF | 0.00 (0.00) | -3.59 (-4.44) | 18.58 (17.13) | 20.11 (18.14) | 18.51 (16.72) |
| aug-cc-pVQZ SCF | 0.00 (0.00) | -3.48 (-4.34) | 18.76 (17.31) | 20.28 (18.31) | 18.54 (16.75) |
| cc-pVTZ CCSD | 0.00 (0.00) | 1.11 (0.15) | 13.34 (11.50) | 13.80 (12.31) | 19.04 (17.14) |
| aug-cc-pVTZ CCSD | 0.00 (0.00) | 1.52 (0.58) | 14.11 (12.24) | 14.60 (13.10) | 19.56 (17.66) |
| cc-pVQZ CCSD | 0.00 (0.00) | 1.48 (0.52) | 14.64 (12.76) | 15.09 (13.57) | 20.21 (18.29) |
| aug-cc-pVQZ CCSD | 0.00 (0.00) | 1.52 (0.58) | 14.84 (12.96) | 15.30 (13.79) | 20.38 (18.47) |
| cc-pVTZ CCSD(T) | 0.00 (0.00) | 3.22 (1.82) | 12.81 (11.42) | 12.91 (11.54) | 18.49 (17.04) |
| aug-cc-pVTZ CCSD(T) | 0.00 (0.00) | 3.50 (2.33) | 13.44 (12.00) | 13.57 (12.16) | 18.97 (17.53) |
| cc-pVQZ CCSD(T) | 0.00 (0.00) | 3.51 (2.33) | 13.96 (12.61) | 14.09 (12.65) | 19.57 (18.09) |
| aug-cc-pVQZ CCSD(T) | 0.00 (0.00) | 3.50 (2.35) | 14.10 (12.76) | 14.25 (12.82)[a] | 19.74 (18.27) |

[a] ZPVE values computed at the cc-pVQZ CCSD(T) level of theory.

Table 3.2: Dissociation energies (in kcal mol$^{-1}$, ZPVE corrected values in parentheses) of the BNNO ($\tilde{X}\ ^2A'$) $\rightarrow$ B ($^2P_u$) + NNO ($\tilde{X}\ ^1\Sigma^+$) and BNNO ($\tilde{X}\ ^2A'$) $\rightarrow$ BN ($X\ ^3\Pi$) + NO ($X\ ^2\Sigma^+$) channels, at the SCF, CCSD, and CCSD(T) levels of theory with the aug-cc-pVQZ basis set.

| Level of theory | cyclic | *trans* | *cis* |
|---|---|---|---|
| BNNO ($\tilde{X}\ ^2A'$) $\rightarrow$ B ($^2P_u$) + NNO ($\tilde{X}\ ^1\Sigma^+$) | | | |
| aug-cc-pVQZ SCF | 30.50 (28.45) | 33.95 (32.75) | 11.91 (11.32) |
| aug-cc-pVQZ CCSD | 38.27 (36.17) | 36.77 (35.60) | 23.58 (23.35) |
| aug-cc-pVQZ CCSD(T) | 41.27 (39.65) | 37.81 (37.33) | 27.30 (27.02) |
| BNNO ($\tilde{X}\ ^2A'$) $\rightarrow$ BN ($X\ ^3\Pi$) + NO ($X\ ^2\Sigma^+$) | | | |
| aug-cc-pVQZ SCF | 17.58 (13.55) | 21.03 (17.86) | $-1.00$ ($-3.57$) |
| aug-cc-pVQZ CCSD | 48.34 (44.61) | 46.84 (44.04) | 33.65 (31.79) |
| aug-cc-pVQZ CCSD(T) | 54.22 (50.67) | 50.75 (48.35) | 40.25 (38.04) |

Table 3.3: Theoretical predictions of the total energy (in hartree), harmonic vibrational frequencies ($\omega$, in $cm^{-1}$), and zero-point vibrational energy (ZPVE in kcal $mol^{-1}$) for the $^2A'$ cyclic, *trans*, *cis*, TS1, and TS2 $^{11}B^{14}N^{14}NO$ molecule at the aug-cc-pVQZ CCSD(T) level of theory.[a]

| Structure | Total energy | $\omega_1(a')$ | $\omega_2(a')$ | $\omega_3(a')$ | $\omega_4(a')$ | $\omega_5(a')$ | $\omega_6(a'')$ | ZPVE |
|---|---|---|---|---|---|---|---|---|
| cyclic | -209.134170 | 1712 | 1298 | 1013 | 859 | 517 | 511 | 8.45 |
| *trans* | -209.128591 | 1876 | 1544 | 874 | 646 | 149 | 137 | 7.30 |
| *cis* | -209.111697 | 1641 | 1368 | 1011 | 679 | 189 | 85 | 7.11 |
| TS1 | -209.111462 | (1675) | (1420) | (990) | (651) | (204) | ($100i$) | (7.06) |
| TS2 | -209.102719 | 1866 | 1234 | 1005 | 431 | 348 | $691i$ | 6.98 |

[a] For TS1, the total energy is the single point energy with cc-pVQZ CCSD(T) optimized geometry, and harmonic vibrational frequencies and ZPVE are computed at the cc-pVQZ CCSD(T) level.

Table 3.4: Fundamental vibrational frequencies (in $cm^{-1}$) for the BNNO molecule and the corresponding shifts ($\Delta$) upon isotopic substitution at the cc-pCVTZ CCSD(T) level of theory. The experimental results are shown for comparison purposes.

| Mode (Sym.) | $\nu_{^{10}B^{14}N^{14}NO}$ | $\Delta(\nu_{^{11}B^{14}N^{14}NO})$ | $\Delta(\nu_{^{10}B^{15}N^{15}NO})$ |
|---|---|---|---|
| Experiment[a] | | | |
| B-N stretch | 1837 | 41 | 28 |
| N-O stretch | 1502 | 2 | 26 |
| N-N stretch | 838 | 1 | 23 |
| Bending | 634 | 7 | 9 |
| *trans* BNNO | | | |
| B-N stretch | 1873 | 41 | 30 |
| N-O stretch | 1530 | 2 | 27 |
| N-N stretch | 832 | 1 | 22 |
| Bending | 619 | 8 | 10 |
| cyclic BNNO | | | |
| B-N stretch | 1305 | 28 | 19 |
| N-O stretch | 1684 | 15 | 34 |
| N-N stretch | 982 | 18 | 16 |
| Bending | 830 | 6 | 16 |

[a] Ref.

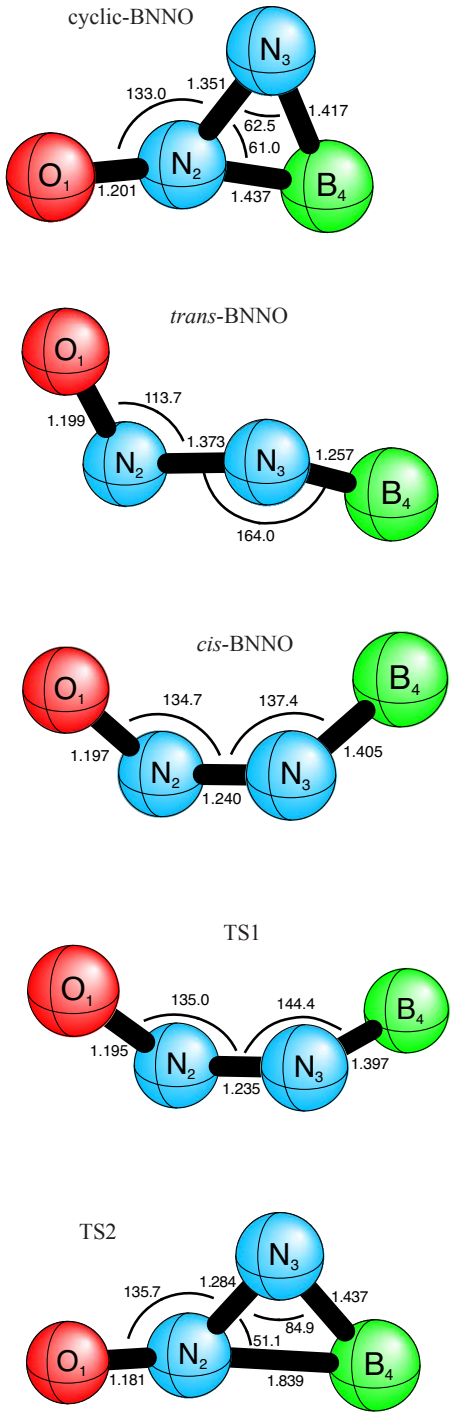


Figure 3.1: The optimized geometries (Å and degrees) of the five stationary point structures of BNNO at the aug-cc-pVQZ CCSD(T) level of theory. $\tau$(BNNO) for the *cis* BNNO isomer is 38.8° and $\tau$ for TS1 is 80.4°. The TS1 geometrical parameters are at the cc-pVQZ CCSD(T) level of theory.

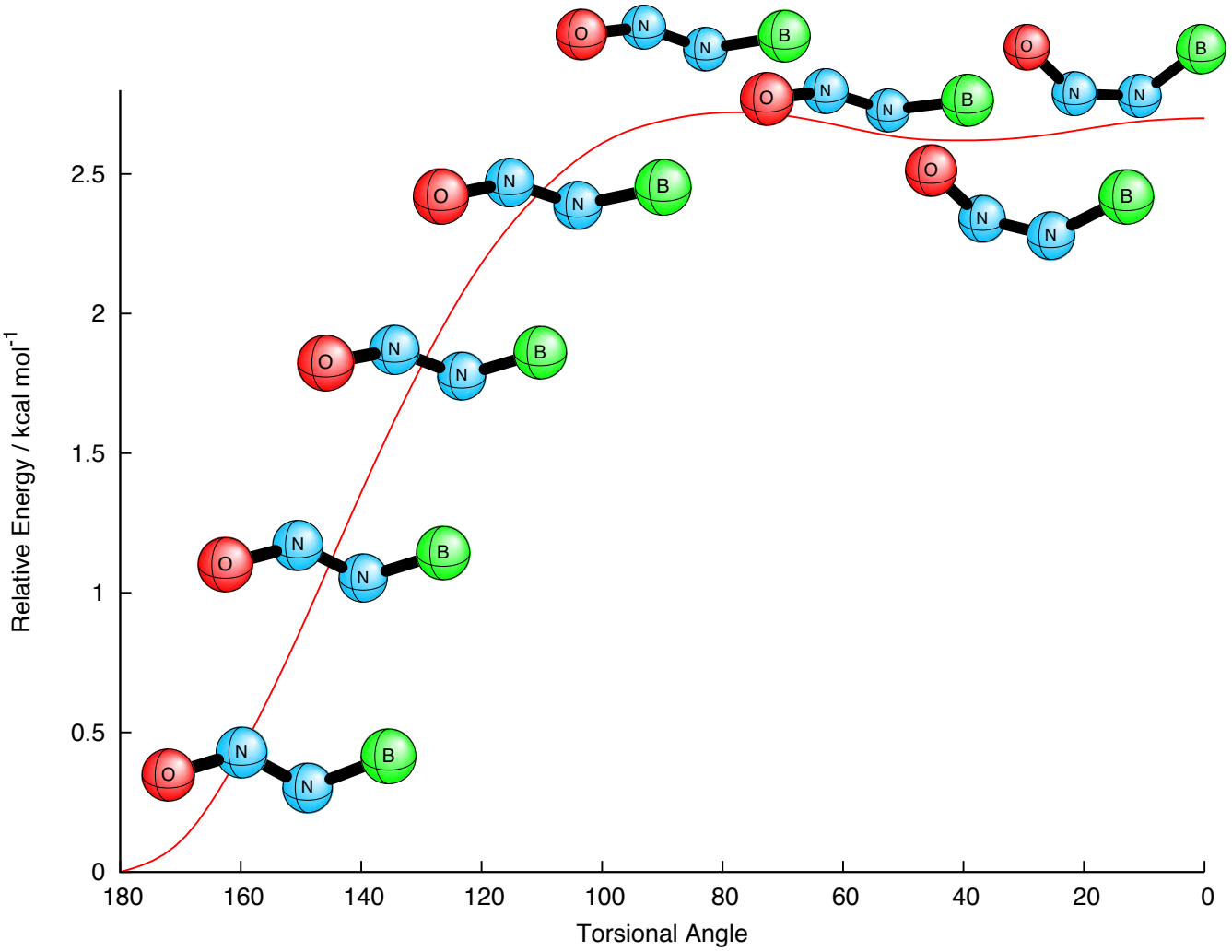


Figure 3.2: Relaxed potential energy curve for BNNO, plotted as a function of the torsional angle $\tau$(BNNO), at the cc-pVTZ CCSD(T) level of theory.

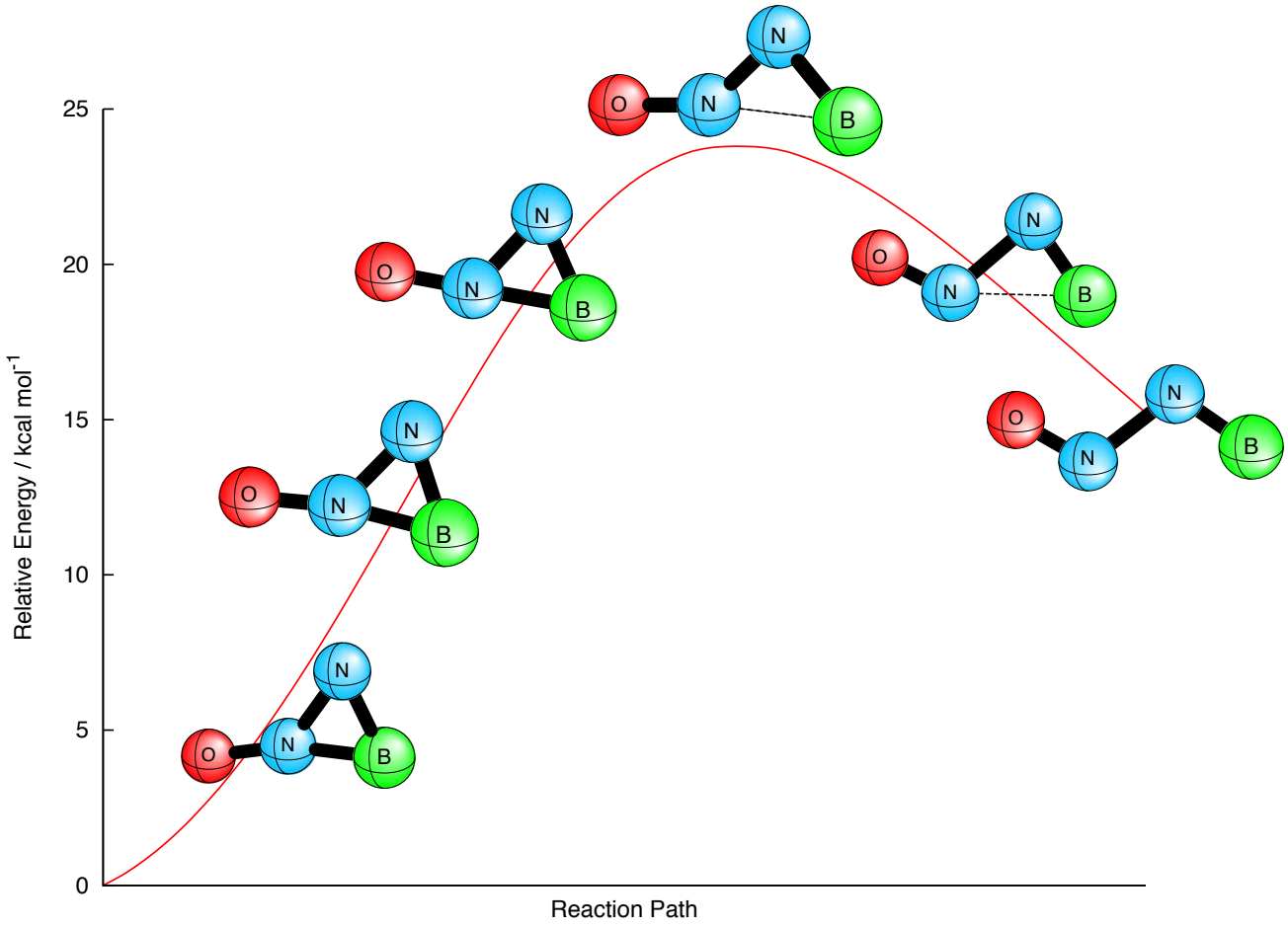


Figure 3.3: Intrinsic reaction coordinate (IRC) for the cyclic−*trans* isomerization reaction of BNNO at the cc-pVDZ MP2 level of theory.

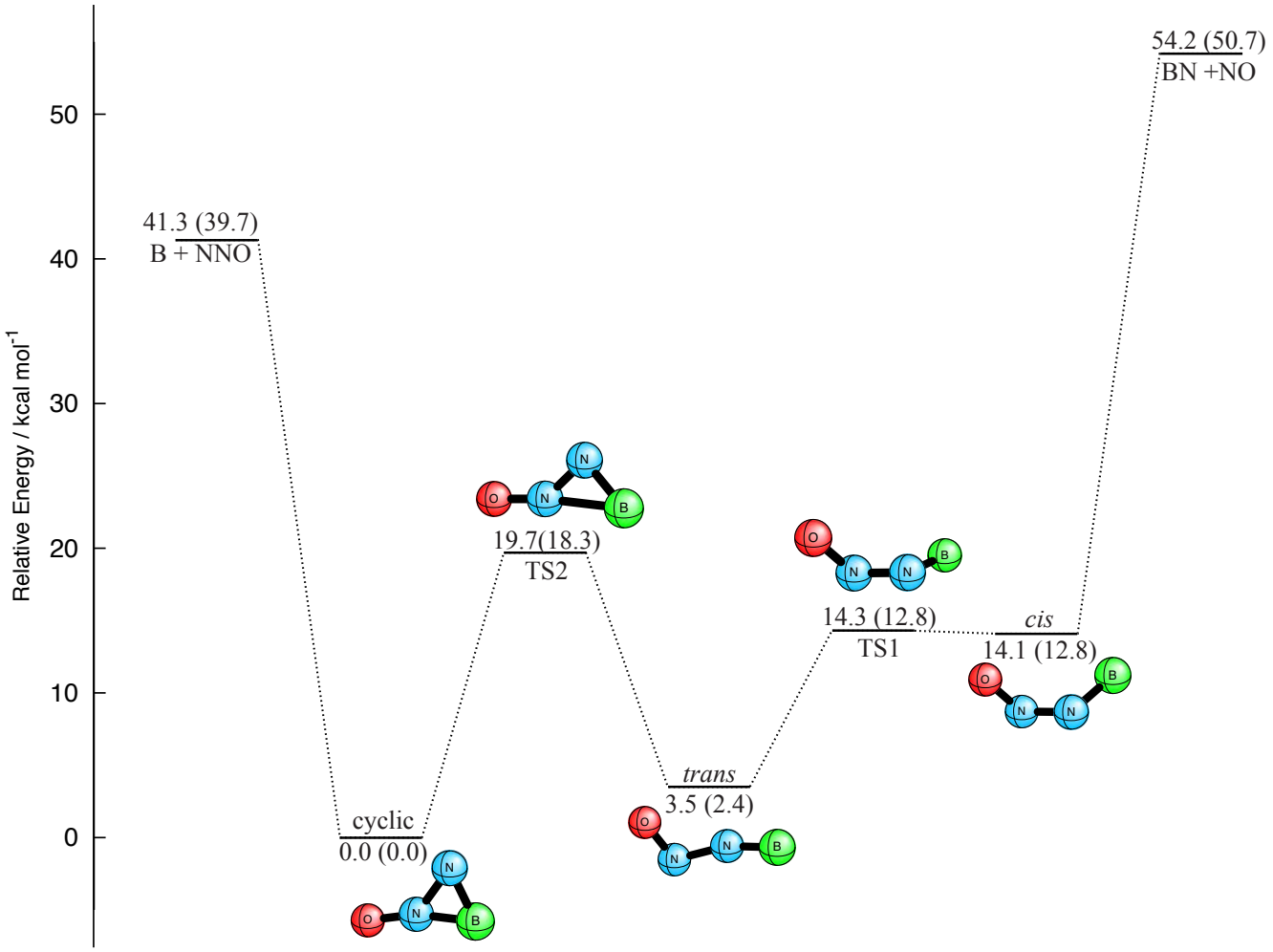


Figure 3.4: Stationary points on the BNNO potential energy surface at the aug-cc-pVQZ CCSD(T) level of theory. Relative energies are in kcal $mol^{-1}$(ZPVE corrected values in parentheses).

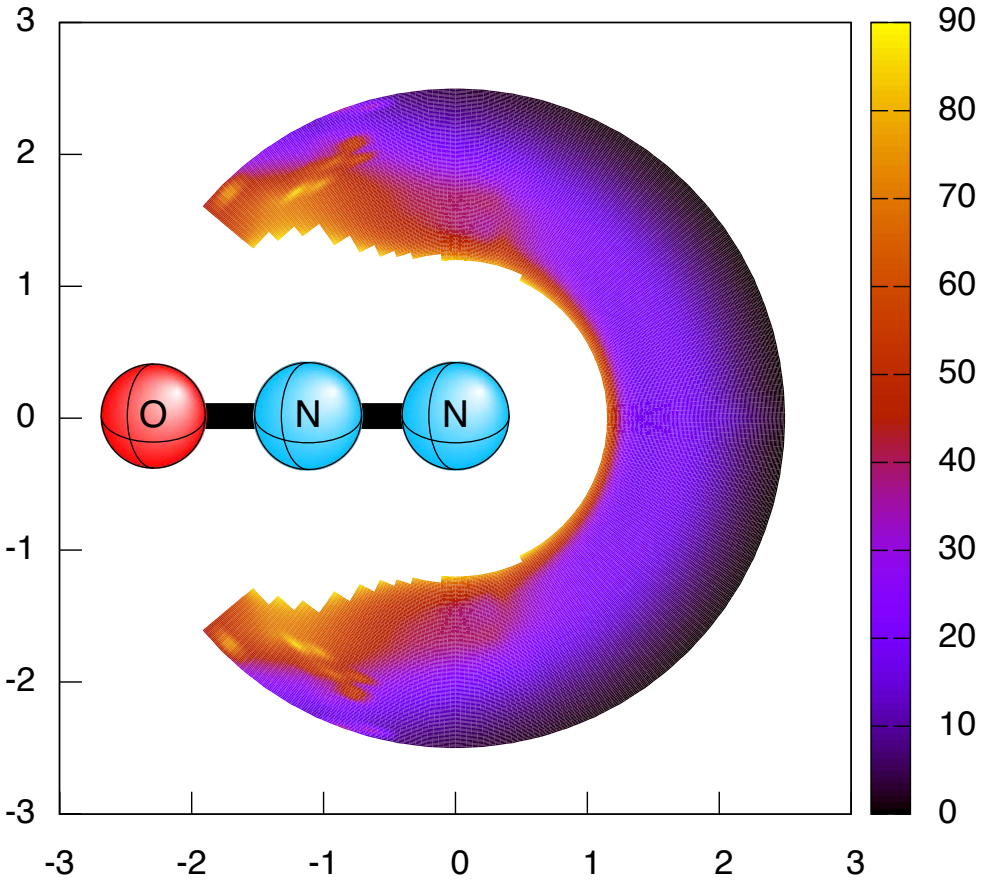


Figure 3.5: The potential energy surface (in kcal mol$^{-1}$ and Å units) describing the B ($^2$P$_u$) + NNO ($\tilde{X}$ $^1\Sigma^+$) (linear) reaction at the cc-pVDZ CASSCF (7, 7) level of theory. See text for details.

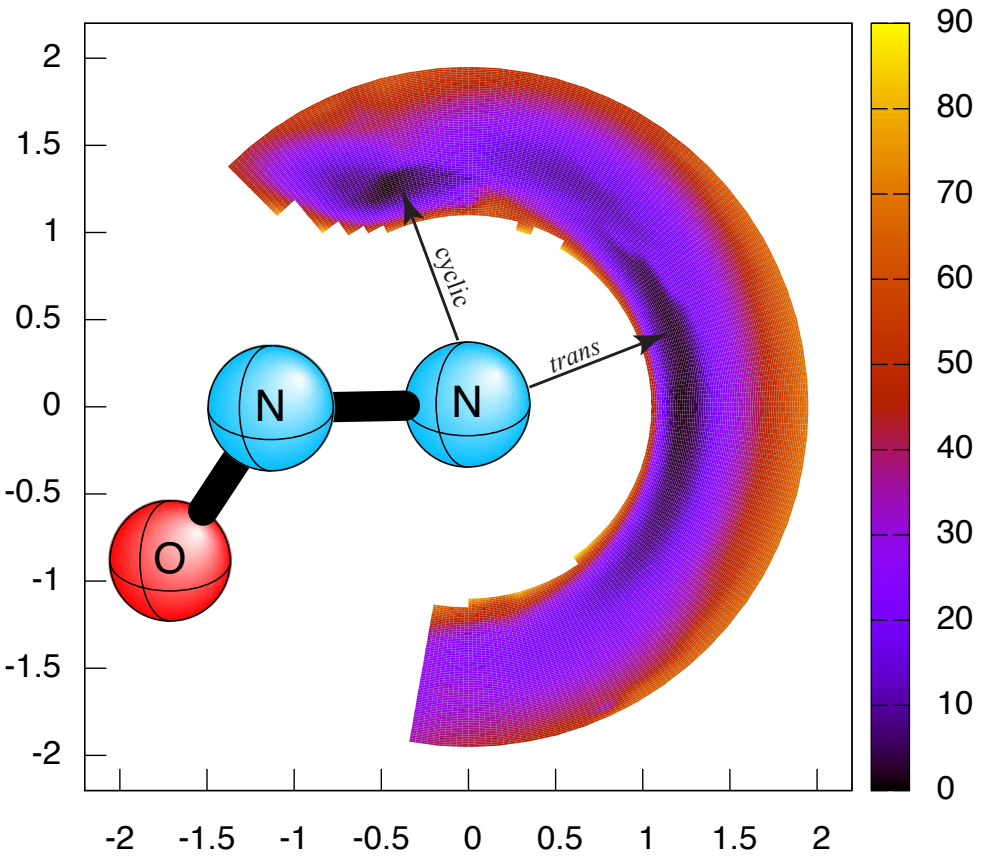


Figure 3.6: The potential energy surface (in kcal mol$^{-1}$ and Å units) describing the B ($^2$P$_u$) + NNO ($\tilde{X}\ ^1A'$) (bent) reaction at the cc-pVDZ CASSCF (7, 7) level of theory. Wells corresponding to cyclic and *trans* BNNO minima are labelled. See text for details.

## Bibliography


[1] U. Nohl and G. Olbrich, *Gmelin Handbook of Inorganic Chemistry* (Springler: Berlin, 1988).

[2] R. T. Paine and C. K. Narula, Chem. Rev. **90**, 73 (1990).

[3] Z. Wang, S. Li, L. Zhang, Z. Sheng, and S. Yu, Propel. Explos. Pyrotech. **29**, 160 (2004).

[4] K. Kuo and R. Pein, *Combustion of Boron-Based Solid Propellants and Solid Fuels* (CRC Press, Boca Raton, 1993).

[5] D. M. Chen, S. P. Luh, T. K. Liu, G. K. Wu, and H. C. Perng, Combustion of Boron-Based Solid Propellants and Solid Fuels p. 375 (1993).

[6] W. Eckl, N. Eisenreich, K. Menke, T. Rohe, and V. Weiser, in *the 26th International Annual Conference of ICT* (1995), p. 70.

[7] D. Ritter and J. C. Weisshaar, J. Phys. Chem. **94**, 4907 (1990).

[8] J. M. C. Plane and R. J. Rollason, J. Chem. Soc., Faraday Trans. **92**, 4371 (1996).

[9] D. E. Clemmer, K. Honma, and I. Koyano, J. Phys. Chem. **97**, 11480 (1993).

[10] R. Matsui, K. Senba, and K. Honma, J. Phys. Chem. **101**, 179 (1997).

[11] M. L. Campbell and R. E. McClean, J. Phys. Chem. **97**, 7942 (1993).

[12] M. L. Campbell, J. Chem. Phys. **104**, 7515 (1996).

[13] M. L. Campbell, E. J. Kölsch, and K. L. Hooper, J. Phys. Chem. **104**, 11147 (2000).

[14] M. L. Campbell, J. Phys. Chem. **107**, 3048 (2003).

[15] P. B. Armentrout, L. F. Halle, and J. L. Beauchamp, J. Chem. Phys. **76**, 2449 (1982).

[16] P. M. Futerko and A. Fontijn, J. Chem. Phys. **95**, 8065 (1991).

[17] A. Delabie, C. Vinckier, M. Flock, and K. Pierloot, J. Phys. Chem. **105**, 5479 (2001).

[18] A. Stirling, J. Am. Chem. Soc. **124**, 4058 (2002).

[19] O. Tishchenko, C. Vinckier, and M. T. Nguyen, J. Phys. Chem. **108**, 1268 (2004).

[20] O. Tishchenko, C. Vinckier, A. Ceulemans, and M. T. Nguyen, J. Phys. Chem. **109**, 6099 (2005).

[21] V. V. Lavrov, V. Blagojevic, G. K. Koyanagi, G. Orlova, and D. K. Bohme, J. Phys. Chem. **108**, 5610 (2004).

[22] V. Blagojevic, G. Orlova, and D. K. Bohme, J. Am. Chem. Soc. **127**, 3545 (2005).

[23] M. D. C. Michelini, N. Russo, M. E. Alikhani, and B. Silvi, J. Comput. Chem. **26**, 1284 (2005).

[24] S. F. Palopoli and T. B. Brill, Combust. Flame **87**, 45 (1991).

[25] T. B. Brill, P. J. Brush, and D. G. Patil, Combust. Flame **94**, 70 (1993).

[26] G. Wang and M. Zhou, Chem. Phys. Lett. **342**, 90 (2007).

[27] T. H. Dunning, J. Chem. Phys. **90**, 1007 (1989).

[28] D. E. Woon and T. H. Dunning, J. Chem. Phys. **98**, 1358 (1993).

[29] P. J. Knowles and H.-J. Werner, Chem. Phys. Lett. **115**, 259 (1985).

[30] H.-J. Werner and P. J. Knowles, J. Chem. Phys. **82**, 5053 (1985).

[31] C. Hampel, K. A. Peterson, and H.-J. Werner, Chem. Phys. Lett. **190**, 1 (1992).

[32] J. D. Watts, J. Gauss, and R. J. Bartlett, Chem. Phys. Lett. **200**, 1 (1992).

[33] K. Raghavachari, G. W. Trucks, J. A. Pople, and M. Head-Gordon, Chem. Phys. Lett. **157**, 479 (1989).

[34] J. D. Watts, J. Gauss, and R. J. Bartlett, J. Chem. Phys. **98**, 8718 (1993).

[35] J. F. Stanton, Chem. Phys. Lett. **281**, 130 (1997).

[36] H.-J. Werner, P. J. Knowles, R. Lindh, F. R. Manby, M. Schütz, *et al.*, Molpro, version 2006.1, a package of ab initio programs.

[37] J. F. Stanton, J. Gauss, J. D. Watts, W. J. Lauderdale, and R. J. Bartlett, Int. J. Quantum Chem. **44(S26)**, 879 (1992).

[38] Stanton, J. F.; Gauss, J.; Watts, J. D.; Szalay, P. G.; Bartlett, R. J.; with contributions from Auer, A. A.; Bernholdt, D. E.; Christiansen, O.; Harding, M. E.; Heckert, M.; Heun, O.; Huber, C.; Jonsson, D.; Jusélius, J.; Lauderdale, W. J.; Metzroth, T.; Michauk, C.; O'Neill, D. P.; Price, D. R.; Ruud, K.; Schiffmann, F.; Tajti, A.; Varner, M. E.; Vázquez, J.; and the integral packages: MOLECULE (Almlöf, J.; Taylor, P. R.), PROPS (Taylor, P. R.), and ABACUS (Helgaker, T.; Jensen, H. J. Aa.; Jørgensen, P.; Olsen, J.;). Current version see http://www.aces2.de.

[39] T. D. Crawford, C. D. Sherrill, E. F. Valeev, J. T. Fermann, R. A. King, M. L. Leininger, S. T. Brown, C. L. Janssen, E. T. Seidl, J. P. Kenny, and W. D. Allen, J. Comp. Chem. **28**, 1610 (2007).

[40] T. J. Lee and P. R. Taylor, Int. J. Quantum. Chem. Symp. **23**, 199 (1989).

[41] A. L. L. East, C. S. Johnson, and W. D. Allen, J. Chem. Phys. **98**, 1299 (1993).

[42] H. H. Nielsen, Rev. Mod. Phys. **23**, 90 (1951).

[43] I. M. Mills, in *Molecular Spectroscopy: Modern Research*, edited by K. N. Rao and C. W. Mathews (Academic Press, New York, 1972), p. 115.

[44] J. K. G. Watson, in *Vibrational Spectra and Structure*, vol. 6, edited by J. R. Durig (Elsevier, Amsterdam, 1972), p. 1.

[45] D. Papoušek and M. R. Aliev, *Molecular Vibrational-Rotation Spectra* (Elsevier, Amsterdam, 1982).

[46] D. A. Clabo, W. D. Allen, R. B. Remington, Y. Yamaguchi, and H. F. Schaefer, Chem. Phys. **123**, 187 (1988).

[47] W. D. Allen, Y. Yamaguchi, A. G. Császár, D. A. Clabo, R. B. Remington, and H. F. Schaefer, Chem. Phys. **145**, 427 (1990).

[48] K. Aarset, A. G. Császár, E. L. Sibert, W. D. Allen, H. F. Schaefer, W. Klopper, and J. Noga, J. Chem. Phys. **112**, 4053 (2000).

[49] GRENDEL is a program written by Jeremiah J. Wilke to perform general numerical differentiations to high orders of electronic structure data.

[50] INTDER2005 is a general program developed by Wesley D. Allen and co-workers which performs various vibrational analyses and higher-order nonlinear transformations among force field representations.

[51] W. D. Allen and A. G. Császár, J. Chem. Phys. **98**, 2983 (1993).

[52] W. D. Allen, A. G. Császár, V. Szalay, and I. M. Mills, Mol. Phys. **89**, 1213 (1996).

[53] K. Sarka and J. Demaison, in *Computational Molecular Spectroscopy*, edited by P. Jensen and P. R. Bunker (Wiley, Chichester, 2000), p. 255.

[54] A. C. Simmonett, F. A. Evangelista, W. D. Allen, and H. F. Schaefer, J. Chem. Phys. **127**, 014306 (2007).

[55] ANHARM is a FORTRAN program written for VPT2 analysis by Y. Yamaguchi and H. F. Schaefer, Center for Computational Chemistry, University of Georgia, Athens, GA, 30602, USA.

[56] W. Humphrey, A. Dalke, and K. Schulten, J. Mol. Graphics **14**, 33 (1996).

[57] R. M. Richard and D. W. Ball, J. Mol. Struct. **806**, 113 (2007).

[58] A. Karton and J. M. L. Martin, J. Chem. Phys. **125**, 144313 (2006).

[59] F. Wang and R. D. Harcourt, J. Phys. Chem. A **104**, 1304 (2000).

[60] B. A. MacKay and M. D. Fryzuk, Chem. Rev. **104**, 385 (2004).

[61] H. F. Schaefer, Chem. Britain **11**, 227 (1975).

[62] K. Fukui, Acc. Chem. Res. **14**, 363 (1981).

[63] M. W. Schmidt, M. S. Gordon, and M. Dupuis, J. Am. Chem. Soc. **107**, 2585 (1985).

[64] B. C. Garrett, M. J. Redmon, R. Steckler, D. G. Truhlar, K. K. Baldridge, D. Bartol, M. W. Schmidt, and M. S. Gordon, J. Phys. Chem. **92**, 1476 (1988).

[65] G. Wang, X. Jin, M. Chen, and M. Zhou, Chem. Phys. Lett. **420**, 130 (2006).

# CHAPTER 4

## HYDROXYL RADICAL REACTIONS WITH ADENINE: REACTANT COMPLEXES, TRANSITION STATES, AND PRODUCT COMPLEXES[†]

[†]This is the pre-peer reviewed version of the following article: Qianyi Cheng, Jiande Gu, Katherine R. Compaan, and Henry F. Schaefer, III, *Chem.-Eur. J.*, 2010, **16**, 11848-11858.

## 4.1 Abstract

In order to address problems such as aging, cell death, and cancer, it is important to understand the mechanisms behind reactions causing DNA damage. One specific reaction implicated in DNA oxidative damage is hydroxyl free radical attack on adenine and other nucleic acid bases. The adenine reaction has been studied experimentally, but there are few theoretical results. In the present study, adenine dehydrogenation at various sites, and the potential energy surfaces for these reactions, are investigated theoretically. Four reactant complexes $[A\cdots OH]\cdot$ have been found, with binding energies relative to A + OH· of 32.8, 11.4, 10.7, and 10.1 kcal mol$^{-1}$. These four reactant complexes lead to six transition states, which in turn lie +4.3, −5.4, (−3.7 and +0.8), and (−2.3 and +0.8) kcal mol$^{-1}$ below A + OH·, respectively. Thus the lowest lying $[A\cdots OH]\cdot$ complex faces the highest local barrier to formation of the product $(A{-}H)\cdot + H_2O$. Between the transition states and the products lie six product complexes. Adopting the same order as the reactant complexes, the product complexes $[(A{-}H)\cdots H_2O]\cdot$ lie, respectively, at −10.9, −22.4, (−24.2 and −18.7), and (−20.5 and −17.5) kcal mol$^{-1}$, again relative to separated A + OH·. All six $A + OH\cdot \rightarrow (A{-}H)\cdot + H_2O$ pathways are exothermic, by −0.3, −14.7, (−17.4 and −7.8), and (−13.7 and −7.8) kcal mol$^{-1}$, respectively. The transition state for dehydrogenation at $N_6$ lies at the lowest energy (−5.4 kcal mol$^{-1}$ relative to A + OH·), and thus reaction is likely to occur at this site. This theoretical prediction dovetails with the observed high reactivity of OH radicals with the $NH_2$ group of aromatic amines. However, the high barrier (37.1 kcal mol$^{-1}$) for reaction at the $C_8$ site makes $C_8$ dehydrogenation unlikely. The latter result is consistent with experimental observation of the imidazole ring opening upon OH radical addition to $C_8$. In addition, TD-DFT computed electronic transitions of the $N_6$ product around 420 nm confirm that this is the most likely site for hydrogen abstraction by hydroxyl radical.

## 4.2 Introduction

Cellular DNA contains the complex hereditary information of living organisms. Organisms must maintain the integrity of their DNA in order to remain healthy and propagate. Both normal metabolic activities, and environmental effects can damage DNA.[1–28] When damage accumulates to the extent that it can no longer be repaired, three major problems may occur. These are senescence, programmed cell death, and carcinogenesis, and are manifested by aging, neurological syndromes, and cancer. Thus, the identification and repair of DNA damage is an important factor in improving human health and longevity. A tremendous amount of research has focused on the causes of DNA damage, both exogenously and endogenously. Oxidative damage of cellular DNA by free radicals may be a significant factor in human carcinogenesis.[29–33] There are several reactive oxygen species commonly present in biological systems. Of these, hydroxyl free radical (·OH) appears to be the most damaging.[30,34,35] Normally, hydroxyl radical is present at low concentrations, due to the metabolism of oxygen. Higher concentrations are caused by respiratory bursts, or acute exposure to oxidizing agents such as ionizing radiation[36] or UVA solar light.[37] Solar radiation is strongly implicated in the induction of human skin cancers, including squamous cell and basocellular carcinoma, along with malignant melanoma.[37]

Approximately half of the damage caused by OH radicals occurs on nucleobases. Nucleobases are the structural units which carry genetic information in DNA and RNA. The five principal nucleobases are guanine (G), cytosine (C), adenine (A), thymine (T), and uracil (U). Thymine is only present in DNA, while only RNA contains uracil. Of the four DNA nucleobases, guanine is the most likely to be attacked by OH radicals. The probability that guanine will suffer an initial ·OH attack is 36%, while adenine, thymine, and cytosine have initial attack probabilities of 24%, 22%, and 18%, respectively.[38] Because of this, the one-electron oxidation of guanine is of great interest, particularly oxidation by OH radical. The gas-phase dehydrogenation reaction of guanine with OH radical was studied by Colvin and coworkers[19] using Car-Parinello molecular dynamics in 2002. $N_{11}$ is predicted to be the most favorable site for dehydrogenation. Guanine can under go ·OH addition at its $C_4$ or $C_8$ positions; however, this is less favorable than $N_{11}$ dehydrogenation. Of the two addition products, the $C_8$-hydroxylated radical is more stable. Compared to the $N_{11}$

dehydrogenation product, the $N_9$ dehydrogenated product lies 1.9 kcal $mol^{-1}$ higher in energy, and the $N_1$ dehydrogenated product is 3.4 kcal $mol^{-1}$ higher. Dehydrogenation at $C_8$ is strongly disfavored, being 26.9 kcal $mol^{-1}$ higher in energy at the B3LYP/6-31++G(3df,3pd) level. The free energy dehydrogenation reaction barrier is predicted lowest for $N_9$ (0.15 kcal $mol^{-1}$), followed by $N_{11}$ (0.86 kcal $mol^{-1}$) and $C_8$ (9.64 kcal $mol^{-1}$). Because of the low barriers for $N_9$ and $N_{11}$, these reactions may occur spontaneously, even at low temperatures. For the $C_8$ position, dehydrogenation occurs at a reasonable rate at room temperature but would be slow at low temperatures.

In more recent work, Chatgilialoglu and coworkers experimentally studied the reaction of the OH radical with guanosine and 8-bromoguanosine using absorption spectroscopy, in an effort to reevaluate the ambient reactivity of guanine moieties toward ·OH radicals.[39] A broad band at 616 nm implies that the major reaction between guanine and the OH radical is hydrogen abstraction from $NH_2$, followed by tautomerization. Hydroxyl radical addition at the $C_4$ position is less important.

Adenine has the second highest initial ·OH attack probability, so it is also of great interest. Hydroxyl radical typically adds to the double bonds of adenine to yield $C_4$, $C_5$, and $C_8$ radical adducts.[40,41,44–46] Of these three products, the A4OH radical constitutes more than 81% of the hydroxylated radicals generated.[41] The A4OH radical adduct is a weak oxidant. However, like guanine, A4OH can lose a water molecule and become a strong oxidant, the (A−H)· radical. The second most abundant radical product is A8OH, which comprises about 18% of the radicals generated.[41] This radical is actually predicted to form the products 8-hydroxyadenine, 5-formamido-4,6-diaminopyrimidine ($FAP_Y$), ($FAP_Y$G), and 5′-cyclo-2′-deoxy-adenosine.[40] Vieira and Steenken studied the transient species formed during the aqueous reaction of OH radical with adenine. Using a combination of conductance, optical detection, and absorption spectroscopy, they monitored the reaction of the OH radical with fully alkylated adenines, such as $N^6$, $N^6$-dimethyladenosine, and $N^6$, $N^6$, 9-trimethyladenine.[44] Either dehydroxylation or dehydration can occur when OH radicals add at $C_4$ or $C_5$ sites. This is evidenced by a decrease in optical density (OD) at 400 nm. If the OH radicals add at the $C_8$ site, ring-opening occurs and the OD at 330 nm increases. A 2008 study by Naumov and Sonntag[46] confirmed the earlier indications that OH radical forms an adduct with adenine at the $C_4$ position. The adduct undergoes proton or hydrogen transfer, followed by dehy-

dration, to form an $N_6$-dehydrogenated radical. On the other hand, if the C8 adduct is formed, ring-opening occurs. The product is 5-formamido-4,6-diaminopyrimidine ($FAP_Y$). In concert with X-ray radiation, OH radical can attack the $C_2$, $C_8$, $N_9$, $N_{61}$, or $N_{62}$ hydrogens directly,[4,40,41,47–50] producing neutral radicals or ionized species.[46,51]

In the realm of quantum chemistry, a plethora of highly interesting large systems have not yet been explored, including many DNA subunits. For sufficiently small species, wave function methods yield excellent results, accurate to within 1 kcal $mol^{-1}$. This chemical accuracy is only possible for systems with a limited number of chemically active electrons. On the other hand, Density Functional Theory (DFT) holds promise for very large systems. It is more accurate than Hartree-Fock theory and most semi-empirical methods, but is efficient enough to be applied to large molecules. Because of this, DFT is an effective method for quantum chemistry applications.

Neutral adenine[56] and five dehydrogenated adenine radical derivatives[57] have been considered in previous theoretical studies. However, the mechanisms of crucial dehydrogenation reactions have not been fully unravelled. Specifically, the energetics and associated transition states for dehydrogenation of adenine by OH radical ($A + \cdot OH \rightarrow \ \cdot A{-}H + H_2O$) are not known. The present study elucidates the potential energy surfaces for dehydrogenation of adenine by ·OH radical. The corresponding reaction pathways and energetics are provided, and should shed light on related biochemical experiments.

## 4.3 Theoretical methods

The generalized gradient approximation exchange-correlation B3LYP functional was employed in this work. This method has predicted reasonable results for DNA bases, base pairs, and anions[58–61] in previous research. This functional is a combination of Becke's 3-parameter HF/DFT hybrid exchange functional (B3)[62] with the dynamical correlation functional of Lee, Yang, and Parr (LYP)[63].

The B3LYP method is adopted along with double-$\zeta$ quality basis sets with polarization and diffuse functions (denoted as DZP++). The DZP++ basis sets are created by augmenting the Huzinaga−Dunning set of contracted double-$\zeta$ Gaussian functions with one set of $p$-type polarization functions for each H atom and one set on five $d$-type polarization functions for each first-row

atom. To complete the DZP++ basis, one even-tempered $s$ diffuse function was added to each H atom, while even-tempered $s$ and $p$ diffuse functions were centered on every heavy atom. The even-tempered orbital exponents were determined according to the prescription of Lee:[64]

$$\alpha_{\text{diffuse}} = \frac{1}{2}\left(\frac{\alpha_1}{\alpha_2} + \frac{\alpha_2}{\alpha_3}\right)\alpha_1 \tag{4.1}$$

where $\alpha_1$, $\alpha_2$, and $\alpha_3$ are the three smallest Gaussian orbital exponents of the $s$- or $p$-type primitive functions for a given atom ($\alpha_1 < \alpha_2 < \alpha_3$). The final DZP++ set contains six functions per H atom ($5s1p/3s1p$) and nineteen functions per C, N, or O atom ($10s6p1d/5s3p1d$). There are 220 contracted functions for the adenine molecule, 245 functions for adenine-OH complexes, and 214 functions for dehydrogenated adenine molecules . This combination of functionals and basis sets has the tactical advantage that it has previously been used in comprehensive benchmark studies[65] of a wide range of electron affinities.

The binding energies for reactant complexes $(\mathrm{A}\cdots\mathrm{OH})\cdot$ (BE1) and for product complexes $[(\mathrm{A}{-}\mathrm{H})\cdots\mathrm{H_2O}]\cdot$ (BE2) were evaluated according to the following definitions:

$$\mathrm{BE1} = E(\mathrm{A}) + E(\mathrm{OH}\cdot) - E[(\mathrm{A}\cdots\mathrm{OH})\cdot] \tag{4.2}$$

$$\mathrm{BE2} = E(\mathrm{A}) + E(\mathrm{OH}\cdot) - E[\cdot(\mathrm{A}-\mathrm{H})\cdots\mathrm{H_2O}] \tag{4.3}$$

The dissociation energy for reactant complexes $(\mathrm{A}\cdots\mathrm{OH})\cdot$ (DE1) and for product complexes $[(\mathrm{A}{-}\mathrm{H})\cdots\mathrm{H_2O}]\cdot$ (DE2) were evaluated according to the following definitions:

$$\mathrm{DE1} = E[(\mathrm{A}-\mathrm{H})\cdot] + E(\mathrm{H_2O}) - E[(\mathrm{A}\cdots\mathrm{OH})\cdot] \tag{4.4}$$

$$\mathrm{DE2} = E[(\mathrm{A}-\mathrm{H})\cdot] + E(\mathrm{H_2O}) - E[\cdot(\mathrm{A}-\mathrm{H})\cdots\mathrm{H_2O}] \tag{4.5}$$

Computations of optimized geometries, harmonic vibrational frequencies, natural populations,[66–68] and intrinsic reaction coordinates (IRC)[69–72] were performed with the QChem package,[73] which was also used for time-dependent DFT (TD-DFT) treatment of excited electronic states.

## 4.4 Results and Discussion

The structure and numbering scheme for adenine are shown in Figure1. The optimized geometries of neutral adenine molecule, hydroxyl radical, and neutral water molecule are displayed in Figure 2. The optimized geometries of dehydrogenated adenine radicals in the isolated forms are shown in Figure 3. The stability sequence of these radicals is $A-H_9 > A-H_{62} > A-H_{61} > A-H_2 > A-H_8$. Micro-hydration with one water molecule in the dehydrogenation reactions does not change this stability order. The relative energies are summarized in Table 1. The $N_9$-dehydrogenated adenine is the most stable radical, followed by the two $N_6$-dehydrogenated products. Dehydrogenation reactions at nitrogen sites are all exothermic, with enthalpy changes $-0.30$ kcal mol$^{-1}$ for $N_9$, $-0.54$ for $N_{61}$, and $-0.53$ kcal mol$^{-1}$ for $N_{62}$. Carbon site dehydrogenated adenine radicals are much higher in energy [9.52 (9.82) kcal mol$^{-1}$ for $C_2$ site, 17.06 (17.46) kcal mol$^{-1}$ for $C_8$ site] than the $N_9$-radical. In addition, at the carbon site, these dehydrogenation reactions are endothermic; the enthalpy changes are both 0.24 kcal mol$^{-1}$. Nevertheless, the changes in the Gibbs energy for all six dehydrogenation reactions are negative ($-1.34$, $-0.96$, $-1.30$, $-1.15$ and $-1.14$ kcal mol$^{-1}$ for $C_2$, $C_8$, $N_9$, and two $N_6$ sites, respectively) at room temperature. Thus, these reactions are thermodynamically favored.

A natural population analysis (NPA) for neutral adenine is presented in Figure 4. Adenine has five hydrogen atoms. Three of these H atoms are attached to $C_2$, $C_8$, and $N_9$, while two bond to $N_6$. From Figure 4, it is clear that hydrogens bound to nitrogen atoms ($N_6$ and $N_9$) are more positively charged. The positive charge on the five hydrogen atoms is in this order: $H_9 > H_{62} > H_{61} > H_8 > H_2$. Thus, all hydrogen atoms are vulnerable to OH radical attack. In addition, all the carbon atoms are positively charged in A. They may be attacked by OH radical. Since we are interested in dehydrogenation reactions, all hydrogen atoms, and carbon atoms directly attached to hydrogens ($C_2$ and $C_8$), will be considered as OH radical attack sites.

Six different reaction pathways are found for [A+OH$\cdot$ $\rightarrow$ reactant complexes $\rightarrow$ **TS** $\rightarrow$ product complexes $\rightarrow$ (A$-$H)$\cdot$+$H_2O$]. Ten intermediate adenine$-$OH complexes and six transition states for OH radical reacting with adenine are presented in Figure 5 and 6. The numbering schemes correspond to increasing energy, relative to separated adenine and OH radical. All energies are in

kcal mol$^{-1}$, with ZPVE corrected values in parentheses. The energy profiles along the six pathways are displayed in Figure 7. For each pathway, optimized geometries of adenine-OH reactant complexes, transition states, and product complexes are shown in Figures 8−13. The corresponding relative energies are shown in Figures 8−13 and in Table 2.

### 4.4.1 $N_9$ Dehydrogenation

In the vicinity of the most positively charged hydrogen atom ($H_9$), the OH radical attaches to adenine through two hydrogen bonds (see Figure 8). This forms the reactant complex **9**, in which the hydrogen bond lengths of $O\cdots H_9$ and $N_3\cdots H$ are 2.290 and 1.837 Å, respectively. As the reaction progresses from reactant complex **9**, the $O\cdots H_9$ distance decreases to 1.367 Å in **TS2**, then to 0.980 Å in the product complex **2**. However, the $N_9-H_9$ bond length increases from 1.019 Å in the reactant complex **9**, to 1.147 Å at **TS2**, and finally to 1.957 Å in the product complex **2**.

For this reaction pathway (green in Figure 7), the reactant complex **9** has a binding energy of 10.66 (8.84 including ZPVE) kcal mol$^{-1}$ relative to separated adenine plus OH radical. The transition state **TS2** also lies below the separated reactants, by 3.68 (5.47) kcal mol$^{-1}$. The local barrier for this reaction pathway is predicted to be 6.98 (3.37) kcal mol$^{-1}$ relative to reactant complex **9**. This is higher than the transition state for abstraction of $H_{62}$, but lower than that of $H_{61}$ (discussed in the following sections). This reaction results in the lowest energy product complex **2**, which lies 24.21 (22.94) kcal mol$^{-1}$ below separated adenine plus OH radical and 13.55 (14.10) kcal mol$^{-1}$ lower in energy than reactant complex **9**. The dissociation energy for **2** is predicted to be 6.85 (5.06) kcal mol$^{-1}$ with respect to separated $(A-H_9)\cdot$ plus water. It should be noted that although $H_9$ is not present in nucleosides and nucleotides, $N_9$ dehydrogenation is still important for the experiments involving nucleobases.

### 4.4.2 $N_{62}$ Dehydrogenation

Hydroxyl radical may also easily attack $H_{62}$ (dark blue pathway, Figure 7), since it is the second most positively charged hydrogen atom in neutral adenine. The optimized geometries of the reactant complex **7**, transition state (**TS1**), and product complex **3** for this reaction pathway are presented in Figure 9. The $N_6-H_{62}$ bond (1.021 Å) in **7** is only 0.01 Å longer than that in

the isolated neutral adenine. $H_{62}$ is hydrogen bonded to the attacking OH radical, with an O$\cdots$H distance of 2.016 Å. The hydrogen of the hydroxyl radical links to $N_7$, forming another hydrogen bond with an H$\cdots N_7$ distance of 1.792 Å. As the dehydrogenation reaction proceeds to **TS1**, the $N_6-H_{62}$ bond lengthens to 1.155 Å, while the O$\cdots H_{62}$ distance decreases to 1.300 Å. When $H_{62}$ is abstracted to form product complex **3**, the $N_6\cdots H_{62}$ distance further elongates to 2.183 Å, while the $N_6-C_6$ bond length shortens to 1.332 Å, *i.e.*, by 0.02 Å compared to complex **7**. The $O-H_{62}$ bond decreases to a normal water O−H bond (0.974 Å) in **3**.

The reactant complex **7** is stabilized by two H-bonds. The binding energy between the adenine and the attacking OH radical is computed to be 11.39 (9.13 with ZPVE) kcal mol$^{-1}$. The local energy barrier (**7**→**TS1**) for the reaction is predicted to be 5.96 (2.72) kcal mol$^{-1}$. There is no barrier for this reaction pathway, since **TS 1** lies 5.43 (6.40) kcal mol$^{-1}$ below separated adenine plus OH radical. After $H_{62}$ is abstracted, the resulting water and the newly formed (A−H)· radical are held together by two hydrogen bonds, forming the [(A−H)$\cdots H_2O$]· product complex **3** with a binding energy of 22.45 (20.79) kcal mol$^{-1}$ relative to the separated reactants. When **3** dissociates to separated products [(A$-H_{62}$)· + $H_2O$], the energy increases by 7.70 (5.52) kcal mol$^{-1}$. Compared to the reactant complex **7**, the product complex **3** is predicted to be 11.06 kcal mol$^{-1}$ lower in energy. Thus, this dehydrogenation reaction energetically favors the [(A−H)$\cdots H_2O$]· complex.

### 4.4.3 $N_{61}$ Dehydrogenation

In order to attack $H_{61}$ (orange pathway, Figure 7), the OH radical binds to adenine at the $N_1$ and $N_6$ positions through two H-bonds, to form the reactant complex **10**. This reaction pathway proceeds through transition state **TS3** to form product complex **4** (Figure 10). The O$\cdots H_{61}$ distance in **10** is found to be 2.221 Å, a long hydrogen bond. The hydrogen in the hydroxyl radical is connected to $N_1$ with a hydrogen bond length of 1.812 Å. In **TS3**, the O$\cdots H_{61}$ separation decreases to 1.358 Å, and further shortens to 0.979 Å in the product complex **4**. Meanwhile, the $N_6-H_{61}$ bond steadily increases along the reaction pathway, from 1.017 Å in **10**, to 1.121 Å in **TS3**, to 1.985 Å in **4**.

Let us now consider the energetics of the reaction A+OH· → **10** → **TS3** → **4** → (A$-H_{61}$)·+$H_2O$. The binding energy for the reactant complex **10** is 10.15 (8.13) kcal mol$^{-1}$ compared to the separated

A plus OH reactants. The most important feature is that the energy of **TS3** lies 2.32 (3.36) kcal mol$^{-1}$ below reactants A + OH·. The lack of any barrier with respect to reactants shows that this process should be facile. There is, of course, a barrier for the local approach of reactant complex **10** to **TS3**, and that barrier is 7.83 (4.77) kcal mol$^{-1}$. Meanwhile, the product complex **4** lies 10.33 (11.11) kcal mol$^{-1}$ below **10**. Unlike the just-discussed $N_{62}$ dehydrogenation product complex **3**, water and the (A−H)· radical in **4** are held together only through one hydrogen bond. The corresponding dissociation energy is 6.80 kcal mol$^{-1}$ relative to separated (A−$H_{61}$)· radical plus $H_2O$. The $N_{61}$ dehydrogenation is comparable to $N_{62}$ dehydrogenation thermodynamically. However, the two pathways are distinct, since the barrier to $NH_2$ rotation in adenine is about 14 kcal mol$^{-1}$. Interestingly, the barrier differs slightly based on the direction of rotation: 13.98 (13.58) kcal mol$^{-1}$ or 14.53 (14.15) kcal mol$^{-1}$. However, experimental discrimination between these two pathways would require deuteration of $H_{61}$ or $H_{62}$.

### 4.4.4 $C_8$ Dehydrogenation

The $C_8$ dehydrogenation pathway (magenta, Figure 7) involves reactant complex **1**, transition state **TS6**, and product complex **8** (see Figure 11). Although reactant complex **1** is a long-lived adduct, and has been characterized by experiment [17,42,43], it will be termed a reactant complex for the sake of consistency. Oxygen bonds to $C_8$ directly in reactant complex **1**, instead of hydrogen bonding. This breaks the $N_7$−$C_8$ double bond and forms the low energy reactant complex **1**. Significant geometric changes occur in the five and six-membered rings since the conjugation of the entire system has been disrupted. As the dehydration reaction proceeds, $H_8$ migrates away from $C_8$, forming a nearly linear (163.8°) $C_8 \cdots H_8 \cdots O$ structure in **TS6**. In the product complex **8**, there are two hydrogen bonds; one of the hydrogen atoms from the newly formed water molecule hydrogen bonds to $N_3$ ($N_3 \cdots H_8$ distance is 1.953 Å), while the oxygen hydrogen bonds to $H_9$ ($O \cdots H_9$ atomic distance is 2.050 Å).

Reactant complex **1** is extraordinarily stable; the binding energy [32.79 (29.64) kcal mol$^{-1}$ relative to separated A + OH·] is much greater than that of the other dehydrogenation reactant complexes. However, dehydrogenation at $C_8$ is disfavored for several reasons. It is predicted to have a large local barrier [37.14 (31.53) kcal mol$^{-1}$] with respect to the reactant complex **1**. In addition,

only this reaction pathway leads to a product complex (**8**) which lies above the corresponding reactant complex (**1**), by 21.88 (20.77) kcal mol$^{-1}$. Moreover, only the transition state (**TS6**) of this pathway lies appreciably (4.35 kcal mol$^{-1}$) above separated reactants A + OH·, indicating that $C_8$ dehydrogenation is unlikely at low temperatures. These energetics may explain the experimental inference that ring-opening, not dehydrogenation, occurs when OH radical attacks the $C_8$ position of adenine.[41,44]

### 4.4.5 $C_2$ Dehydrogenation

Abstraction of atom $H_2$ from adenine is complicated by the fact that two transition states **TS4** (Figure 12) and **TS5** (Figure 13) have been located (light blue and red pathways, in Figure 7). This indicates that there are two reaction pathways for $C_2$ dehydrogenation. **TS4** and **TS5** have similar geometries, except for the orientation of the OH radical. The energy difference between **TS4** and **TS5**, due to OH rotation, is only 0.04 (0.08) kcal mol$^{-1}$. In **TS4** and **TS5**, atom $C_2$, as discussed above (abstraction of $H_8$), is directly bonded to a hydrogen atom, so a reactant complex analogous to complex **1**, with OH radical directly attacking carbon, was considered. However, intrinsic reaction coordinate (IRC) analyses reveal that **TS4** connects the reactant complex **9** and the product complex **5**. Similarly, **TS5** connects the reactant complex **10** and the product complex **6**. This indicates that OH radical directly attacking $C_2$ does not lead to dehydrogenation. In both product complexes **5** and **6**, two new hydrogen bonds are formed.

For these two reaction pathways, the reactant complexes are the same as in the $N_9$ and $N_{61}$ dehydrogenations. The transition state **TS4** for hydroxyl H pointing "down" (Figure 12) lies 0.77 kcal mol$^{-1}$ above separated A plus OH radical. The transition state **TS5** for hydroxyl H pointing "up" (Figure 13) lies 0.81 kcal mol$^{-1}$ above the separated reactants. Inclusion of the ZPVE corrections decreases the energies to $-1.34$ and $-1.42$ kcal mol$^{-1}$. The local barriers for these two reaction pathways are predicted to be 11.42 (7.42) and 10.95 (6.79) kcal mol$^{-1}$ relative to the reactant complexes **9** and **10**. Though these local barriers are not as high as for the $C_8$ dehydrogenation reaction, they are much higher than those for the $N_9$ and $N_{61}$ dehydrogenations. The binding energies are 18.69 (16.71) and 17.47 (15.18) below separated adenine plus OH radical for product complexes **5**

and **6**. The dissociation energies are predicted to be 10.84 (8.65) and 9.62 (7.12) kcal mol$^{-1}$ for the two product complexes relative to separated (A−$H_2$)· radical plus water.

### 4.4.6 Energetics

Table 2 reports the relative enthalpies, relative entropies and relative Gibbs energies for the six dehydrogenation reaction transition states. All energies are relative to separated adenine plus OH· radical. The relative enthalpies and entropies are all negative for all the transition states. Therefore, low temperatures favor all these dehydrogenation reactions. There are two transition states with different OH orientation at the $C_2$ position, **TS4** and **TS5**. The reaction enthalpy barriers differ only by 0.02 kcal mol$^{-1}$, so these two reactions may happen simultaneously, based on the direction of the OH radical attack.

The energy profiles along the six reaction pathways [A+OH· → reactant complexes → **TS** → product complexes → (A−H)·+$H_2O$] are shown in Figure 7. The most important feature is that all the transition states lie near or below separated A + OH· in energy, except for **TS6** on the $C_8$ pathway. The lack of any barrier with respect to reactants shows that these processes, except for $C_8$ dehydrogenation, should be facile. Based on the transition state energies, the dehydrogenation of $N_{62}(H_{62})$ is the most kinetically favorable reaction pathway with a transition state lying 5.43 kcal mol$^{-1}$ below separated adenine plus OH radical. It is followed by $N_9$ and $N_6(H_{61})$ dehydrogenation (3.68 and 2.32 kcal mol$^{-1}$, respectively, below separated reactants). The $C_2$ dehydrogenation transition state energies vary based on hydroxyl orientation; 0.77 and 0.81 kcal mol$^{-1}$ above separated reactants, for H from hydroxyl radical pointing "down" and "up", respectively. Note that with the ZPVE correction these transition states lie below the separated reactants. Dehydrogenation at the $C_8$ site is energetically least favored, with a transition state 4.35 kcal mol$^{-1}$ above separated adenine plus OH radical.

### 4.4.7 Optical Transitions

TD-DFT computed absorption spectra for adenine, the four reactant complexes, and the five dehydrogenated adenine radicals are shown in Table 4. In this context Vieira and Steenken[41] recorded optical absorption spectra in the 250 − 700 nm region. Their initial spectrum was measured

2 $\mu$s after the reaction of OH radical with adenine. Additional spectra were recorded 30 $\mu$s after completion of the first-order transformation reaction.

The laboratory spectrum recorded 2$\mu$s after the reaction showed small peaks around 300 and 400 nm, with a broad peak from $450 - 600$ nm. In our computations, the $N_9$, $N_{61}$, and $N_{62}$-dehydrogenated adenine radicals have strong transitions in the 300 nm region. For $N_9$, the main transitions are at 302 nm ($f = 0.050$), 312 nm ($f = 0.068$); for $N_{61}$, 298 nm ($f = 0.080$); and for $N_{62}$, 300 nm ($f = 0.079$). These products were not mentioned in Vieira and Steenken's work. Vieira and Steenken assigned the features around 400 nm to the dehydration reaction of the A4OH radical.[41] However, the $\cdot OH + A \rightarrow A4OH\cdot \rightarrow A{-}H_6\cdot + H_2O$ reaction was not considered in our work, since the mechanism involves a complex series of proton transfers. Our TD-DFT computations indicate that $N_{61}$ and $N_{62}$-dehydrogenated adenine radical products have optical transitions in this region; that is, $\lambda = 421$ nm ($f = 0.017$) and $\lambda = 427$ nm ($f = 0.015$), respectively.

After 30 $\mu$s, the Vieira-Steenken spectrum showed a significant increase of optical density (OD) at about 330 nm, compared to the 2 $\mu$s spectrum. This feature was assigned by Steenken to the ring-opening reaction of A8OH radical. There is also a very broad, though weak, peak in the 450-700 nm region. As mentioned above, the $N_{61}$, and $N_{62}$-dehydrogenated adenine radicals have transitions in this region. However, none of these transitions is very strong. The $C_8$ reactant complex **1** does have a strong transition at 313 nm ($f = 0.135$); see Table 4. It has a significant shoulder at a higher wavelength (335 nm, $f = 0.032$) and several weak shoulders in the $242{-}451$ nm region. This peak cannot be definitively assigned, since we focused on dehydrogenation reactions of adenine in this work. The ring-opening reaction transients and products, as mentioned before,[40,41,44–46] may present strong transitions corresponding to these shorter wavelength peaks.

## 4.5 Conclusions

Six possible dehydrogenation reaction pathways for adenine attacked by the hydroxyl radical have been investigated at the B3LYP/DZP++ level of theory. The $N_{62}$, $N_9$, and $N_{61}$ pathways have transition states lower in energy than separated adenine and hydroxyl radical; $-5.43$, $-3.68$, and $-2.32$ kcal mol$^{-1}$, respectively. After including the ZPVE corrections, only the $C_8$ dehydrogenation transition state is higher in energy higher than the separated reactants. This suggests that, except

for attacking at the $C_8$ site, OH radical attack at all other positions will lead to dehydrogenation spontaneously, forming an adenine radical and water. Based on energetic analyses, the reactions at $N_9$, $N_{61}$, and $N_{62}$ are exothermic, while those at $C_2$ and $C_8$ are endothermic. Since $N_{62}$ has the lowest lying transition state, it is the most kinetically favorable pathway for dehydrogenation. Other compatible pathways are the dehydrogenation at $N_9$ and $N_{61}$. Dehydrogenation at $C_2$ is less favorable than at the $N_9$ and $N_{61}$ positions. For the $C_8$ pathway, though the activation energy is 4.35 kcal $mol^{-1}$ relative to separated A plus OH radical, the local barrier is 37.14 kcal $mol^{-1}$ with respect to reactant complex **1**. These relatively high barriers indicate that $C_8$ dehydrogenation is unlikely to take place; ring-opening reaction may occur in agreement with early experiments.[41,44] The TD-DFT computed transitions of $N_{61}$ at 421 nm and $N_{62}$ 427 nm agree well with the early experimental assignment of a 400 nm band to dehydrogenation at $N_6$ position. The $N_6$ position is most favorable for OH radical attack, leading to formation of $N_6$-dehydrogenated adenine radicals.

## 4.6 Acknowledgments

The authors would like to thank Heather M. Jaeger, Dr. Francesco A. Evangelista and Dr. Yaoming Xie for insightful discussions and technical expertise. This research was funded by the U.S. National Science Foundation, Grant CHE−0749868.

Table 4.1: Energies ($\Delta$E, in kcal mol$^{-1}$, ZPVE corrected values in parentheses) of the five dehydrogenated adenine radicals [(A$-$H)$\cdot$] plus water, relative to separated adenine plus OH radical. Also reported are reaction enthalpies ($\Delta$H, in kcal mol$^{-1}$), entropies ($\Delta$S, in cal mol$^{-1}$), and Gibbs energies ($\Delta$G, in kcal mol$^{-1}$) for A + OH$\cdot$ $\rightarrow$ (A$-$H)$\cdot$ + $H_2O$.

| | $\Delta$E | | $\Delta$H | $\Delta$S | $\Delta$G |
|---|---|---|---|---|---|
| $N_9$-dehydrogenated adenine | $-17.36$ | $(-17.88)$ | $-0.30$ | 3.33 | $-1.30$ |
| $N_{62}$-dehydrogenated adenine | $-14.75$ | $(-15.27)$ | $-0.53$ | 2.07 | $-1.14$ |
| $N_{61}$-dehydrogenated adenine | $-13.67$ | $(-14.20)$ | $-0.54$ | 2.04 | $-1.15$ |
| $C_2$-dehydrogenated adenine | $-7.85$ | $(-8.06)$ | 0.24 | 5.28 | $-1.34$ |
| $C_8$-dehydrogenated adenine | $-0.30$ | $(-0.43)$ | 0.24 | 4.04 | $-0.96$ |

Table 4.2: Relative energies[a] ($E_{rel}$, in kcal mol$^{-1}$, ZPVE corrected values in parentheses,) of sixteen structures with respect to separated adenine plus OH radical, and the dissociation energies with respect to separated dehydrogenated adenine radical plus water (DE, in kcal mol$^{-1}$, ZPVE corrected values in parentheses).

| | Description | $E_{rel}$ A + OH· | | DE (A−H)· + $H_2O$ | |
|---|---|---|---|---|---|
| **1** | $[A_{H_8} \cdots OH]\cdot$ | −32.79 | (−29.64) | 32.49 | (29.21) |
| **2** | $[(A-H)_{N_9} \cdots H_2O]\cdot$ | −24.21 | (−22.94) | 6.85 | (5.06) |
| **3** | $[(A-H)_{N_{62}} \cdots H_2O]\cdot$ | −22.45 | (−20.79) | 7.70 | (5.52) |
| **4** | $[(A-H)_{N_{61}} \cdots H_2O]\cdot$ | −20.47 | (−19.24) | 6.80 | (5.04) |
| **5**[a] | $[(A-H)_{C_{21}} \cdots H_2O]\cdot$ | −18.69 | (−16.71) | 10.84 | (8.65) |
| **6**[b] | $[(A-H)_{C_{22}} \cdots H_2O]\cdot$ | −17.47 | (−15.81) | 9.62 | (7.12) |
| **7** | $[A_{H_{62}} \cdots OH]\cdot$ | −11.39 | (−9.13) | −3.36 | (−6.14) |
| **8** | $[(A-H)_{C_8} \cdots H_2O]\cdot$ | −10.91 | (−8.87) | 10.61 | (8.44) |
| **9** | $[A_{H_9} \cdots OH]\cdot$ | −10.66 | (−8.84) | −6.71 | (−9.04) |
| **10** | $[A_{H_{61}} \cdots OH]\cdot$ | −10.15 | (−8.13) | −3.52 | (−6.07) |
| **TS1** | $N_{62}$ position | −5.43 | (−6.40) | −9.31 | (−8.87) |
| **TS2** | $N_9$ position | −3.68 | (−5.47) | −13.68 | (−12.41) |
| **TS3** | $N_{61}$ position | −2.32 | (−3.36) | −11.35 | (−10.85) |
| **TS4**[b] | $C_{21}$ position | 0.77 | (−1.42) | −8.61 | (−6.64) |
| **TS5**[c] | $C_{22}$ position | 0.81 | (−1.34) | −8.65 | (−6.72) |
| **TS6** | $C_8$ position | 4.35 | (1.89) | −4.65 | (−2.31) |

[a]These are also the negative values of binding energies.
[b]$C_{21}$ is for transition state and product of $C_2$ position reaction with a lower energy, see Figure 10.
[c]$C_{22}$ is for transition state and product of $C_2$ position reaction with a higher energy, see Figure 11.

Table 4.3: Barrier heights ($\Delta H^{\ddagger}$, in kcal mol$^{-1}$), barrier entropy changes ($\Delta S^{\ddagger}$, in cal mol$^{-1}$), and ordered Gibbs energies of activation ($\Delta G^{\ddagger}$, in kcal mol$^{-1}$) with respect to separated adenine plus OH radical at 298.18 K for the six dehydrogenation reactions [A + OH$\cdot$ $\rightarrow$ TS $\rightarrow$ (A$-$H)$\cdot$ + $H_2O$].

| | $\Delta H^{\ddagger}$ | $\Delta S^{\ddagger}$ | $\Delta G^{\ddagger}$ |
|---|---|---|---|
| **TS1** ($N_{62}$ position) | -2.06 | -32.67 | 7.68 |
| **TS2** ($N_9$ position) | -2.32 | -28.00 | 6.03 |
| **TS3** ($N_{61}$ position) | -1.81 | -29.47 | 6.98 |
| **TS4** ($C_{21}$ position) | -2.51 | -26.22 | 5.31 |
| **TS5** ($C_{22}$ position) | -2.53 | -27.03 | 5.53 |
| **TS6** ($C_8$ position) | -2.79 | -27.13 | 5.29 |

Table 4.4: Vertical optical transitions (absorption spectra $\lambda$ in nm) of the adenine molecule, four reactant complexes, and five dehydrogenated adenine radicals, predicted using the TD-DFT approach. Oscillator strengths ($f$) are reported for transitions $\geq 0.010$ in magnitude.

| | $\lambda$ ($f$) | $\lambda$ ($f$) | $\lambda$ ($f$) | $\lambda$ ($f$) | $\lambda$ ($f$) | $\lambda$ ($f$) | $\lambda$ ($f$) | $\lambda$ ($f$) |
|---|---|---|---|---|---|---|---|---|
| adenine | 203 (0.096) | 204 (0.035) | 239 (0.034) | 250 (0.202) | | | | |
| **1** $C_8$ site reactant complex | 242 (0.068) | 244 (0.035) | 245 (0.018) | 260 (0.022) | 313 (0.135) | 335 (0.032) | 451 (0.013) | |
| **9** $N_9$ site reactant complex | 238 (0.038) | 250 (0.221) | | | | | | |
| **10** $N_{61}$ site reactant complex | 241 (0.070) | 251 (0.206) | | | | | | |
| **7** $N_{62}$ site reactant complex | 240 (0.036) | 258 (0.187) | | | | | | |
| $C_2$-dehydrogenated A | 245 (0.207) | 259 (0.010) | | | | | | |
| $C_8$-dehydrogenated A | 228 (0.019) | 237 (0.112) | 241 (0.080) | 247 (0.014) | | | | |
| $N_9$-dehydrogenated A | 242 (0.037) | 259 (0.024) | 277 (0.019) | 302 (0.050) | 312 (0.068) | 522 (0.033) | | |
| $N_{61}$-dehydrogenated A | 250 (0.024) | 277 (0.016) | 298 (0.080) | 421 (0.017) | 505 (0.034) | | | |
| $N_{62}$-dehydrogenated A | 222 (0.025) | 229 (0.048) | 252 (0.052) | 261 (0.031) | 279 (0.022) | 300 (0.079) | 427 (0.015) | 506 (0.036) |

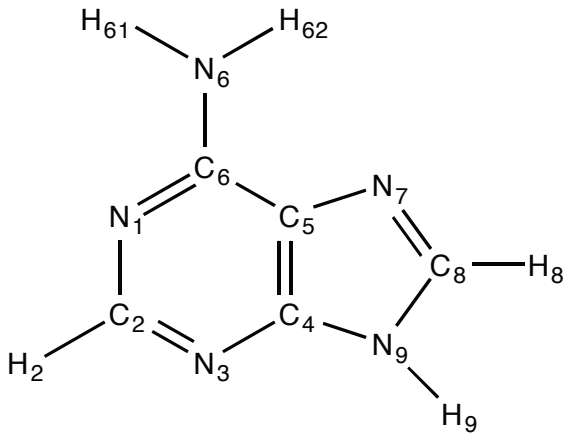


Figure 4.1: IUPAC numbering of atoms for adenine.

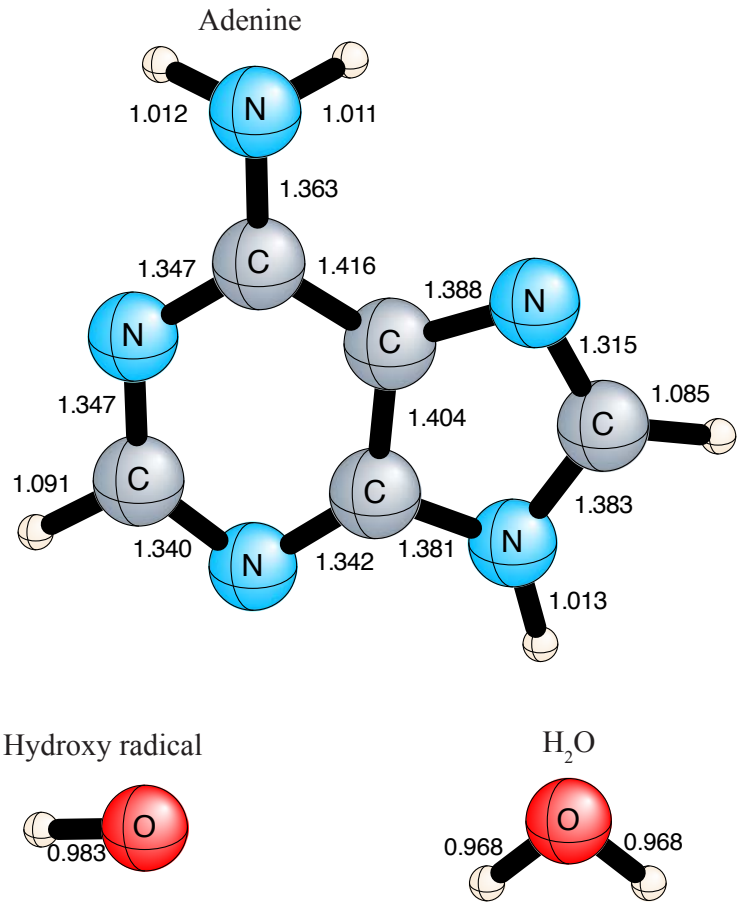


Figure 4.2: Optimized geometries of isolated adenine, hydroxyl radical and water, with bond lengths in Å.

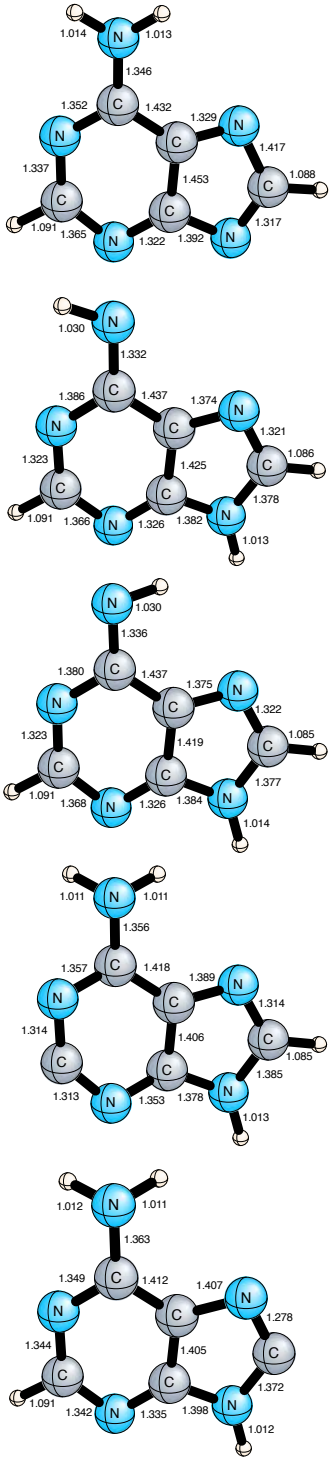


Figure 4.3: Five optimized structures for (A−H) radicals, *i.e.*, structures resulting from the removal of one hydrogen atom from adenine. Bond distances are in Å.

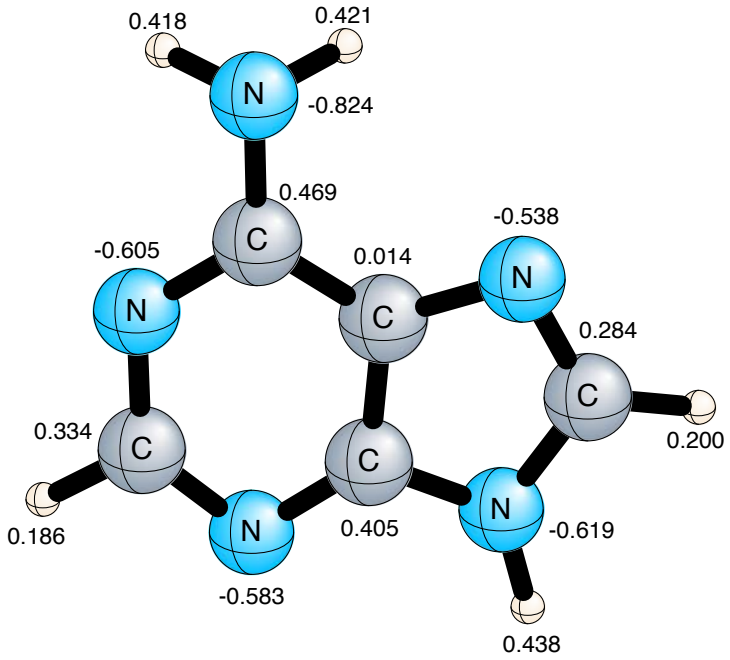


Figure 4.4: Natural population analysis (NPA) for neutral adenine.

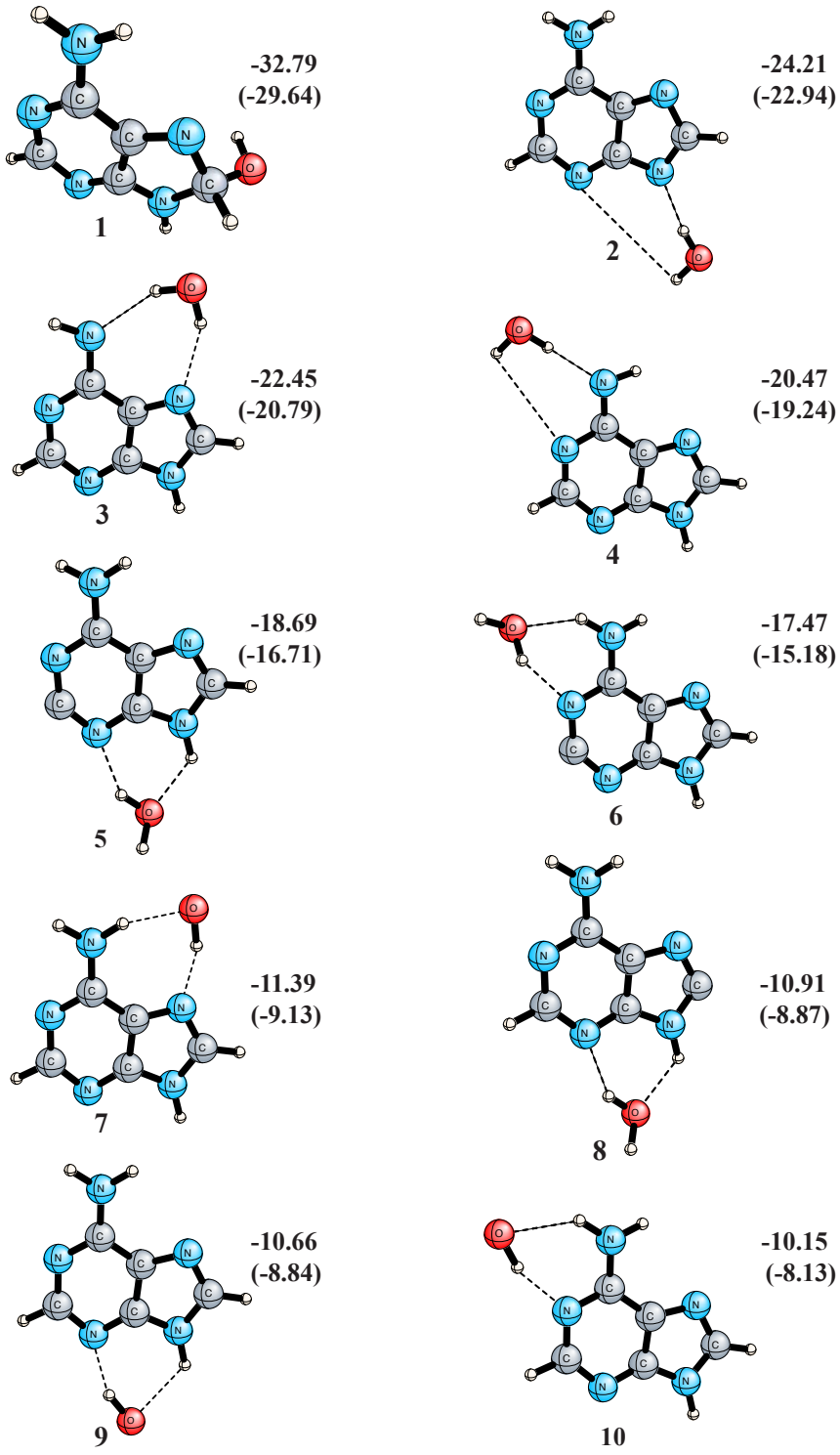


Figure 4.5: Numbering of the ten adenine-OH and (A−H)-$H_2O$ radical complexes. Relative energies(in kcal $mol^{-1}$, ZPVE corrected values in parentheses) are reported with respect to separated adenine and hydroxyl radical.

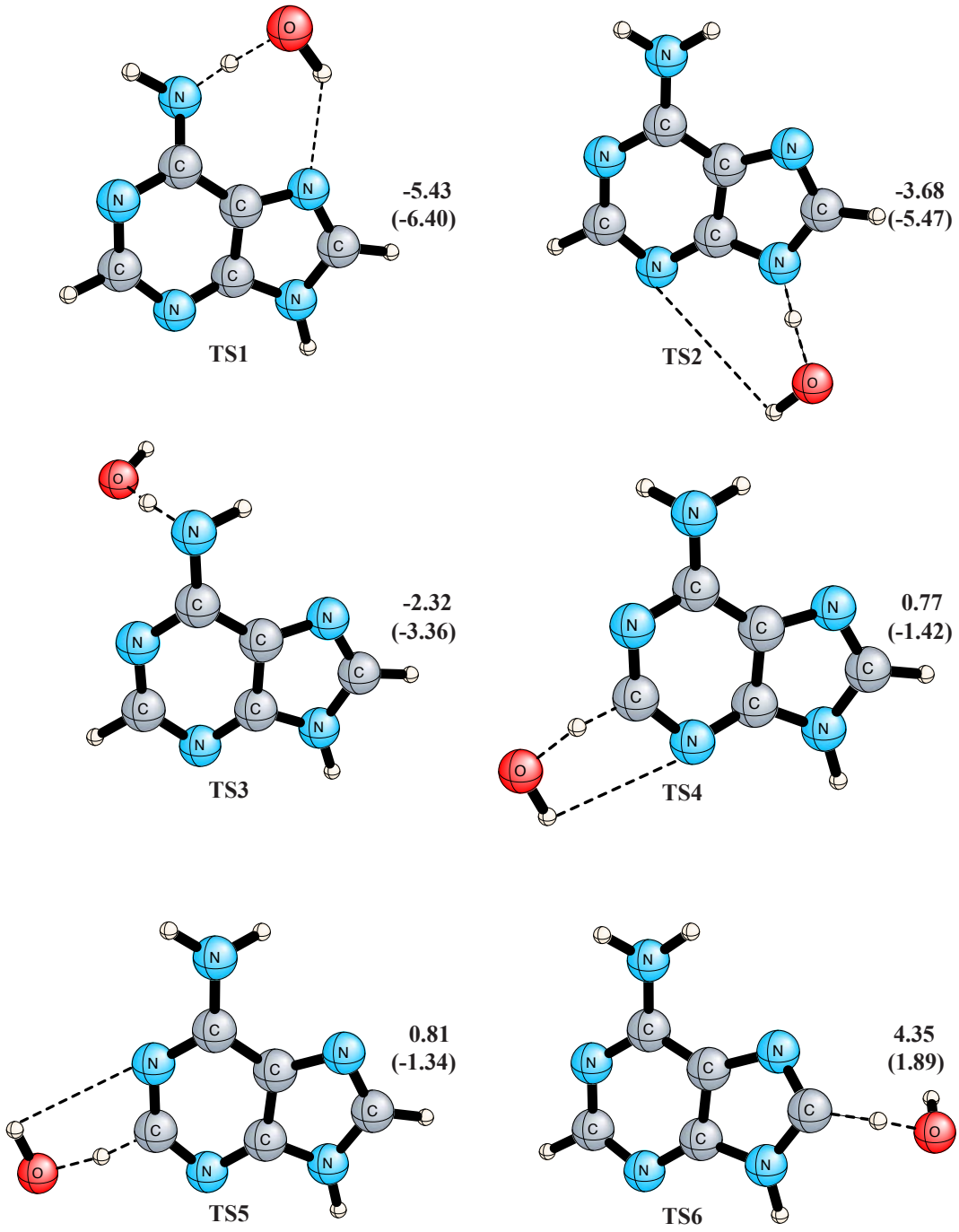


Figure 4.6: Numbering of the six A + OH→ (A−H) + $H_2O$ transition states. Relative energies (in kcal $mol^{-1}$, ZPVE corrected values in parentheses) are reported with respect to separated adenine and hydroxyl radical.

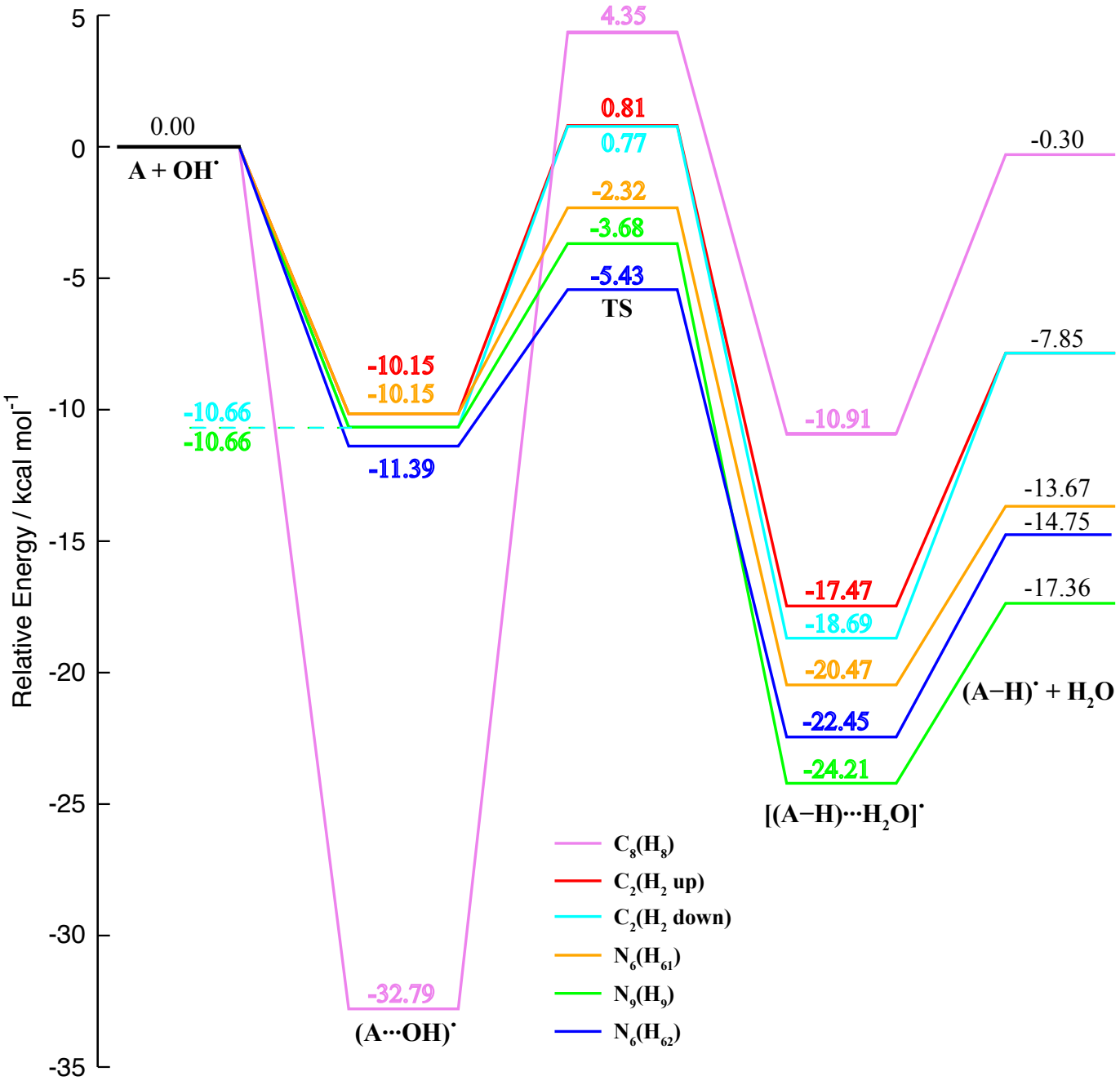


Figure 4.7: Relative energies (in kcal $mol^{-1}$) with respect to separated adenine and hydroxyl radical.

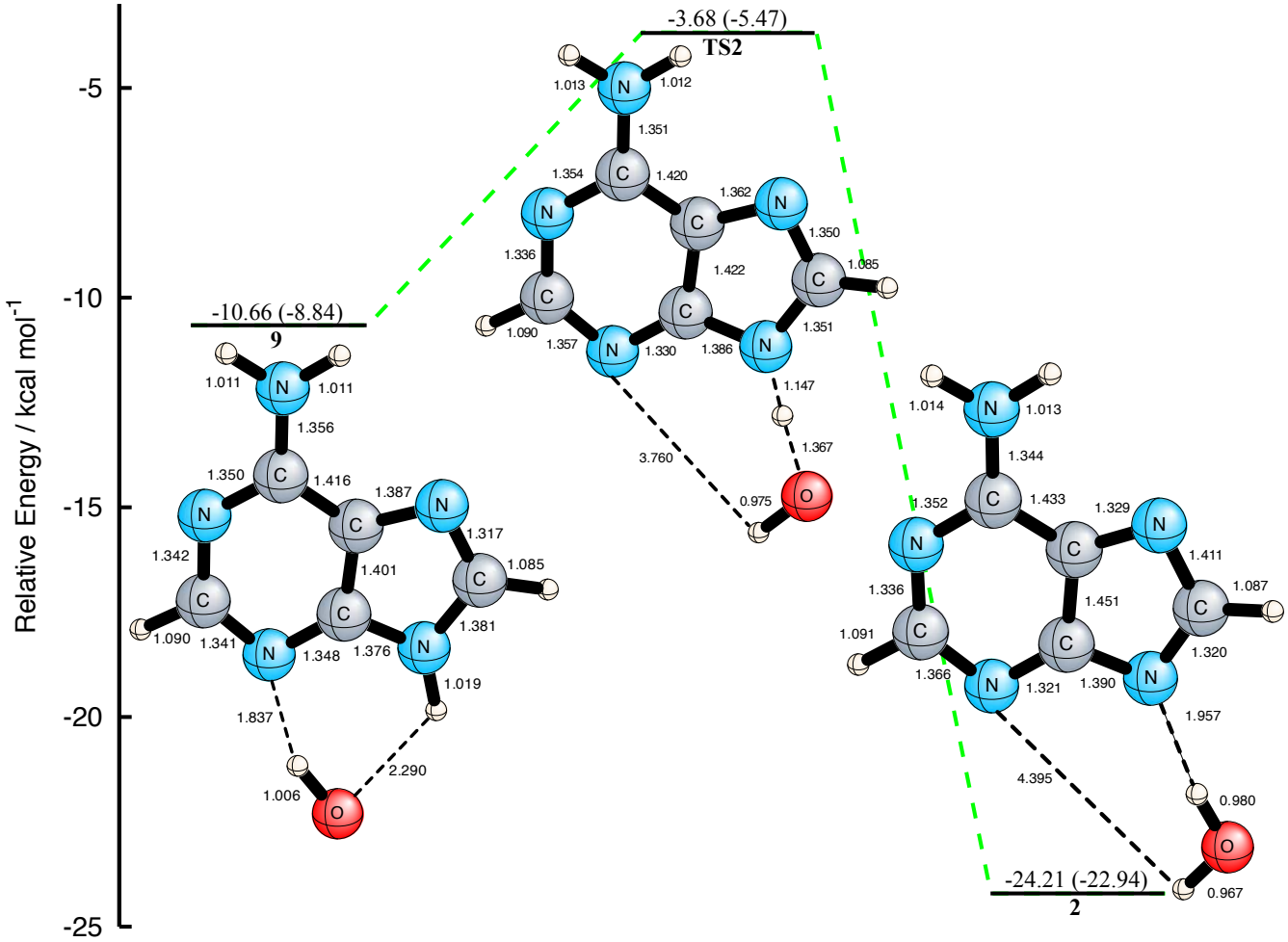


Figure 4.8: Optimized geometries for the hydroxyl radical attack on adenine position $(N_9)H_9$. Included in the figure are the reactant complex (**9**), transition state (**TS2**), and product complex (**2**). Bond lengths are in Å. Relative energies (in kcal $mol^{-1}$, ZPVE corrected values in parentheses) are given with respect to separated A+OH.

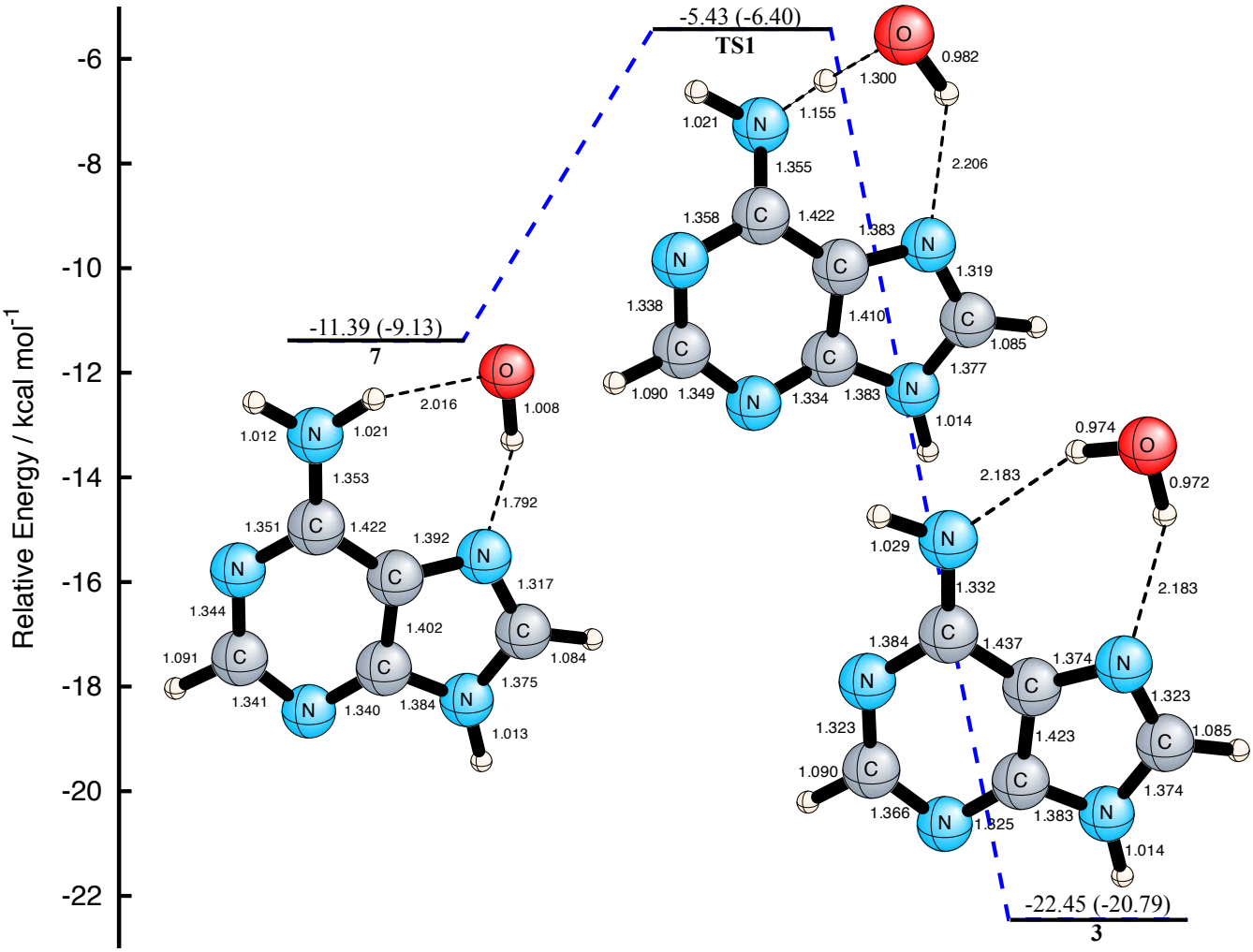


Figure 4.9: Optimized geometries for the hydroxyl radical attack on adenine position $(N_6)H_{62}$. Included in the figure are the reactant complex (**7**), transition state (**TS1**), and product complex (**3**). Bond lengths are in Å. Relative energies (in kcal mol$^{-1}$, ZPVE corrected values in parentheses) are given with respect to separated A+OH.

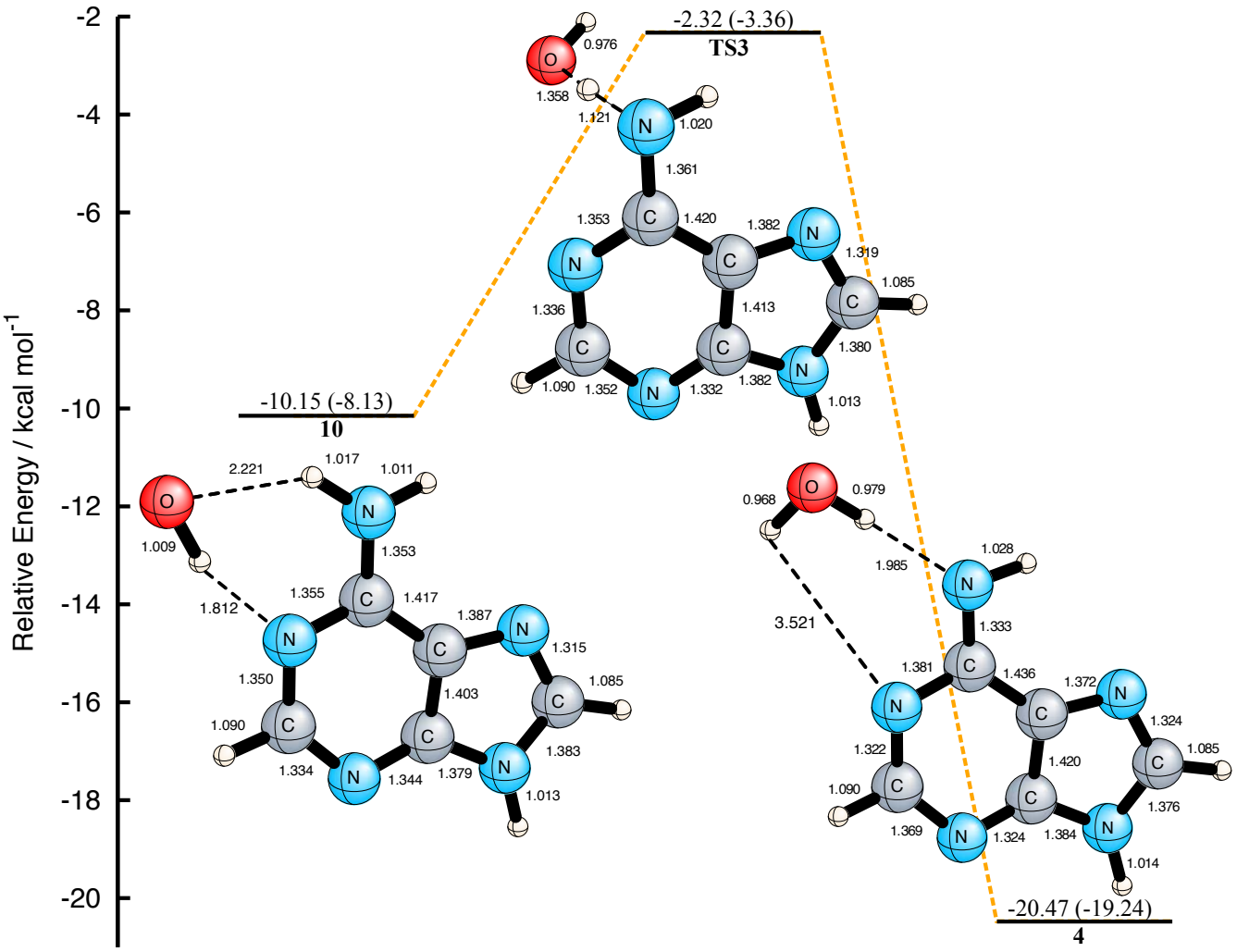


Figure 4.10: Optimized geometries for the hydroxyl radical attack on adenine position $(N_6)H_{61}$. Included in the figure are the reactant complex (**10**), transition state (**TS3**), and product complex (**4**). Bond lengths are in Å. Relative energies (in kcal $mol^{-1}$, ZPVE corrected values in parentheses) are given with respect to separated A+OH.

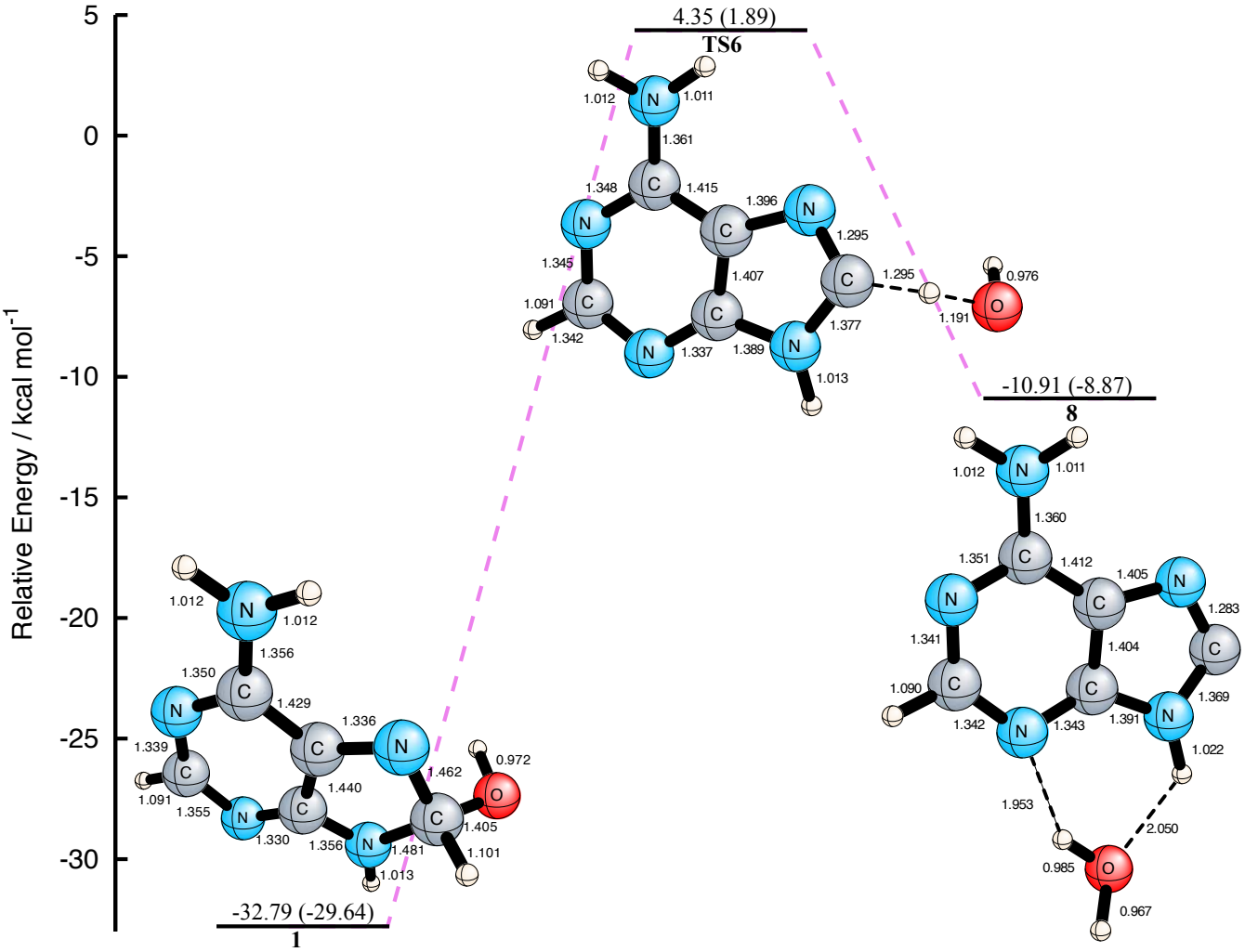


Figure 4.11: Optimized geometries for the hydroxyl radical attack on adenine position $(C_8)H_8$. Included in the figure are the reactant complex (**1**), transition state (**TS6**), and product complex (**8**). Bond lengths are in Å. Relative energies (in kcal $mol^{-1}$, ZPVE corrected values in parentheses) are given with respect to separated A+OH.

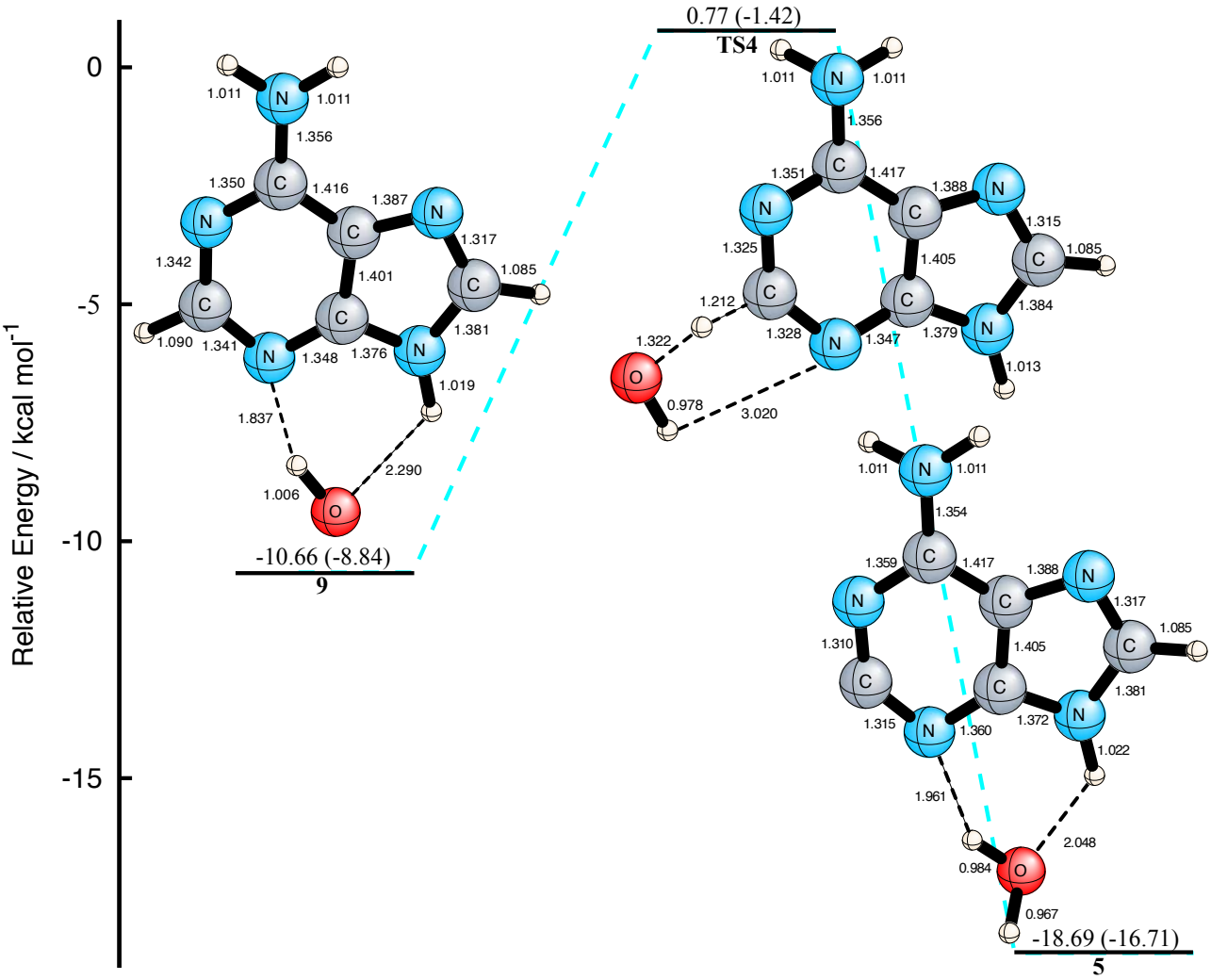


Figure 4.12: Optimized geometries for the hydroxyl radical attack on adenine position $(C_2)H_2$. Included in the figure are the reactant complex (**9**), transition state (**TS4**), and product complex (**5**). Bond lengths are in Å. Relative energies (in kcal $mol^{-1}$, ZPVE corrected values in parentheses) are given with respect to separated A+OH.

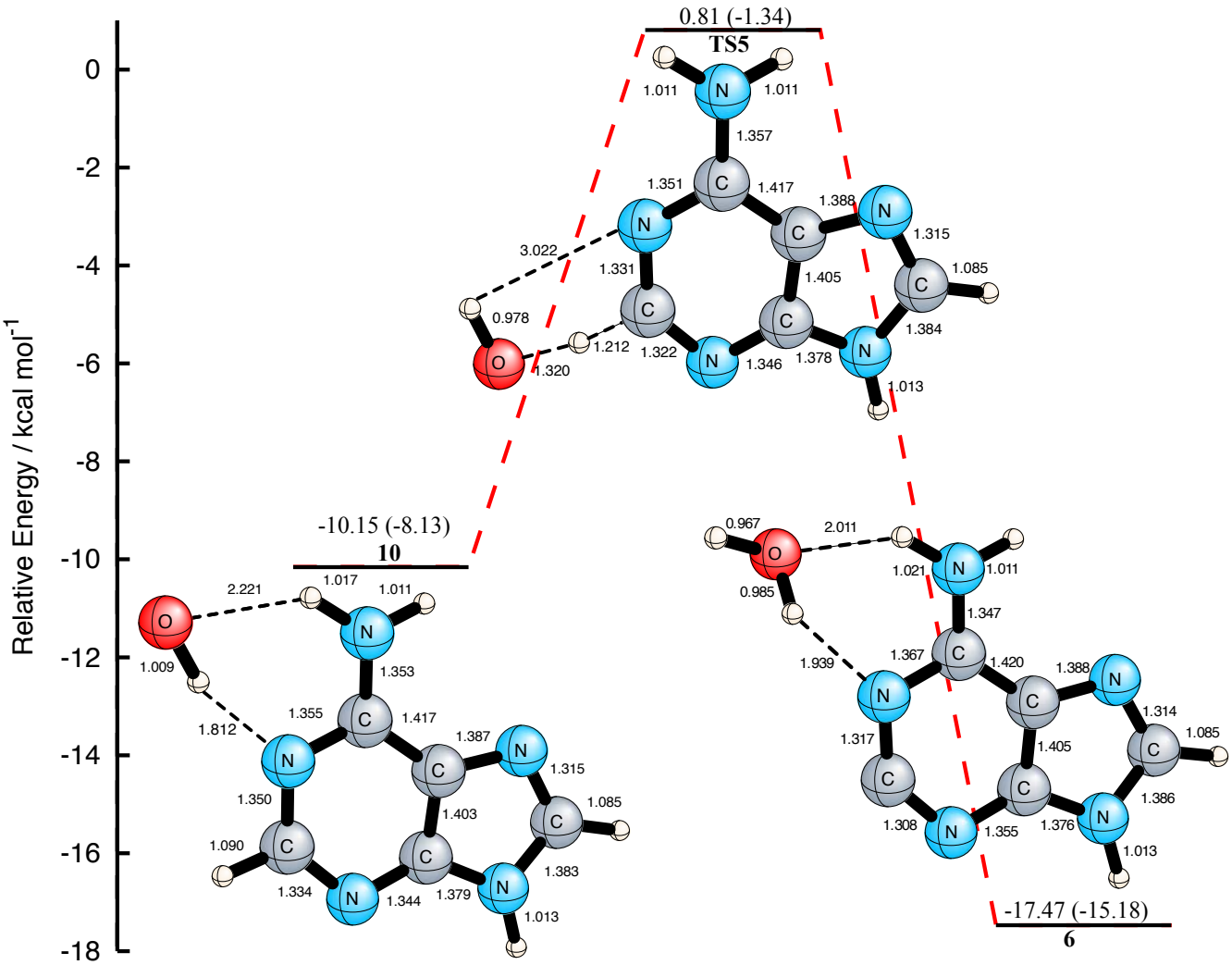


Figure 4.13: Optimized geometries for the hydroxyl radical attack on adenine position $(C_2)H_2$. Included in the figure are the reactant complex (**10**), transition state (**TS5**), and product complex (**6**). Bond lengths are in Å. Relative energies (in kcal $mol^{-1}$, ZPVE corrected values in parentheses) are given with respect to separated A+OH.

## Bibliography


[1] D. K. Hazra, S. Steenken, *J. Am. Chem. Soc.* **1983**, *105*, 4380.

[2] E. Sagstuen, E. O. Hole, W. H. Nelson, D. M. Close, *J. Phys. Chem.* **1992**, *96*, 1121.

[3] E. Sagstuen, E. O. Hole, W. H. Nelson, D. M. Close, *J. Phys. Chem.* **1992**, *96*, 8269.

[4] D. M. Close, *Radiat. Res.* **1993**, *135*, 1.

[5] A. O. Colson, M. D. Sevilla, *J. Phys. Chem.* **1995**, *99*, 13033.

[6] D. M. Close, L. A. Eriksson, E. O. Hole, E. Sagstuen, W. H. Nelson, *J. Phys. Chem. B* **2000**, *104*, 9343.

[7] M. Krauss, R. Osman, *J. Phys. Chem. A* **1997**, *101*, 4117.

[8] A. O. Colson, D. Becker, I. Eliezer, M. D. Sevilla, *J. Phys. Chem. A* **1997**, *101*, 8935.

[9] S. Steenken, S. V. Jovanovic, *J. Am. Chem. Soc.* **1997**, *119*, 617.

[10] S. D. Wetmore, R. J. Boyd, *J. Phys. Chem. B* **1998**, *102*, 9332.

[11] S. D. Wetmore, F. Himo, R. J. Boyd, L. A. Eriksson, *J. Phys. Chem. B* **1998**, *102*, 7484.

[12] S. D. Wetmore, R. J. Boyd, L. A. Eriksson, *J. Phys. Chem. B* **1998**, *102*, 10602.

[13] S. D. Wetmore, R. J. Boyd, L. A. Eriksson, *J. Phys. Chem. B* **1998**, *102*, 5369.

[14] S. D. Wetmore, R. J. Boyd, F. Himo, L. A. Eriksson, *J. Phys. Chem. B* **1999**, *103*, 3051.

[15] S. D. Wetmore, R. J. Boyd, L. A. Eriksson, *Chem. Phys. Lett.* **2000**, *322*, 129.

[16] J. Cadet, T. Delatour, T. Douki, D. Gasparutto, J. P. Pouget, J. L. Ravanat, S. Sauvaigo, *Mutat. Res.* **1999**, *424*, 9.

[17] L. P. Candeias, S. Steenken, *Chem.−Eur. J.* **2000**, *6*, 475.

[18] S. S. Wallace, *Free Rad. Biol. Med.* **2002**, *33*, 1.

[19] C. J. Mundy, M. E. Colvin, A. A. Quong, *J. Phys. Chem. A* **2002**, *106*, 10063.

[20] R. Kakkar, R. Garg, *J. Mol. Struct.* **2003**, *620*, 139.

[21] Y. Wu, C. J. Mundy, M. E. Colvin, R. Car, *J. Phys. Chem. A* **2004**, *108*, 2922.

[22] K. C. Hunter, L. R. Rutledge, S. D. Wetmore, *J. Phys. Chem. A* **2005**, *109*, 9554.

[23] M. H. Almatarneh, C. G. Flinn, R. Poirier, *J. Phys. Chem. A* **2006**, *110*, 8227.

[24] R. B. Zhang, L. A. Eriksson, *J. Phys. Chem. B* **2007**, *111*, 6571.

[25] J. D. Zhang, H. F. Schaefer, *J. Chem. Theory Comput.* **2007**, *3*, 115.

[26] M. H. Almatarneh, C. G. Flinn, R. Poirier, *J. Chem. Inf. Model* **2008**, *48*, 831.

[27] R. H. D. Lyngdoh, H. F. Schaefer, *Acc. Chem. Res.* **2009**, *42*, 563.

[28] A. Kumar, M. D. Sevilla, *Chem. Rev.* **2010**.

[29] B. Halliwell, I. Okezie, E. Aruoma, *DNA and Free Radicals, 2nd ed.*, Ellis Horwood Ltd.: New York, **1993**.

[30] C. Von Sonntag, *The Chemical Basis of Radiation Biology*, Taylor & Francis: London, **1987**.

[31] M. Dizdaroglou, *Free Rad. Biol. Med.* **1991**, *10*, 225.

[32] N. L. Oleinick, S. Cluh, N. Ramakrishman, L. Xue, *Br. J. Cancer* **1987**, *55*, Suppl. VIII 135.

[33] B. Halliwell, J. M. C. Gutteridge, *Free Radicals in Biology and Medicine*, Clarendon Press: Oxford, **1989**.

[34] A. J. Bertinchamps, J. Hüttermann, W. Köhnlein, R. Teoule, *Effects of Ionizing Radiation on DNA*, Springer: Berlin, **1987**.

[35] W. A. Bernhard, *Adv. Radiat. Biol.* **1981**, *9*, 199.

[36] J. P. Pouget, S. Frelon, J. L. Ravanat, I. Testard, F. Odin, J. Cadet, *Radiat. Res.* **2002**, *157*, 589.

[37] J. Cadet, E. Sage, T. Douki, *Mutat. Res.* **2005**, *571*, 3.

[38] B. Aydogan, W. E. Bolch, S. G. Swarts, J. E. Turner, D. T. Marshall, *Radiat. Res.* **2008**, *169*, 223.

[39] C. Chatgilialoglu, M. D'Angelantonio, M. Guerra, P. Kaloudis, Q. G. Mulazzani, *Angew. Chem. Int. Ed.* **2009**, *48*, 2214.

[40] S. Steenken, *Chem. Rev.* **1989**, *89*, 503.

[41] A. J. S. C. Vieira, S. Steenken, *J. Am. Chem. Soc.* **1990**, *112*, 6986.

[42] A. J. S. C. Vieira, S. Steenken, *J. Phys. Chem.* **1991**, *92*, 9341.

[43] P. O'Neill, *Radiat. Res.* **1983**, *96*, 198.

[44] A. J. S. C. Vieira, S. Steenken, *J. Phys. Chem.* **1987**, *91*, 4138.

[45] J. Llano, L. A. Eriksson, *Phys. Chem. Chem. Phys.* **2004**, *6*, 4707.

[46] S. Naumov, C. V. Sonntag, *Radiat. Res.* **2008**, *169*, 355.

[47] E. O. Hole, E. Sagstuen, W. H. Nelson, D. M. Close, *Radiat. Res.* **1995**, *144*, 258.

[48] D. M. Close, W. H. Nelson, *Radiat. Res.* **1989**, *117*, 367.

[49] W. H. Nelson, E. Sagstuen, E. O. Hole, D. M. Close, *Radiat. Res.* **1992**, *131*, 272.

[50] L. Kar, W. A. Bernhard, *Radiat. Res.* **1983**, *93*, 232.

[51] H. Xie, Z. Cao, *Int. J. Quant. Chem.* **2007**, *107*, 1261.

[52] M. E. Harding, J. Vásquez, B. Ruscic, A. K. Wilson, J. Gauss, J. F. Stanton, *J. Chem. Phys.* **2008**, *128*, 114111.

[53] A. Karton, E. Rabinovich, J. M. Martin, B. Ruscic, *J. Chem. Phys.* **2006**, *125*, 144108.

[54] Y. Shao, C. Saravanan, M. H. Gordon, C. White, *J. Chem. Phys.* **2003**, *118*, 6144.

[55] P. Salek, S. Høst, L. Thøgersen, P. Jørgensen, P. Manninen, J. Olsen, B. Jansík, S. Reine, F. Pawłoski, E. Tellgren, T. Helgaker, S. Coriani, *J. Chem. Phys.* **2007**, *126*, 114110.

[56] S. Wang, H. F. Schaefer, *J. Chem. Phys.* **2006**, *124*, 044303.

[57] F. A. Evangelista, A. Paul, H. F. Schaefer, *J. Phys. Chem. A* **2004**, *108*, 3565.

[58] S. S. Wesolowski, M. L. Leininger, P. N. Pentchev, H. F. Schaefer, *J. Am. Chem. Soc.* **2001**, *123*, 4023.

[59] N. A. Richardson, S. S. Wesolowski, H. F. Schaefer, *J. Am. Chem. Soc.* **2002**, *124*, 10163.

[60] N. A. Richardson, S. S. Wesolowski, H. F. Schaefer, *J. Phys. Chem. B* **2003**, *107*, 848.

[61] N. A. Richardson, J. Gu, S. Wang, Y. Xie, H. F. Schaefer, *J. Am. Chem. Soc.* **2004**, *126*, 4404.

[62] A. D. Becke, *J. Chem. Phys.* **1993**, *98*, 5648.

[63] C. Lee, W. Yang, R. G. Parr, *Phys. Rev. B* **1988**, *37*, 785.

[64] T. J. Lee, H. F. Schaefer, *J. Chem. Phys.* **1985**, *83*, 1784.

[65] J. C. Rienstra-Kiracofe, G. S. Tschumper, H. F. Schaefer, S. Nandi, G. B. Ellison, *Chem. Rev.* **2002**, *102*, 231.

[66] A. E. Reed, F. Weinhold, *J. Chem. Phys.* **1983**, *78*, 4066.

[67] A. E. Reed, R. B. Weinstock, F. Weinhold, *J. Chem. Phys.* **1985**, *83*, 735.

[68] A. Szabo, N. S. Ostlund, *Modern Quantum Chemistry: Introduction To Advanced Electronic Structure Theory*, Dover: New York, **1998**.

[69] H. F. Schaefer, *Chem. Britain* **1975**, *11*, 227.

[70] K. Fukui, *Acc. Chem. Res.* **1981**, *14*, 363.

[71] M. W. Schmidt, M. S. Gordon, M. Dupuis, *J. Am. Chem. Soc.* **1985**, *107*, 2585.

[72] B. C. Garrett, J. Redmon, M, R. Steckler, D. G. Truhlar, K. K. Baldridge, D. Bartol, M. W. Schmidt, M. S. Gordon, *J. Phys. Chem.* **1988**, *92*, 1476.

[73] Y. Shao, L. Fusti-Molnar, Y. Jung, J. Kussmann, C. Ochsenfeld, S. T. Brown, A. T. B. Gilbert, L. V. Slipchenko, S. V. Levchenko, D. P. O'Neill, R. A. D. Jr., R. C. Lochan, T. Wang, G. J. O. Beran, N. A. Besley, J. M. Herbert, C. Y. Lin, T. V. Voorhis, S. H. Chien, A. Sodt, R. P. Steele, V. A. Rassolov, P. E. Maslen, P. P. Korambath, R. D. Adamson, B. Austin, J. Baker, E. F. C. Byrd, H. Dachsel, R. J. Doerksen, A. Dreuw, B. D. Dunietz, A. D. Dutoi, T. R. Furlani, S. R. Gwaltney, A. Heyden, S. Hirata, C. P. Hsu, G. Kedziora, R. Z. Khalliulin, P. Klunzinger, A. M. Lee, M. S. Lee, W. Liang, I. Lotan, N. Nair, B. Peters, E. I. Proynov, P. A. Pieniazek, Y. M. Rhee, J. Ritchie, E. Rosta, C. D. Sherrill, A. C. Simmonett, J. E. Subotnik, H. L. W. III, W. Zhang, A. T. Bell, A. K. Chakraborty, D. M. Chipman, F. J. Keil, A. Warshel, W. J. Hehre, H. F. Schaefer, J. Kong, A. I. Krylov, P. M. W. Gill, M. Head-Gordon, *Phys. Chem. Chem. Phys.* **2006**, *8*, 3172.

# Chapter 5

## Summary and Conclusions

Application of high levels of theory to small molecules is still of interest to both experimentalist and theorists. Detailed analysis of small molecules by means of improved computational and experimental methods can be very helpful for more complete understanding of the system. In addition, reference data such as energies and other properties for small model systems provides invaluable information for larger molecules and bulk systems.

Challenging problems related to the electronic structure of two open shell systems, $(H_2O)_2^+$ and BNNO have been systematically investigated by quantum mechanical *ab initio* methods such as SCF, CCSD, and CCSD(T). Corrections due to the zero point vibrational energy have been included, and large basis sets such as aug-cc-pVQZ have been employed.

Fourteen stationary points have been located on the water dimer radical cation electronic doublet ground state PES. For this open shell system, stationary point geometries and energetics are very sensitive to basis sets and levels of sophistication. However, with the highest level aug-cc-pVQZ CCSD(T) computations, the small energy difference, which is less than 1 kcal $mol^{-1}$, between isomer **1** and **2** is able to be predicted. The geometry of the $(H_2O)_2^+$ global minimum, isomer **1**, is very different from neutral water dimer due to loss of one electron and formation of a hydrogen bridge bond.

The isomerization reactions for BNNO have been characterized with various *ab initio* methods. The small reaction barrier is accurately predicted using high level computations. Fundamental vibrational frequencies, as well as isotopic shifts, were compared with experimental observations. This confirms that the second lowest lying *trans*-isomer is formed in the reaction of boron with nitrous oxide. In addition, physical and chemical properties such as bonding, equilibrium geometries, dipole moments, and infrared intensities have been studied, and reliable values have been determined with coupled cluster theories.

Finally, B3LYP method combined with DZP++ basis set efficiently elucidated the potential energy surfaces for dehydrogenation of adenine by hydroxyl radical. The corresponding reaction pathways and energetics should shed light on related biochemical experiments. Understanding the detailed reaction processes of small molecules and fragments of large biomolecules such as DNA, constitutes the most promising path towards solutions for DNA damage and other human diseases.

# APPENDIX A

## SUPPLEMENTARY MATERIAL FOR CHAPTER 3

Table A.1: Electron configurations of the cyclic, *trans*, *cis*, TS1 and TS2 BNNO molecule, and that of the linear NNO ($\tilde{X}\ ^1\Sigma^+$) molecule.

| Structure | Electron configuration |
|---|---|
| cyclic | [core]$(5a')^2(6a')^2(7a')^2(8a')^2(1a'')^2(9a')^2(10a')^2(11a')^2(2a'')^2(12a')^a$ |
| *trans* | [core]$(5a')^2(6a')^2(7a')^2(8a')^2(9a')^2(1a'')^2(10a')^2(2a'')^2(11a')^2(12a')^a$ |
| *cis* | [core]$(5a)^2(6a)^2(7a)^2(8a)^2(9a)^2(10a)^2(11a)^2(12a)^2(13a)^2(14a)^a$ |
| TS1 | [core]$(5a)^2(6a)^2(7a)^2(8a)^2(9a)^2(10a)^2(11a)^2(12a)^2(13a)^2(14a)^a$ |
| TS2 | [core]$(5a')^2(6a')^2(7a')^2(8a')^2(1a'')^2(9a')^2(10a')^2(2a'')^2(11a')^2(12a')^a$ |
| NNO | [core]$(4\sigma)^2(5\sigma)^2(6\sigma)^2(1\pi)^4(7\sigma)^2(2\pi)^{4\ b}$ |

[a][core] denotes the four lowest-lying core [B, N, O: 1s-like] orbitals.
[b][core] denotes the three lowest-lying core [N, O: 1s-like] orbitals.

Table A.2: Dominant CI coefficients of cc-pVQZ CASSCF wave function for five stationary points of BNNO molecule predicted at the cc-pVQZ UCCSD(T) geometries. [...] denotes the eight lowest-lying orbitals.

| Structure | Wavefunction | CI coefficients |
|---|---|---|
| cyclic | $[\ldots](9a')^2(10a')^2(11a')^2(12a')^1(1a'')^2(2a'')^2$ | $C_1 = 0.930$ |
| | $[\ldots](9a')^2(10a')^2(11a')^2(12a')^1(1a'')^2(2a'')^0(3a'')^2$ | $C_2 = -0.137$ |
| | $[\ldots](9a')^2(10a')^2(11a')^2(12a')^1(1a'')^0(2a'')^2(3a'')^2$ | $C_3 = -0.070$ |
| | $[\ldots](9a')^2(10a')^2(11a')^0(12a')^1(13a')^2(1a'')^2(2a'')^2$ | $C_4 = -0.060$ |
| *trans* | $[\ldots](9a')^2(10a')^2(11a')^2(12a')^1(1a'')^2(2a'')^2$ | $C_1 = 0.927$ |
| | $[\ldots](9a')^2(10a')^2(11a')^2(12a')^1(1a'')^2(2a'')^0(3a'')^2$ | $C_2 = -0.155$ |
| | $[\ldots](9a')^2(10a')^2(11a')^0(12a')^1(13a')^2(1a'')^2(2a'')^2$ | $C_3 = -0.101$ |
| | $[\ldots](9a')^2(10a')^2(11a')^2(12a')^1(1a'')^0(2a'')^2(4a'')^2$ | $C_4 = -0.071$ |
| *cis* | $[\ldots](9a)^2(10a)^2(11a)^2(12a)^2(13a)^2(14a)^1$ | $C_1 = 0.912$ |
| | $[\ldots](9a)^2(10a)^2(11a)^2(12a)^2(13a)^0(14a)^1(15a)^2$ | $C_2 = -0.102$ |
| | $[\ldots](9a)^2(10a)^2(11a)^2(12a)^1(13a)^1(14a)^2(15a)^1$ | $C_3 = -0.071$ |
| | $[\ldots](9a)^2(10a)^2(11a)^2(12a)^0(13a)^2(14a)^1(16a)^2$ | $C_4 = -0.074$ |
| TS1 | $[\ldots](9a)^2(10a)^2(11a)^2(12a)^2(13a)^2(14a)^1$ | $C_1 = 0.912$ |
| | $[\ldots](9a)^2(10a)^2(11a)^2(12a)^2(13a)^0(14a)^1(15a)^2$ | $C_2 = -0.099$ |
| | $[\ldots](9a)^2(10a)^2(11a)^2(12a)^0(13a)^1(14a)^2(16a)^2$ | $C_3 = -0.083$ |
| | $[\ldots](9a)^2(10a)^2(11a)^1(12a)^2(13a)^1(14a)^2(15a)^1$ | $C_4 = 0.074$ |
| TS2 | $[\ldots](9a')^2(10a')^2(11a')^2(12a')^1(1a'')^2(2a'')^2$ | $C_1 = 0.914$ |
| | $[\ldots](9a')^2(10a')^2(11a')^2(12a')^1(1a'')^2(2a'')^0(3a'')^2$ | $C_2 = -0.109$ |
| | $[\ldots](9a')^2(10a')^2(11a')^1(12a')^1(13a')^1(1a'')^2(2a'')^2$ | $C_3 = -0.107$ |
| | $[\ldots](9a')^2(10a')^2(11a')^0(12a')^1(13a')^2(1a'')^2(2a'')^2$ | $C_4 = -0.106$ |

Table A.3: Optimized geometries (Å and degrees) for five stationary points of BNNO ($\tilde{X}\ ^2A'$), BN ($X\ ^3\Pi$), NO ($X\ ^2\Sigma^+$), and NNO ($\tilde{X}\ ^1\Sigma^+$) predicted at the aug-cc-pVQZ CCSD(T) level of theory [geometries at the cc-pVQZ CCSD(T) level of theory are in parentheses[a]]. $\tau$(BNNO) for the *cis* BNNO isomer is 38.8° and $\tau$ for TS1 is 80.4°.

| | Structure | $r_e$(ON) | $r_e$(NN) | $r_e$(BN) | $r_e$(NB) | $\theta_e$(NNO) | $\theta_e$(BNN) | $\theta_e$(NBN) | $\theta_e$(BNN) |
|---|---|---|---|---|---|---|---|---|---|
| cyclic | 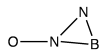 | 1.201 | 1.351 | 1.417 | 1.437 | 133.0 | 62.5 | 56.5 | 61.0 |
| | | (1.199) | (1.352) | (1.415) | (1.436) | (133.0) | (62.5) | (56.6) | ((60.9) |
| *trans* | 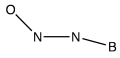 | 1.199 | 1.373 | 1.257 | | 113.7 | 164.0 | | |
| | | (1.198) | (1.375) | (1.256) | | (113.7) | (164.0) | | |
| *cis* | 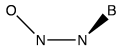 | 1.197 | 1.240 | 1.405 | | 134.7 | 137.4 | | |
| | | (1.196) | (1.240) | (1.404) | | (134.8) | (137.9) | | |
| TS1 | 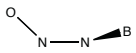 | – | – | – | | – | – | | |
| | | (1.195) | (1.235) | (1.397) | | (135.0) | (144.4) | | |
| TS2 | 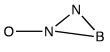 | 1.181 | 1.284 | 1.437 | 1.839 | 135.7 | 84.9 | 44.0 | 51.1 |
| | | (1.180) | (1.284) | (1.436) | (1.837) | (135.7) | (84.8) | (44.1) | (51.1) |
| BN | | | | 1.330 | | | | | |
| NO | | 1.153 | | | | | | | |
| NNO | | 1.188 | 1.129 | | | 180.0 | | | |

[a] TS1 is only shown at the cc-pVQZ CCSD(T) level of theory, without the augmenting diffuse functions. See text for details.

Table A.4: BNNO ($\tilde{X}\ ^2A'$) $\rightarrow$ B ($^2P_u$) + NNO ($\tilde{X}\ ^1\Sigma^+$) dissociation energies (in kcal mol$^{-1}$, ZPVE corrected values in parentheses) at the SCF, CCSD, and CCSD(T) levels of theory with the four basis sets.

| Level of theory | cyclic | *trans* | *cis* |
|---|---|---|---|
| cc-pVTZ SCF | 29.53 (27.50) | 33.26 (32.07) | 11.76 (11.17) |
| aug-cc-pVTZ SCF | 30.17 (28.14) | 33.49 (32.30) | 11.68 (11.10) |
| cc-pVQZ SCF | 30.33 (28.28) | 33.89 (32.69) | 11.93 (11.33) |
| aug-cc-pVQZ SCF | 30.50 (28.45) | 33.95 (32.75) | 11.91 (11.32) |
| cc-pVTZ CCSD | 35.44 (33.68) | 34.33 (33.54) | 22.22 (22.30) |
| aug-cc-pVTZ CCSD | 36.66 (34.89) | 35.15 (34.33) | 22.68 (22.78) |
| cc-pVQZ CCSD | 37.83 (36.03) | 36.36 (35.52) | 23.33 (23.42) |
| aug-cc-pVQZ CCSD | 38.27 (36.17) | 36.77 (35.60) | 23.58 (23.35) |
| cc-pVTZ CCSD(T) | 38.33 (36.74) | 35.14 (34.95) | 25.64 (25.44) |
| aug-cc-pVTZ CCSD(T) | 39.58 (37.97) | 36.11 (35.67) | 26.27 (26.09) |
| cc-pVQZ CCSD(T) | 40.80 (39.16) | 37.32 (36.86) | 26.97 (26.68) |
| aug-cc-pVQZ CCSD(T) | 41.27 (39.65) | 37.81 (37.33) | 27.30 (27.02) |

Table A.5: BNNO ($\tilde{X}\ ^2A'$) $\rightarrow$ BN ($X\ ^3\Pi$) + NO ($X\ ^2\Sigma^+$) dissociation energies (in kcal mol$^{-1}$, ZPVE corrected values in parentheses) at the SCF, CCSD, and CCSD(T) levels of theory with the four basis sets.

| Level of theory | cyclic | *trans* | *cis* |
|---|---|---|---|
| cc-pVTZ SCF | 17.12 (13.10) | 20.85 (17.67) | $-0.65$ ($-3.23$) |
| aug-cc-pVTZ SCF | 17.52 (13.50) | 20.84 (17.66) | $-0.97$ ($-3.54$) |
| cc-pVQZ SCF | 17.47 (13.44) | 21.03 (17.85) | $-0.93$ ($-3.50$) |
| aug-cc-pVQZ SCF | 17.58 (13.55) | 21.03 (17.86) | $-1.00$ ($-3.57$) |
| cc-pVTZ CCSD | 45.69 (41.95) | 44.58 (41.81) | 32.47 (30.57) |
| aug-cc-pVTZ CCSD | 46.78 (43.06) | 45.27 (42.50) | 32.80 (30.96) |
| cc-pVQZ CCSD | 47.91 (44.15) | 46.44 (43.64) | 33.41 (31.54) |
| aug-cc-pVQZ CCSD | 48.34 (44.61) | 46.84 (44.04) | 33.65 (31.79) |
| cc-pVTZ CCSD(T) | 51.39 (47.83) | 48.20 (46.04) | 38.70 (36.54) |
| aug-cc-pVTZ CCSD(T) | 52.54 (48.99) | 49.07 (46.69) | 39.23 (37.12) |
| cc-pVQZ CCSD(T) | 53.75 (50.17) | 50.27 (47.87) | 39.93 (37.69) |
| aug-cc-pVQZ CCSD(T) | 54.22 (50.67) | 50.75 (48.35) | 40.25 (38.04) |

Table A.6: Theoretical predictions of the total energy (in hartree), dipole moment[a] ($\mu_e$, in Debye), harmonic vibrational frequencies ($\omega$, in cm$^{-1}$), infrared intensities[a] (in km mol$^{-1}$, in parentheses) and zero-point vibrational energy (ZPVE in kcal mol$^{-1}$) for the $^2A'$ cyclic-$^{11}$B$^{14}$N$^{14}$NO molecule.

| Level of theory | Total energy | $\mu_e$ | $\omega_1(a')$ | $\omega_2(a')$ | $\omega_3(a')$ | $\omega_4(a')$ | $\omega_5(a')$ | $\omega_6(a'')$ | ZPVE |
|---|---|---|---|---|---|---|---|---|---|
| cc-pVDZ SCF | -208.270405 | 2.81 | 1883 (496) | 1532 (58) | 1264 (245) | 987 (8) | 581 (12) | 607 (8) | 9.80 |
| cc-pVTZ SCF | -208.331384 | 2.90 | 1861 (515) | 1528 (60) | 1265 (284) | 995 (8) | 592 (13) | 615 (6) | 9.80 |
| cc-pVQZ SCF | -208.347303 | 2.94 | 1853 (528) | 1528 (57) | 1268 (297) | 997 (8) | 594 (13) | 615 (14) | 9.80 |
| aug-cc-pVDZ SCF | -208.286544 | 3.05 | 1846 (540) | 1518 (47) | 1268 (292) | 984 (6) | 576 (13) | 603 (5) | 9.72 |
| aug-cc-pVTZ SCF | -208.334767 | 2.99 | 1847 (533) | 1523 (57) | 1265 (305) | 995 (7) | 592 (13) | 614 (6) | 9.77 |
| aug-cc-pVQZ SCF | -208.348276 | 2.98 | 1850 (536) | 1527 (56) | 1268 (304) | 997 (8) | 594 (13) | 614 (14) | 9.79 |
| cc-pVDZ CCSD | -208.843696 | 1.72 | 1781 (336) | 1342 (44) | 1047 (87) | 872 (20) | 523 (5) | 520 (4) | 8.70 |
| cc-pVTZ CCSD | -209.025495 | 1.97 | 1771 (382) | 1363 (53) | 1075 (118) | 894 (17) | 537 (6) | 537 (4) | 8.83 |
| cc-pVQZ CCSD | -209.083626 | – | 1772 (–) | 1371 (–) | 1092 (–) | 905 (–) | 542 (–) | 539 (–) | 8.89 |
| aug-cc-pVDZ CCSD | -208.882161 | 2.15 | 1726 (401) | 1319 (44) | 1056 (123) | 870 (18) | 514 (6) | 513 (3) | 8.57 |
| aug-cc-pVTZ CCSD | -209.039679 | 2.15 | 1752 (412) | 1356 (51) | 1079 (136) | 895 (15) | 535 (6) | 534 (3) | 8.79 |
| aug-cc-pVQZ CCSD | -209.089133 | – | 1763 (–) | 1364 (–) | 1088 (–) | 903 (–) | 540 (–) | 537 (–) | 8.86 |
| cc-pVDZ CCSD(T) | -208.873036 | 1.47 | 1730 (277) | 1277 (31) | 974 (53) | 828 (22) | 502 (4) | 500 (4) | 8.31 |
| cc-pVTZ CCSD(T) | -209.066925 | 1.70 | 1721 (305) | 1300 (42) | 999 (74) | 848 (22) | 516 (5) | 513 (3) | 8.43 |
| cc-pVQZ CCSD(T) | -209.128075 | – | 1722 (–) | 1307 (–) | 1015 (–) | 860 (–) | 520 (–) | 514 (–) | 8.49 |
| aug-cc-pVDZ CCSD(T) | -208.915054 | 1.91 | 1676 (331) | 1252 (35) | 981 (78) | 827 (20) | 492 (5) | 490 (3) | 8.17 |
| aug-cc-pVTZ CCSD(T) | -209.082567 | 1.90 | 1701 (327) | 1291 (44) | 1003 (87) | 850 (21) | 513 (5) | 509 (3) | 8.39 |
| aug-cc-pVQZ CCSD(T) | -209.134170 | – | 1712 (–) | 1298 (–) | 1013 (–) | 859 (–) | 517 (–) | 511 (–) | 8.45 |

[a] Dipole moment and IR intensities are determined using ACESII program.

Table A.7: Theoretical predictions of the total energy (in hartree), dipole moment[a] ($\mu_e$, in Debye), harmonic vibrational frequencies ($\omega$, in cm$^{-1}$), infrared intensities[a] (in km mol$^{-1}$, in parentheses) and zero-point vibrational energy (ZPVE in kcal mol$^{-1}$) for the $^2A'$ *trans*-$^{11}$B$^{14}$N$^{14}$NO molecule.

| Level of theory | Total energy | $\mu_e$ | $\omega_1(a')$ | $\omega_2(a')$ | $\omega_3(a')$ | $\omega_4(a')$ | $\omega_5(a')$ | $\omega_6(a'')$ | ZPVE |
|---|---|---|---|---|---|---|---|---|---|
| cc-pVDZ SCF | -208.279090 | 2.88 | 2137(363) | 1917 (442) | 1053 (186) | 774 (12) | 196 (9) | 189 (12) | 8.96 |
| cc-pVTZ SCF | -208.337383 | 3.00 | 2135 (388) | 1886 (423) | 1048 (186) | 778 (12) | 209 (10) | 211 (13) | 8.96 |
| cc-pVQZ SCF | -208.353025 | 3.06 | 2134 (398) | 1881 (432) | 1049 (184) | 779 (12) | 208 (11) | 207 (13) | 8.95 |
| aug-cc-pVDZ SCF | -208.293389 | 3.13 | 2122 (409) | 1883 (454) | 1057 (180) | 775 (10) | 193 (12) | 193 (14) | 8.90 |
| aug-cc-pVTZ SCF | -208.340111 | 3.11 | 2130 (412) | 1873 (437) | 1048 (185) | 778 (11) | 209 (11) | 210 (14) | 8.93 |
| aug-cc-pVQZ SCF | -208.353828 | 3.09 | 2132 (408) | 1878 (438) | 1050 (184) | 780 (11) | 208 (11) | 206 (13) | 8.94 |
| cc-pVDZ CCSD | -208.847043 | 1.73 | 1931 (157) | 1649 (294) | 890 (184) | 647 (50) | 151 (4) | 136 (5) | 7.53 |
| cc-pVTZ CCSD | -209.023721 | 2.12 | 1950 (68) | 1637 (533) | 909 (178) | 671 (34) | 167 (5) | 159 (7) | 7.87 |
| cc-pVQZ CCSD | -209.081263 | 2.28 | 1961 (74) | 1643 (758) | 922 (175) | 683 (28) | 168 (5) | 161 (–) | 7.94 |
| aug-cc-pVDZ CCSD | -208.884434 | 2.26 | 1909 (202) | 1610 (330) | 897 (183) | 658 (36) | 150 (6) | 136 (7) | 7.47 |
| aug-cc-pVTZ CCSD | -209.037250 | 2.34 | 1942 (86) | 1621 (560) | 913 (178) | 675 (30) | 170 (6) | 158 (7) | 7.84 |
| aug-cc-pVQZ CCSD | -209.086715 | – | 1957 (–) | 1638 (–) | 923 (–) | 684 (–) | 170 (–) | 157 (–) | 7.92 |
| cc-pVDZ CCSD(T) | -208.872958 | 1.73 | 1845 (148) | 1572 (290) | 841 (170) | 600 (74) | 137 (4) | 112 (6) | 6.94 |
| cc-pVTZ CCSD(T) | -209.061792 | 2.01 | 1870 (162) | 1547 (313) | 861 (168) | 631 (51) | 147 (4) | 133 (6) | 7.03 |
| cc-pVQZ CCSD(T) | -209.122477 | 2.19 | 1881 (161) | 1551 (356) | 874 (169) | 644 (42) | 151 (5) | 138 (–) | 7.31 |
| aug-cc-pVDZ CCSD(T) | -208.914269 | 2.20 | 1819 (194) | 1523 (323) | 846 (173) | 616 (54) | 139 (6) | 114 (8) | 6.87 |
| aug-cc-pVTZ CCSD(T) | -209.076985 | 2.27 | 1859 (188) | 1527 (330) | 864 (171) | 637 (44) | 152 (6) | 137 (–) | 7.22 |
| aug-cc-pVQZ CCSD(T) | -209.128591 | – | 1876 (–) | 1544 (–) | 874 (–) | 646 (–) | 149 (–) | 137 (–) | 7.30 |

[a] Dipole moment and IR intensities are determined using ACESII program.

Table A.8: Theoretical predictions of the total energy (in hartree), dipole moment[a] ($\mu_e$, in Debye), harmonic vibrational frequencies ($\omega$, in cm$^{-1}$), infrared intensities[a] (in km mol$^{-1}$, in parentheses) and zero-point vibrational energy (ZPVE in kcal mol$^{-1}$) for the $^2A$ *cis*-$^{11}$B$^{14}$N$^{14}$NO molecule.

| Level of theory | Total energy | $\mu_e$ | $\omega_1$ | $\omega_2$ | $\omega_3$ | $\omega_4$ | $\omega_5$ | $\omega_6$ | ZPVE |
|---|---|---|---|---|---|---|---|---|---|
| cc-pVDZ SCF | -208.246002 | 1.80 | 1911 (1268) | 1612 (259) | 1055 (277) | 787 (20) | 325 (6) | 204 (1) | 8.43 |
| cc-pVTZ SCF | -208.302790 | 1.91 | 1882 (1415) | 1620 (302) | 1062 (264) | 789 (28) | 309 (6) | 185 (1) | 8.36 |
| cc-pVQZ SCF | -208.317693 | 1.91 | 1873 (1422) | 1618 (325) | 1060 (271) | 792 (27) | 305 (6) | 187 (1) | 8.34 |
| aug-cc-pVDZ SCF | -208.258921 | 1.73 | 1870 (1331) | 1589 (279) | 1043 (305) | 784 (15) | 325 (5) | 211 (1) | 8.32 |
| aug-cc-pVTZ SCF | -208.305015 | 1.86 | 1867 (1440) | 1613 (312) | 1057 (280) | 789 (25) | 307 (5) | 186 (1) | 8.32 |
| aug-cc-pVQZ SCF | -208.318375 | 1.90 | 1871 (1434) | 1617 (329) | 1059 (276) | 792 (26) | 303 (5) | 187 (1) | 8.33 |
| cc-pVDZ CCSD | -208.847043 | 1.31 | 1931 (762) | 1649 (84) | 890 (201) | 647 (9) | 151 (5) | 136 (1) | 7.53 |
| cc-pVTZ CCSD | -209.023721 | 1.34 | 1958 (913) | 1637 (78) | 909 (199) | 673 (11) | 167 (5) | 160 (1) | 7.87 |
| cc-pVQZ CCSD | -209.081263 | – | 1970 (934) | 1643 (78) | 923 (208) | 684 (10) | 170 (5) | 161 (–) | 7.94 |
| aug-cc-pVDZ CCSD | -208.884434 | 0.97 | 1909 (874) | 1610 (67) | 897 (238) | 658 (5) | 150 (5) | 136 (1) | 7.47 |
| aug-cc-pVTZ CCSD | -209.037250 | 1.16 | 1950 (955) | 1621 (70) | 912 (219) | 677 (8) | 169 (5) | 158 (1) | 7.84 |
| aug-cc-pVQZ CCSD | -209.086715 | – | 1965 (–) | 1638 (–) | 924 (–) | 685 (–) | 171 (–) | 158 (–) | 7.92 |
| cc-pVDZ CCSD(T) | -208.858715 | 1.29 | 1693 (708) | 1399 (35) | 1021 (169) | 726 (4) | 189 (5) | 81 (1) | 7.19 |
| cc-pVTZ CCSD(T) | -209.046507 | – | 1653 (808) | 1388 (23) | 1013 (156) | 682 (9) | 183 (5) | 78 (1) | 7.03 |
| cc-pVQZ CCSD(T) | -209.105827 | – | 1650 (808) | 1378 (21) | 1013 (160) | 681 (8) | 187 (4) | 90 (–) | 7.14 |
| aug-cc-pVDZ CCSD(T) | -208.899517 | 0.90 | 1632 (786) | 1353 (22) | 997 (205) | 724 (2) | 192 (4) | 89 (1) | 7.00 |
| aug-cc-pVTZ CCSD(T) | -209.061153 | – | 1628 (814) | 1362 (17) | 1006 (176) | 676 (7) | 191 (4) | 83 (1) | 6.95 |
| aug-cc-pVQZ CCSD(T) | -209.111697 | – | 1641 (–) | 1368 (–) | 1011 (–) | 679 (–) | 189 (–) | 85 (–) | 7.11 |

[a] Dipole moment and IR intensities are determined using ACESII program.

Table A.9: Theoretical predictions of the total energy (in hartree), dipole moment[a] ($\mu_e$, in Debye), harmonic vibrational frequencies ($\omega$, in $cm^{-1}$), infrared intensities[a] (in km $mol^{-1}$, in parentheses) and zero-point vibrational energy (ZPVE in kcal $mol^{-1}$) for the *trans−cis* transition state (TS1) of $^{11}B^{14}N^{14}NO$.

| Level of theory | Total energy | $\mu_e$ | $\omega_1$ | $\omega_2$ | $\omega_3$ | $\omega_4$ | $\omega_5$ | $\omega_6$ | ZPVE |
|---|---|---|---|---|---|---|---|---|---|
| cc-pVDZ SCF | -208.242168 | 2.18 | 1971 (1835) | 1730 (238) | 1065 (217) | 740 (46) | 150 (1) | 231$i$ (–) | 8.09 |
| cc-pVTZ SCF | -208.300307 | 2.27 | 1950 (2125) | 1737 (147) | 1063 (212) | 742 (53) | 109 (1) | 199$i$ (–) | 7.85 |
| cc-pVQZ SCF | -208.315257 | 2.26 | 1932 (–) | 1730 (–) | 1066 (–) | 747 (–) | 129 (–) | 204$i$ (–) | 7.83 |
| aug-cc-pVDZ SCF | -208.254859 | 2.12 | 1923 (1864) | 1693 (344) | 1061 (258) | 741 (37) | 185 (1) | 242$i$ (–) | 8.01 |
| aug-cc-pVTZ SCF | -208.302551 | 2.21 | 1932 (2176) | 1728 (162) | 1060 (231) | 743 (51) | 118 (1) | 201$i$ (–) | 7.81 |
| aug-cc-pVQZ SCF | -208.315955 | 2.25 | 1929 (–) | 1728 (–) | 1066 (–) | 747 (–) | 131 (–) | 204$i$ (–) | 7.82 |
| cc-pVDZ CCSD | -208.827615 | 2.00 | 1765 (1167) | 1496 (107) | 1010 (192) | 673 (33) | 199 (1) | 139$i$ (–) | 7.35 |
| cc-pVTZ CCSD | -209.003510 | – | 1759 (–) | 1512 (–) | 1007 (–) | 683 (–) | 178 (–) | 121$i$ (–) | 7.35 |
| cc-pVQZ CCSD | -209.059582 | – | 1760 (–) | 1514 (–) | 1011 (–) | 687 (–) | 189 (–) | 123$i$ (–) | 7.38 |
| aug-cc-pVDZ CCSD | -208.864107 | 1.69 | 1711 (1380) | 1455 (106) | 989 (256) | 668(32) | 217(1) | 147$i$ (–) | 7.21 |
| aug-cc-pVTZ CCSD | -209.016416 | – | 1740 (–) | 1496 (–) | 999 (–) | 680 (–) | 188 (–) | 122$i$ (–) | 7.30 |
| aug-cc-pVQZ CCSD | -209.064753 | – | – | – | – | – | – | – | – |
| cc-pVDZ CCSD(T) | -208.858337 | 1.92 | 1687 (922) | 1414 (56) | 993 (186) | 643 (24) | 215 (1) | 115$i$ (–) | 7.08 |
| cc-pVTZ CCSD(T) | -209.046346 | – | 1674 (–) | 1423 (–) | 990 (–) | 649 (–) | 200 (–) | 96$i$ (–) | 7.06 |
| cc-pVQZ CCSD(T) | -209.105629 | – | 1675 (–) | 1420 (–) | 990 (–) | 651 (–) | 204 (–) | 100$i$ (–) | 7.06 |
| aug-cc-pVDZ CCSD(T) | -208.898885 | 1.57 | 1635 (1076) | 1368 (51) | 981 (248) | 637 (23) | 228 (1) | 134$i$ (–) | 6.93 |
| aug-cc-pVTZ CCSD(T) | -209.060945 | – | 1654 (–) | 1402 (–) | 978 (–) | 643 (–) | 205 (–) | 100$i$ (–) | 6.98 |
| aug-cc-pVQZ CCSD(T) | -209.111462 | – | – | – | – | – | – | – | – |

[a] Dipole moment and IR intensities are determined using ACESII program.

Table A.10: Theoretical predictions of the total energy (in hartree), dipole moment[a] ($\mu_e$, in Debye), harmonic vibrational frequencies ($\omega$, in cm$^{-1}$), infrared intensities[a] (in km mol$^{-1}$, in parentheses) and zero-point vibrational energy (ZPVE in kcal mol$^{-1}$) for the $^2A'$ cyclic$-$*trans* transition state (TS2) of $^{11}$B$^{14}$N$^{14}$NO.

| Level of theory | Total energy | $\mu_e$ | $\omega_1(a')$ | $\omega_2(a')$ | $\omega_3(a')$ | $\omega_4(a')$ | $\omega_5(a')$ | $\omega_6(a'')$ | ZPVE |
|---|---|---|---|---|---|---|---|---|---|
| cc-pVDZ SCF | -208.244012 | 3.83 | 1906 (250) | 1674 (103) | 1017 (310) | 479 (0) | 275 (1) | 771$i$ (–) | 8.07 |
| cc-pVTZ SCF | -208.302008 | 3.94 | 1873 (257) | 1676 (123) | 1011 (345) | 480 (0) | 271 (2) | 772$i$ (–) | 8.01 |
| cc-pVQZ SCF | -208.317805 | 3.99 | 1867 (260) | 1676 (126) | 1016 (354) | 481 (0) | 272 (38) | 774$i$ (–) | 8.01 |
| aug-cc-pVDZ SCF | -208.260535 | 4.10 | 1863 (272) | 1652 (112) | 1042 (354) | 473 (1) | 283 (2) | 771$i$ (–) | 8.02 |
| aug-cc-pVTZ SCF | -208.305308 | 4.06 | 1859 (263) | 1670 (128) | 1013 (362) | 479 (1) | 272 (2) | 772$i$ (–) | 7.99 |
| aug-cc-pVQZ SCF | -208.318735 | 4.04 | 1863 (263) | 1674 (128) | 1018 (361) | 481 (1) | 271 (44) | 774$i$ (–) | 8.01 |
| cc-pVDZ CCSD | -208.817980 | 0.77 | 1746 (353) | 1240 (81) | 985 (8) | 423 (49) | 390 (7) | 726$i$ (–) | 6.84 |
| cc-pVTZ CCSD | -208.995154 | 0.78 | 1749 (401) | 1252 (89) | 1018 (14) | 439 (47) | 389 (7) | 693$i$ (–) | 6.93 |
| cc-pVQZ CCSD | -209.051421 | – | 1758 (–) | 1262 (–) | 1031 (–) | 441 (–) | 385 (–) | 709$i$ (–) | 6.97 |
| aug-cc-pVDZ CCSD | -208.855509 | 0.43 | 1716 (459) | 1225 (97) | 978 (9) | 416 (56) | 383 (6) | 734$i$ (–) | 6.75 |
| aug-cc-pVTZ CCSD | -209.008512 | 0.64 | 1741 (438) | 1248 (94) | 1016 (16) | 436 (47) | 386 (7) | 705$i$ (–) | 6.90 |
| aug-cc-pVQZ CCSD | -209.056654 | – | 1755 (–) | 1257 (–) | 1028 (–) | 439 (–) | 382 (–) | 711$i$ (–) | 6.95 |
| cc-pVDZ CCSD(T) | -208.848082 | 0.91 | 1800 (424) | 1196 (77) | 967 (15) | 400 (41) | 360 (7) | 719$i$ (–) | 6.75 |
| cc-pVTZ CCSD(T) | -209.037465 | 0.90 | 1866 (477) | 1230 (86) | 997 (26) | 434 (40) | 356 (7) | 673$i$ (–) | 6.98 |
| cc-pVQZ CCSD(T) | -209.096883 | – | 1867 (–) | 1240 (–) | 1009 (–) | 437 (–) | 352 (–) | 688$i$ (–) | 7.01 |
| aug-cc-pVDZ CCSD(T) | -208.889538 | 0.55 | 1763 (521) | 1172 (91) | 950 (16) | 383 (46) | 352 (5) | 756$i$ (–) | 6.60 |
| aug-cc-pVTZ CCSD(T) | -209.052332 | 0.74 | 1860 (514) | 1224 (91) | 994 (27) | 429 (40) | 353 (6) | 689$i$ (–) | 6.95 |
| aug-cc-pVQZ CCSD(T) | -209.102719 | – | 1866 (–) | 1234 (–) | 1005 (–) | 431 (–) | 348 (–) | 691$i$ (–) | 6.98 |

[a] Dipole moment and IR intensities are determined using ACESII program.

Table A.11: Experimentally observed and computed frequencies (in $cm^{-1}$) of the BNNO for the $^2A'$*trans*and $^2A'$cyclic-BNNO at the cc-pVTZ CCSD(T) level of theory.

| Mode (Sym.) | Intensity[a] | Obs.[a] | | |
|---|---|---|---|---|
| | | $^{10}B^{14}N^{14}NO$ | $^{11}B^{14}N^{14}NO$ | $^{10}B^{15}N^{15}NO$ |
| B-N stretch | 96 | 1837 | 1796 | 1808 |
| N-O stretch | 447 | 1502 | 1500 | 1476 |
| N-N stretch | 127 | 838 | 837 | 815 |
| Bending | 38 | 634 | 627 | 625 |

| *trans*-BNNO | Intensity[b] | $\omega^c$ | | | $\nu^c$ | | |
|---|---|---|---|---|---|---|---|
| | | $^{10}B^{14}N^{14}NO$ | $^{11}B^{14}N^{14}NO$ | $^{10}B^{15}N^{15}NO$ | $^{10}B^{14}N^{14}NO$ | $^{11}B^{14}N^{14}NO$ | $^{10}B^{15}N^{15}NO$ |
| B-N stretch | 162 | 1922 | 1880 | 1891 | 1873 | 1832 | 1843 |
| N-O stretch | 313 | 1552 | 1550 | 1525 | 1530 | 1528 | 1503 |
| N-N stretch | 168 | 866 | 864 | 842 | 832 | 831 | 810 |
| Bending | 51 | 645 | 637 | 635 | 619 | 611 | 609 |

| cyclic-BNNO | Intensity[b] | $\omega^c$ | | | $\nu^c$ | | |
|---|---|---|---|---|---|---|---|
| | | $^{10}B^{14}N^{14}NO$ | $^{11}B^{14}N^{14}NO$ | $^{10}B^{15}N^{15}NO$ | $^{10}B^{14}N^{14}NO$ | $^{11}B^{14}N^{14}NO$ | $^{10}B^{15}N^{15}NO$ |
| B-N stretch | 42 | 1330 | 1303 | 1311 | 1305 | 1277 | 1286 |
| N-O stretch | 305 | 1734 | 1728 | 1697 | 1684 | 1699 | 1650 |
| N-N stretch | 22 | 1018 | 1001 | 1000 | 982 | 964 | 966 |
| Bending | 74 | 859 | 851 | 842 | 830 | 824 | 814 |

[a] Ref.[1].
[b] cc-pVTZ CCSD(T) (with UHF reference) level from our research (in km $mol^{-1}$).
[c] cc-pCVTZ CCSD(T) (with ROHF reference) level from our research.

Table A.12: Experimentally observed and computed frequencies (in $cm^{-1}$) of the BNNO for the $^2A'$*trans*and $^2A'$cyclic-BNNO at the cc-pCVTZ CCSD(T) level of theory.

| Mode (Sym.) | Intensity[a] | Obs.[a] | | |
|---|---|---|---|---|
| | | $^{10}B^{14}N^{14}NO$ | $^{11}B^{14}N^{14}NO$ | $^{10}B^{15}N^{15}NO$ |
| B-N stretch | 96 | 1837 | 1796 | 1808 |
| N-O stretch | 447 | 1502 | 1500 | 1476 |
| N-N stretch | 127 | 838 | 837 | 815 |
| Bending | 38 | 634 | 627 | 625 |

| *trans*-BNNO | Intensity[b] | $\omega^c$ | | | $\nu^c$ | | |
|---|---|---|---|---|---|---|---|
| | | $^{10}B^{14}N^{14}NO$ | $^{11}B^{14}N^{14}NO$ | $^{10}B^{15}N^{15}NO$ | $^{10}B^{14}N^{14}NO$ | $^{11}B^{14}N^{14}NO$ | $^{10}B^{15}N^{15}NO$ |
| B-N stretch | 162 | 1912 | 1869 | 1880 | 1862 | 1821 | 1832 |
| N-O stretch | 313 | 1549 | 1547 | 1523 | 1527 | 1525 | 1500 |
| N-N stretch | 168 | 861 | 860 | 837 | 828 | 827 | 806 |
| Bending | 51 | 638 | 630 | 628 | 612 | 605 | 603 |

| cyclic-BNNO | Intensity[b] | $\omega^c$ | | | $\nu^c$ | | |
|---|---|---|---|---|---|---|---|
| | | $^{10}B^{14}N^{14}NO$ | $^{11}B^{14}N^{14}NO$ | $^{10}B^{15}N^{15}NO$ | $^{10}B^{14}N^{14}NO$ | $^{11}B^{14}N^{14}NO$ | $^{10}B^{15}N^{15}NO$ |
| B-N stretch | 42 | 1322 | 1295 | 1302 | 1297 | 1269 | 1278 |
| N-O stretch | 305 | 1727 | 1721 | 1690 | 1677 | 1690 | 1643 |
| N-N stretch | 22 | 1013 | 996 | 994 | 977 | 959 | 961 |
| Bending | 74 | 854 | 846 | 837 | 825 | 819 | 809 |

[a] Ref.[1].
[b] cc-pVTZ CCSD(T) (with UHF reference) level from our research (in km $mol^{-1}$).
[c] cc-pVTZ CCSD(T) (with ROHF reference) level from our research.

Table A.13: Fundamental vibrational frequencies (in $cm^{-1}$) for the BNNO molecule and the corresponding shifts ($\Delta$) upon isotopic substitution at the cc-pVTZ CCSD(T) level of theory. The experimental results for the lowest lying isomer are shown for comparison purposes.

| Mode (Sym.) | $\nu_{^{10}B^{14}N^{14}NO}$ | $\Delta(\nu_{^{11}B^{14}N^{14}NO})$ | $\Delta(\nu_{^{10}B^{15}N^{15}NO})$ |
|---|---|---|---|
| Exp.[a] | | | |
| B-N stretch | 1837 | 41 | 28 |
| N-O stretch | 1502 | 2 | 26 |
| N-N stretch | 838 | 1 | 23 |
| Bending | 634 | 7 | 9 |
| *trans*-BNNO | | | |
| B-N stretch | 1862 | 43 | 32 |
| N-O stretch | 1527 | 2 | 26 |
| N-N stretch | 828 | 1 | 24 |
| Bending | 612 | 8 | 10 |
| cyclic-BNNO | | | |
| B-N stretch | 1297 | 27 | 20 |
| N-O stretch | 1677 | 6 | 37 |
| N-N stretch | 977 | 17 | 19 |
| Bending | 825 | 8 | 17 |

[a] Ref.[1].

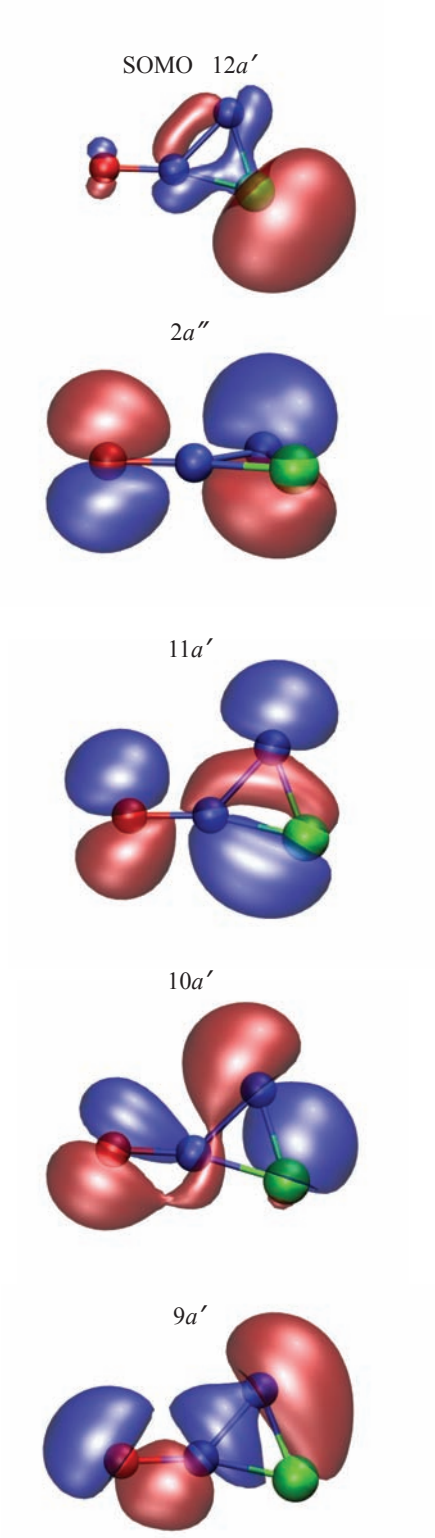


Figure S1: The five highest-lying occupied molecular orbitals of the $^2A'$ cyclic BNNO minimum at the cc-pVTZ ROHF level of theory.

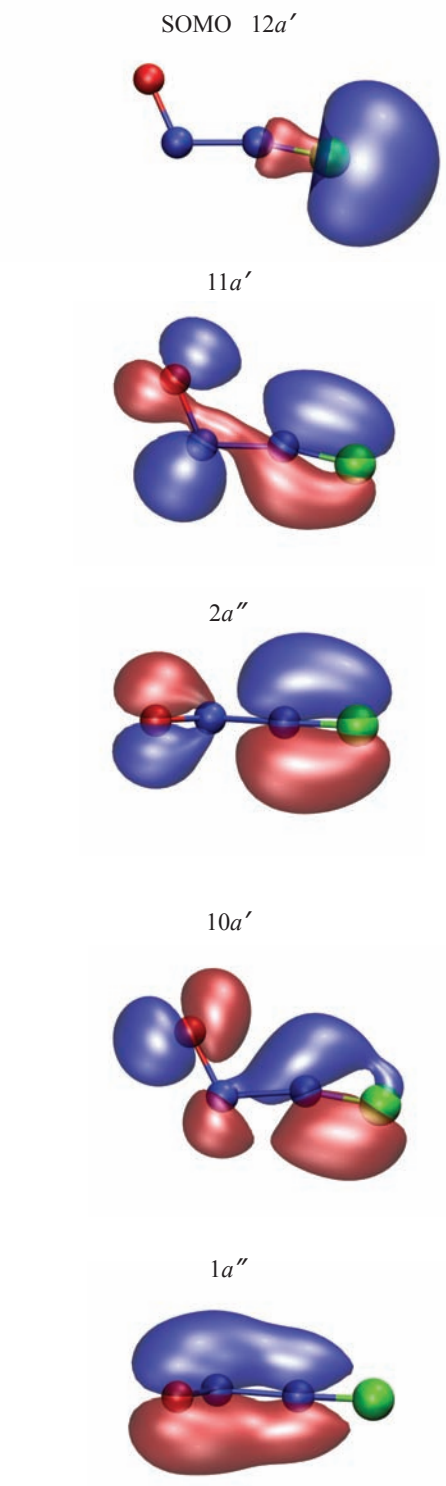


Figure S2: The five highest-lying occupied molecular orbitals of the $^2A'$ *trans* BNNO minimum at the cc-pVTZ ROHF level of theory.

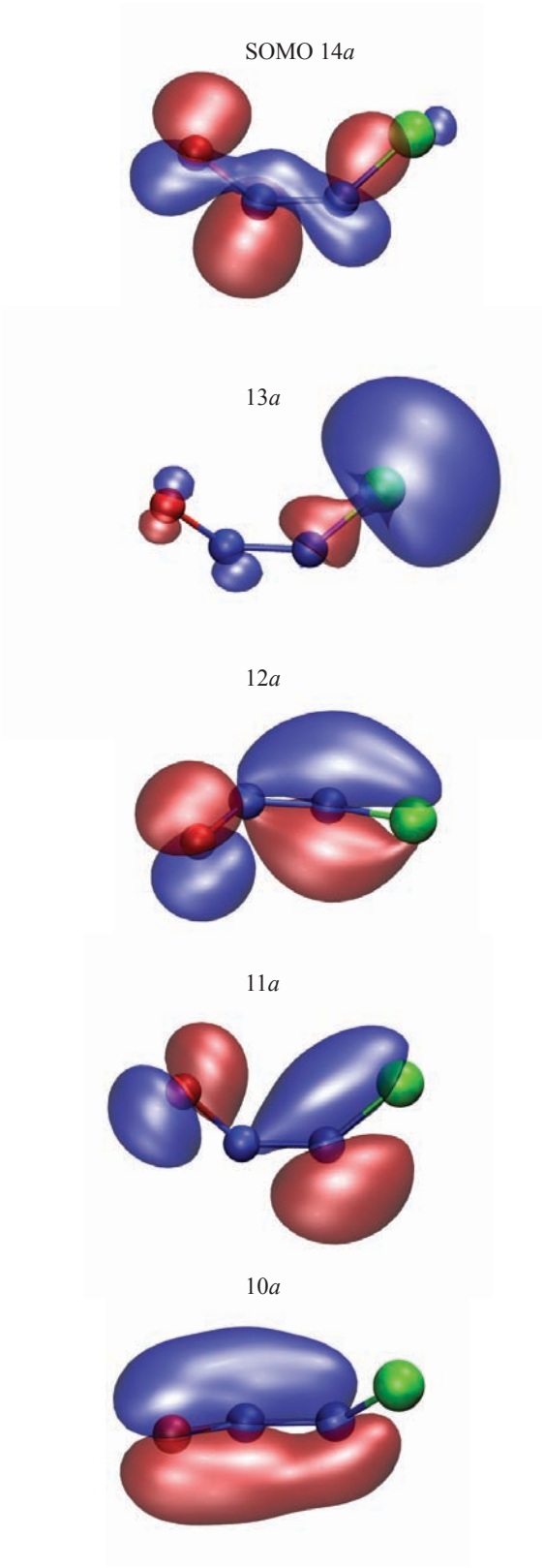


Figure S3: The five highest-lying occupied molecular orbitals of the $^2A$ *cis* BNNO minimum at the cc-pVTZ ROHF level of theory.

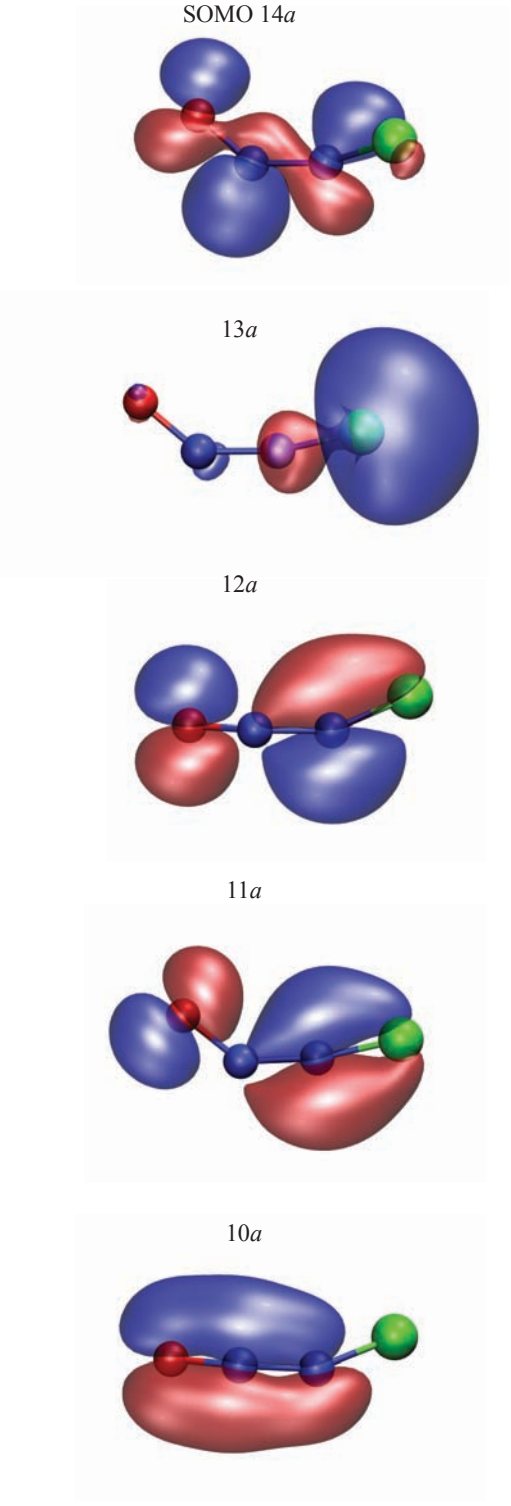


Figure S4: The five highest-lying occupied molecular orbitals of the transition state TS1 at the cc-pVTZ ROHF level of theory.

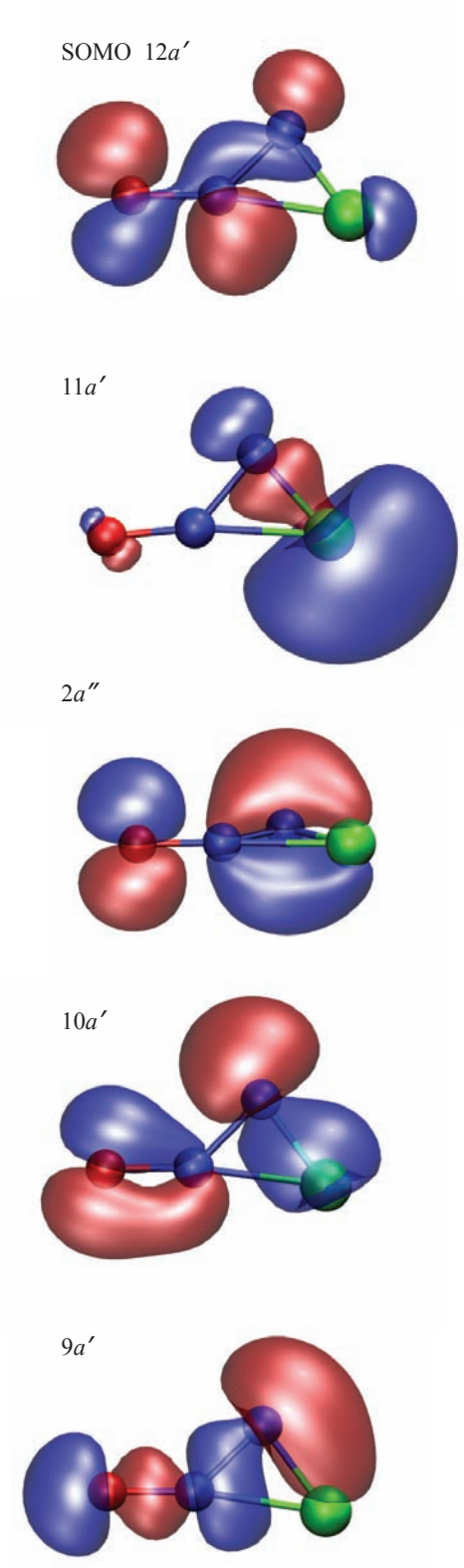


Figure S5: The five highest-lying occupied molecular orbitals of the transition state TS2 at the cc-pVTZ ROHF level of theory.

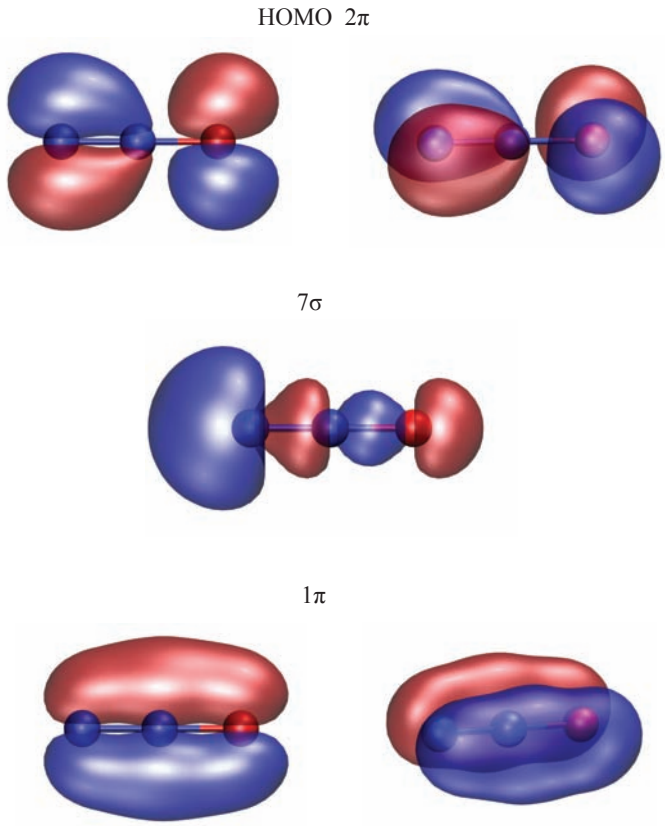


Figure S6: The five highest-lying occupied molecular orbitals of the $\tilde{X}\ ^1\Sigma^+$ $N_2O$ molecule at the cc-pVTZ RHF level of theory.

# Bibliography

[1] G. Wang and M. Zhou, Chem. Phys. Lett. **342**, 90 (2007).